Optimisation of Transfer and Doping of Polymer Supported CVD Graphene

Moon H. Kang

Department of Engineering

University of Cambridge

This dissertation is submitted for the degree of

Doctor of Philosophy

Darwin College

Jan. 2017

Declaration

I hereby declare that except where specific reference is made to the work of others, the contents of this dissertation are original and have not been submitted in whole or in part for consideration for any other degree or qualification in this, or any other University. This dissertation is the result of my own work and includes nothing which is the outcome of work done in collaboration, except where specifically indicated in the text. This dissertation contains less than 65,000 words including appendices, bibliography, footnotes, tables and equations and has less than 150 figures.

Moon H. Kang

Jan. 2017

Acknowledgements

Publications

The following publications have been produced during the course of this research.

- **Journals**

1. **Kang, M. H.**; Milne, W. I.; Cole, M. T., Doping Stability and Opto-Electronic Performance of Chemical Vapour Deposited Graphene on Transparent Flexible Substrates. *IET Circuits, Devices & Systems***, 2015,** *9* (1), 39-45.

2. **Kang, M. H.**; Milne, W. I.; Cole, M. T., Temporal Stability of Metal-Chloride-Doped Chemical-Vapour-Deposited Graphene. *ChemPhysChem***, 2016,** *17* (16), 2545-2550.

3. **Kang, M. H.**; Prieto López, L. O.; Chen, B.; Teo, K.; Williams, J. A.; Milne, W. I.; Cole, M. T., Mechanical Robustness of Graphene on Flexible Transparent Substrates. *ACS Applied Materials & Interfaces***, 2016,** *8* (34), 22506-22515.

4. **Kang, M. H.**; Qiu, G.; Cepek, C.; Wu, L.; Kim, J.; Milne, W. I.; Cole, M. T., Polymer-supported chemically-doped CVD graphene, in preparation for submission, **2017.**

- **Conferences**

5. **Kang, M. H.**; Milne, W. I.; Cole, M. T., Doping Stability and Opto-electronic Performance of Chemical Vapour Deposited Graphene for Plastic Electronic Applications, *AMFPD* **2015**, p.229 –p.232.

6. **Kang, M. H.**; Milne, W. I.; Cole, M. T., Emerging Graphene Technologies: Flexible Transparent Conductors, *IET talk - Graphene Based Technologies*, **2016**.

Abstract

Commercial interest in graphene is increasing, and at a pace. The concurrently high mechanical robustness and electrical conductance make the material suitable for use in a wide array of emerging flexible electronics devices. Theoretically, graphene is stronger than diamond, more conductive than copper, and more flexible than rubber - it has much potential for use in a myriad of flexible electronics applications. However, upon transfer, monolayer graphene has been reported to have poor mechanical robustness and low electrical conductivity relative to theoretical estimates. This has limited the commercial adoption.

This thesis presents the author's efforts towards the development of two new graphene transfer methods; Hot Press Laminate (HPL), and Ultra Violet Adhesive (UVA) transfer, both of which have been shown to enhance the degree of adhesion between the as-grown graphene and the polymer carrier substrate. To assess the feasibility of the transfer approach, sheet resistance (R_S) maps and optical transmittance (%T) maps of the transferred graphene using the two approaches have been measured, alongside a number of metrological studies to better understand the means though which the adhesion is improved and the effects such improved adhesion has on the transport within these two-dimensional thin films. The adhesion of transferred graphene on a substrate has been examined using conventional peel-off tests and the mechanical robustness of the transferred graphene was investigated by measuring resistance as a function of bend angle with repeated bend-relax cycles in a fully-automated, custom-built bend system.

Because of its transparency and high conductivity graphene is especially useful in applications requiring transparent contacts, such as in organic light emitting diodes (OLEDs). To further increase the electrical conductivity and tune the work function of the as-grown

graphene for such applications, chemical doping has been investigated using common metal chloride compounds; $AuCl_3$, $FeCl_3$, $SnCl_2$, $IrCl_3$ and $RhCl_3$. The spatial and temporal variation in R_S, %T, and contact angle have been measured for nominally pristine and doped graphene samples. Micron-scale spatial mapping of the conductivity has also been conducted revealing edge-mediated conduction in doped graphene. It was determined that the high electrical conductivity of the doped graphene was principally due to charge transfer from the dopant to the graphene, with such charge transfer resulting in a notable work function shift. This work function shift, a critical parameter for various systems such as field electron emitters and OLEDs, was independently quantified using Ultra-violet Photo-Spectroscopy (UPS), Kelvin Prove Force Microscopy (KPFM), Hall measurement, and Density Functional Theory (DFT) and was subsequently compared to the Gibb's free energy and standard reduction potential of the composite metal ions within the metal chlorides. Temperature-dependent transport studies (I-V) suggested that the Fermi level shift of doped graphene enhanced charge carrier transport by increasing the transmission coefficient associated with intrinsic potential barriers within the graphene, such as the carbon atoms and grain boundaries. Variable Range and Nearest Neighbour Hopping were found to dominate the transport in the undoped graphene, whilst transport in doped graphene is principally attributed to combined Nearest Neighbour Hopping and diffusive transport.

Contents

List of Figures

xiv

List of Tables

Symbols and Abbreviations

All symbols and abbreviations are written in the text with the denotation immediately following the first usage.

Symbols used in this thesis have the following meanings;

R_S   Sheet resistance

%T   Optical transmittance (%)

$\%T_{550\ nm}$ Optical transmittance (%) at 550 nm wavelength

E_F   Fermi level

m*   Effective mass

γ   Surface energy

W_{ad}   Work of adhesion

R_b   Bending radius

Me_xCl_y   Metal chloride

φ   Work function

R_C   Contact resistance

ϕ_b   Grain boundary height

Abbreviations used in this thesis have the following meanings;

HPL   Hot Press Lamination

UVA   Ultra Violet Adhesive

UPS   Ultra-violet Photo-Spectroscopy

KPFM   Kelvin Prove Force Microscopy

DFT   Density Functional Theory

VRH   Variable Range Hopping

NNH   Nearest Neighbour Hopping

FTO   Fluorine-Tin-Oxide

ITO   Indium-Tin-Oxide

OLED   Organic Light Emitting Diode

HOMO   Highest Occupied Molecular Orbital

LUMO   Lowest Occupied Molecular Orbital

CNT   Carbon nanotube

HOPG   Highly Oriented Pyrolytic Graphite

CVD   Chemical Vapour Deposition

AuCl$_3$	Gold Chloride
FeCl$_3$	Iron Chloride
SnCl$_2$	Tin Chloride
IrCl$_3$	Iridium Chloride
RhCl$_3$	Rhodium Chloride
DOS	Density Of States
FET	Field Effect Transistor
PET	polyethylene terephthalate
SEM	Scanning Electron Microscopy
SSRM	Scanning Spread Resistance Microscopy
PECVD	Plasma Enhanced Chemical Vapour Deposition
DMC	Decamethylcobaltocene
F2-HCNQ	3,6-difluoro-2,5,7,7,8,8-hexyacyano-quinodimethane
AFM	Atomic Force Microscopy
TRT	Thermal Release Tape
GraHIL	Gradient Hole Injection Layer
PEDOT:PSS	poly(3,4-ethylenedioxythiophene) polystyrene sulfonate
TEM	Transmission Electron Microscopy
GO	Graphene Oxide
PMMA	poly-methyl methacrylate

PDMS   polydimethylsiloxane

EDX   Energy-Dispersive Xray spectroscopy

(NH$_4$)$_2$S$_2$O$_8$ Ammonium Persulfate

EVA   Ethylene Vinyl Acetate

RMS   Root Mean Square

DMT   Derjaguin, Muller and Toporov technique

JKR   Johnson, Kendall and Roberts analysis model

AgNW   Silver Nanowire

CTLM   Circular Transmission Line Model

Chapter 1   Introduction

1.1   Motivation

For several decades, the electronics industry has utilised silicon and inorganic transparent conductors, such as fluorine-tin-oxide (FTO) and indium-tin-oxide (ITO), for large area transparent electronics in almost every display and television we see day-to-day. Such large area electronic devices are increasingly being confronted by the requirements for their use in flexible electronics. The flexibility of FTO and ITO have proven insufficient upon bending; both fracture and become irreversibly damaged at strains of only 1.2 – 1.4%.[1] Organic materials have been studied as one alternative.[2-5] However such organic devices have an undesirable characteristic hue and use either FTO or ITO as a primary electrode,[6-7] with the brittleness of these composite materials producing serious problems in the electrical performance of the fabricated devices, especially during flexing.[8-13]

Much effort has been invested in finding alternative materials which are mechanically stable, electrically conductive, and optically transparent. Carbon nanotubes[14-21] and silver nanowires[22-26] have attracted significant attention and have been widely integrated into many devices as ITO and FTO replacements. However, the surface roughness of such ensemble nanomaterials, when dispersed on substrates, is a major issue causing areal non-uniformity in the electrical performance[27-29] as well as temporal degradation by electrical short-circuits under repeated bending.[29] As an organic electrode, poly(3,4-ethylenedioxythiophene) polystyrene sulfonate (PEDOT:PSS)[3-5, 30] has been used widely due to its comparatively low cost and ease of integration. It is readily spin coated. However, PEDOT:PSS is water-soluble and inherently sensitive to moisture; it is thus atmospherically unstable.[2] Consequently, devices based on PEDOT:PSS must be encapsulated or

hermetically sealed to prevent moisture ingress, with such devices unable to be cleaned with deionised (DI) water - a necessary passivation stage during photolithography.
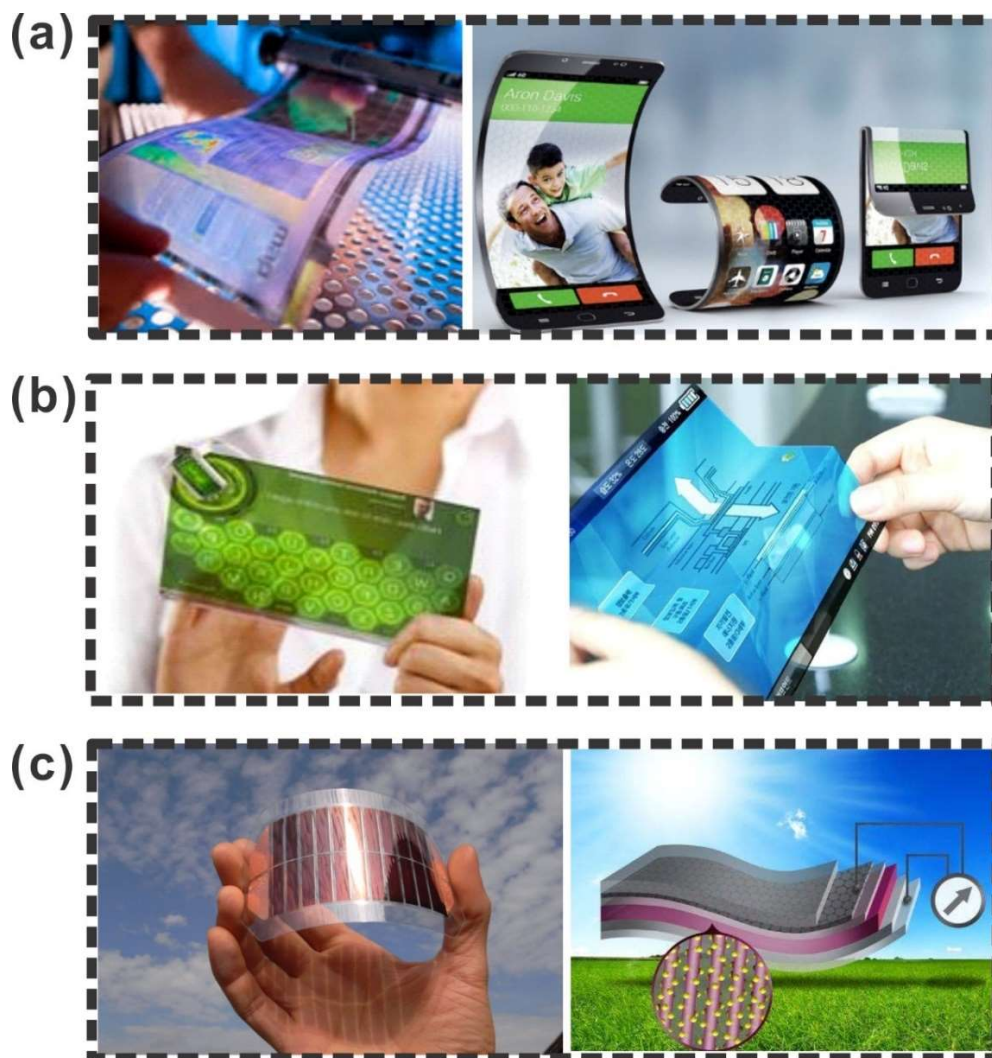
Figure 1.1. Conceptual images of graphene application to flexible electronics. (a) flexible displays, (b) bendable transparent touch screens, and (c) flexible solar cells. Images adapted from [31-36].

Graphene, a 2D material is widely believed to be one of the most promising materials for realising flexible electronics after it was first isolated in Manchester in 2004.[37] The Hall mobility of mechanically exfoliated graphene is predicted to be $10^5 – 10^6$ cm^2/Vs, for a charge carrier concentration ~10^{12} cm^{-2}.[38] There is mounting evidence to suggest that graphene is extremely well suited for use in transparent electronics.[39-47] Studies on the

properties of graphene have been, to date, largely carried out on small samples (< 10 mm x 10 mm) under typical near-ideal situations, such as the absence of surface impurities or lattice defects, which likely do not reflect real graphene obtained on a large scale in an industrial context, certainly in the near-term at least. Although there have been many graphene-based concepts reported[31-36] (Figure 1.1), there has been little in the way of successful manufacturing of flexible electronics using graphene, with a few reports of stable and long-lasting operation under repeated mechanical flexing. To enable the use of graphene and its unique properties in large-scale flexible electronics it is critical to overcome some commercialisation barriers including reproducibility and operational durability under repeated flexing.

Many approaches have been developed to synthesize graphene. Mechanical exfoliation is perhaps the most common. Here, graphene is made by peeling layers from highly oriented pyrolytic graphite (HOPG) using scotch tape.[37] Such exfoliated graphene cannot be easily scaled and the size of the graphene grains is limited to < 0.5 mm[37, 48] in diameter, typically, which makes it extremely challenging for such materials to be used in practical electronics given the challenges associated with multi-layer fabrication and device spatial registration. Graphene devices can also be manufactured with the use of graphene inks produced by electrochemical exfoliation of graphite in ionic liquids.[49-50]. However, such devices lack truly layered structures, with the resulting films formed from highly disordered graphene flakes that adopt no known, or predictable ordering or configuration. Such a lack of short-range order smears the nascent mechano-opto-electronic properties of the pristine graphene on which they are fabricated.[51-54] Many such disadvantages associated with the use of mechanical or electrochemical exfoliation can be remedied through the use of chemical vapour deposition (CVD). CVD allows for the synthesis of true monolayer, planar graphene on large area (> 50 cm x 50 cm) substrates with large grains (> 1 mm)[55-56] and high yields (>90%).[57-65]

At present to realise flexible electronics devices with CVD graphene, large-area compatible single layer transfer techniques must be developed alongside various methods to grow directly on technologically useful flexible substrates. Only limited progress has been made on graphene transfer, with polymer-supported transfer methods being the most commonly

employed.[66-70] Manual PMMA-based transfer requires skilled users, is costly, has low through-put, and is not compatible with large area electronics in mass-production. Moreover, polymer residues often cause problems in latter fabrication steps.[71-72] The adhesion of graphene on a substrate is another critical requirement for the realisation of flexible electronics, however graphene transferred via polymer-supporting approaches results in a material that is only bonded to the destination substrate via short range, weak van der Waals forces[73]. These provide insufficient adhesion to sustain repeated flexing. In this thesis, the author has developed two new CVD-graphene transfer approaches for large flexible electronics offering improved mechanical robustness with strong and long-lasting adhesion between the graphene and the destination substrate.

With the transfer method introduced in this thesis, the transferred graphene obtained mechanical stability, but to be used as a transparent conductor, the electrical resistance of graphene was found to be too high, in most cases, for commercial applications. Monolayer graphene has a sheet resistance of 2 - 5 kΩ/sq. with a transmittance of 97 – 98%. [74-78] which is too high for use in commercial applications, such as touch screens (R_S < 500 Ω/sq.) and OLEDs (R_S < 100 Ω/sq.).[79] Hybrid structures, consisting of metallic nanowires have been investigated elsewhere and shown to be capable of decreasing the electrical resistance of pristine graphene,[80-82] however the areal non-uniformity of nanowire networks is still high compared to pristine graphene. Substitutional doping is a well-established doping approach for polycrystalline and amorphous silicon[83-84] and has been researched elsewhere for graphene.[85-86] Nevertheless, doping causes unintentional dislocation in the graphene basal plane arrangement and subsequent line defect formation, which degrades the mechanical robustness of these doped graphene platforms.[86] To avoid these issues, chemical doping has been considered as one of the most viable means of decreasing R_S without compromising graphene's as-synthesised optical transparency.[87-93] This thesis addresses the chemical doping process through the use of metal chloride compounds. The electrical resistivity and optical transparency of graphene were inspected immediately following doping and the time-dependency of these properties was monitored to evaluate their temporal stability. The temperature dependence of the electron transport of the doped graphene was also investigated, with a focus on the shift in work function.

1.2   Thesis Outline

This thesis continues, in Chapter 2, with a review of the background literature detailing the fundamentals of graphene and its research history. Specifically, this includes; synthesis methods and an introduction to common graphene applications including; field effect transistors (FET), organic light emitting diodes (OLEDs), touch screens, and field emission displays.

After reviewing the background, the developed graphene transfer approaches are introduced in Chapter 3. The areal distribution of the electrical resistance and optical transparency of the transferred graphene will be presented therein. It will be shown that the mechanical robustness of the transferred graphene is enhanced with the author's proposed approaches. Such approaches are then compared to conventional means by comparing surface energy, peeling strength, and bending stability.

In Chapter 4, I report on the light emission properties of an OLED fabricated using the presented transfer approach using polyethylene terephthalate (PET) substrates with a discussion on the relationship between the measured performance and the required electrical properties. Chemical doping is then considered using; gold chloride: $AuCl_3$, iron chloride: $FeCl_3$, tin chloride: $SnCl_2$, iridium chloride: $IrCl_3$, and rhodium chloride: $RhCl_3$. The areal uniformity and temporal stability of doped graphene is detailed with R_S and %T maps, along with contact angle measurements. The spatial distribution of dopant molecules is also discussed in this chapter with results on Scanning Electron Microscopy (SEM) and Scanning Spread Resistance Microscopy (SSRM) presented.

In Chapter 5, the work function of the doped graphene and the Fermi level effects associated with the charge transfer from the dopant molecules are described. The amount of work function shift is evaluated and compared with the chemical parameters of the metal ions in the dopants, such as the Gibb's free energy and the reduction potential. The temperature dependence of the electron transport is then analysed with a discussion of previously

published transport models (Variable Range Hopping (VRH) and Nearest Neighbour Hopping (NNH)). The models are found to be largely representative for pristine graphene or reduced graphene oxide, but are not appropriate in explaining transport in doped graphene, and thus the author suggests a new transport model in such doped graphene cases.

This thesis concludes by considering the future of graphene and its associated applications, which are briefly presented by summarising the evidence outlined in earlier chapters.

References

1. Bradt, R. C.; Munz, D.; Sakai, M.; White, K. W., *Fracture Mechanics of Ceramics: Active Materials, Nanoscale Materials, Composites, Glass, and Fundamentals*. Springer US: 2010.

2. Elschner, A.; Kirchmeyer, S.; Lovenich, W.; Merker, U.; Reuter, K., *Pedot: Principles and Applications of an Intrinsically Conductive Polymer*. CRC Press: 2010.

3. Alemu, D.; Wei, H.-Y.; Ho, K.-C.; Chu, C.-W., Highly Conductive Pedot:Pss Electrode by Simple Film Treatment with Methanol for Ito-Free Polymer Solar Cells. *Energy & Environmental Science*, **2012,** *5* (11), 9662-9671.

4. Li, Z.; Liang, Y.; Zhong, Z.; Qian, J.; Liang, G.; Zhao, K.; Shi, H.; Zhong, S.; Yin, Y.; Tian, W., A Low-Work-Function, High-Conductivity Pedot:Pss Electrode for Organic Solar Cells with a Simple Structure. *Synthetic Metals*, **2015,** *210, Part B*, 363-366.

5. Fan, X.; Xu, B.; Liu, S.; Cui, C.; Wang, J.; Yan, F., Transfer-Printed Pedot:Pss Electrodes Using Mild Acids for High Conductivity and Improved Stability with Application to Flexible Organic Solar Cells. *ACS Applied Materials & Interfaces*, **2016,** *8* (22), 14029-14036.

6. Andersson, A.; Johansson, N.; Bröms, P.; Yu, N.; Lupo, D.; Salaneck, W. R., Fluorine Tin Oxide as an Alternative to Indium Tin Oxide in Polymer Leds. *Advanced Materials*, **1998,** *10* (11), 859-863.

7. Peumans, P.; Yakimov, A.; Forrest, S. R., Small Molecular Weight Organic Thin-Film Photodetectors and Solar Cells. *Journal of Applied Physics*, **2003,** *93* (7), 3693-3723.

8. Indium Price Soars as Demand for Display Continue to Grow. https://www.compoundsemiconductor.net/article/-Indium-price-soars-as-demand-for-displays-continues-to-grow.html.

9. Scott, J. C.; Kaufman, J. H.; Brock, P. J.; DiPietro, R.; Salem, J.; Goitia, J. A., Degradation and Failure of Meh-Ppv Light-Emitting Diodes. *Journal of Applied Physics*, **1996,** *79* (5), 2745-2751.

10. Boehme, M.; Charton, C., Properties of Ito on Pet Film in Dependence on the Coating Conditions and Thermal Processing. *Surface and Coatings Technology*, **2005,** *200* (1–4), 932-935.

11. Lim, C.-Y.; Park, J.-K.; Kim, Y.-H.; Han, J.-I., Mechanical and Electrical Stability Indium-Tin-Oxide Coated Polymer Substrates under Continuous Bending Stress Condition. *Journal of International Council on Electrical Engineering*, **2012,** *2* (3), 237-241.

12.   Sierros, K. A.; Morris, N. J.; Ramji, K.; Cairns, D. R., Stress–Corrosion Cracking of Indium Tin Oxide Coated Polyethylene Terephthalate for Flexible Optoelectronic Devices. *Thin Solid Films*, **2009,** *517* (8), 2590-2595.

13.   Ke, L.; Kumar, R. S.; Chua, S. J.; Burden, A. P., Degradation Study in Flexible Substrate Organic Light-Emitting Diodes. *Applied Physics A*, **2005,** *81* (5), 969-974.

14.   Salajkova, M.; Valentini, L.; Zhou, Q.; Berglund, L. A., Tough Nanopaper Structures Based on Cellulose Nanofibers and Carbon Nanotubes. *Composites Science and Technology*, **2013,** *87*, 103-110.

15.   Koga, H.; Saito, T.; Kitaoka, T.; Nogi, M.; Suganuma, K.; Isogai, A., Transparent, Conductive, and Printable Composites Consisting of Tempo-Oxidized Nanocellulose and Carbon Nanotube. *Biomacromolecules*, **2013,** *14* (4), 1160-1165.

16.   Aliahmad, N.; Agarwal, M.; Shrestha, S.; Varahramyan, K., Paper-Based Lithium-Ion Batteries Using Carbon Nanotube-Coated Wood Microfibers. *IEEE Transactions on Nanotechnology*, **2013,** *12* (3), 408-412.

17.   Mangilal, A.; Qi, X.; Bong Sup, S.; Nicholas, K.; Kody, V.; Yuri, L., Conductive Paper from Lignocellulose Wood Microfibers Coated with a Nanocomposite of Carbon Nanotubes and Conductive Polymers. *Nanotechnology*, **2009,** *20* (21), 215602.

18.   Barnes, T. M.; Wu, X.; Zhou, J.; Duda, A.; van de Lagemaat, J.; Coutts, T. J.; Weeks, C. L.; Britz, D. A.; Glatkowski, P., Single-Wall Carbon Nanotube Networks as a Transparent Back Contact in Cdte Solar Cells. *Applied Physics Letters*, **2007,** *90* (24), 243503.

19.   Rowell, M. W.; Topinka, M. A.; McGehee, M. D.; Prall, H.-J.; Dennler, G.; Sariciftci, N. S.; Hu, L.; Gruner, G., Organic Solar Cells with Carbon Nanotube Network Electrodes. *Applied Physics Letters*, **2006,** *88* (23), 233506.

20.   Chien, Y.-M.; Lefevre, F.; Shih, I.; Izquierdo, R., A Solution Processed Top Emission Oled with Transparent Carbon Nanotube Electrodes. *Nanotechnology*, **2010,** *21* (13), 134020.

21.   Zhang, D.; Ryu, K.; Liu, X.; Polikarpov, E.; Ly, J.; Tompson, M. E.; Zhou, C., Transparent, Conductive, and Flexible Carbon Nanotube Films and Their Application in Organic Light-Emitting Diodes. *Nano Letters*, **2006,** *6* (9), 1880-1886.

22.   Kang, M. G.; Guo, L. J., Nanoimprinted Semitransparent Metal Electrodes and Their Application in Organic Light-Emitting Diodes. *Advanced Materials*, **2007,** *19* (10), 1391-1396.

23.   Lee, J.-Y.; Connor, S. T.; Cui, Y.; Peumans, P., Solution-Processed Metal Nanowire Mesh Transparent Electrodes. *Nano Letters*, **2008,** *8* (2), 689-692.

24.   Pschenitzka, F.; Shen, Y., Transparent Conductive Network of Silver Nanowires as Oled Electrode. *SID Symposium Digest*, **2012,** *43* (1), 1488-1491.

25.   Hu, L.; Choi, J. W.; Yang, Y.; Jeong, S.; La Mantia, F.; Cui, L.-F.; Cui, Y., Highly Conductive Paper for Energy-Storage Devices. *Proceedings of the National Academy of Sciences*, **2009,** *106* (51), 21490-21494.

26.   Zeng, X. Y.; Zhang, Q. K.; Yu, R. M.; Lu, C. Z., A New Transparent Conductor: Silver Nanowire Film Buried at the Surface of a Transparent Polymer. *Advanced Materials*, **2010,** *22* (40), 4484-4488.

27.   Buckley, A., *Organic Light-Emitting Diodes (Oleds): Materials, Devices and Applications*. Elsevier Science: 2013.

28.   Kwon, S. J.; Shon, B. K.; Chung, H. J.; Lee, J. D.; Cho, E. S.; Uh, H. S.; Lee, C. G., Vacuum in-Line Sealed Cnt-Fed Fabricated by a Screen-Printing of Photo-Sensitive Cnt Paste. *SID Symposium Digest of Technical Papers*, **2004,** *35* (1), 442-445.

29.   Yun, H. J.; Kim, S. J.; Hwang, J. H.; Shim, Y. S.; Jung, S.-G.; Park, Y. W.; Ju, B.-K., Silver Nanowire-Izo-Conducting Polymer Hybrids for Flexible and Transparent Conductive Electrodes for Organic Light-Emitting Diodes. *Scientific Reports*, **2016,** *6*, 34150.

30.   Sun, K.; Li, P.; Xia, Y.; Chang, J.; Ouyang, J., Transparent Conductive Oxide-Free Perovskite Solar Cells with Pedot:Pss as Transparent Electrode. *ACS Applied Materials & Interfaces*, **2015,** *7* (28), 15314-15320.

31.   Nanomaterials in Displays. http://www.nanotechmag.com/issue-1-article-nanotech-in-displays/.

32.   Jeon, H., Graphene Makes the Dream of Transparent Flexible Displays More Real. http://www.koreaittimes.com/story/496/crumple-your-tv-put-it-your-pocket.

33.   Ahn, J.-H.; Hong, B. H., Graphene for Displays That Bend. *Nature Nanotechnology*, **2014,** *9* (10), 737-738.

34.   Olarte, C. G. G., Graphene, the Future Is Already Present. http://www.monografias.com/trabajos92/grafeno-tecnologia-del-futuro/grafeno-tecnologia-del-futuro.shtml.

35.   Chandler, D. L., A New Approach Using Graphene Sheets. http://phys.org/news/2012-12-flexible-solar-cells-approach-graphene.html.

36.   Graphene Solar Panels for the Future. http://www.aerogelgraphene.com/graphene-solar-panels-2.

37.   Novoselov, K. S.; Geim, A. K.; Morozov, S. V.; Jiang, D.; Zhang, Y.; Dubonos, S. V.; Grigorieva, I. V.; Firsov, A. A., Electric Field Effect in Atomically Thin Carbon Films. *Science*, **2004,** *306* (5696), 666-669.

38.   Zhang, Y.; Tan, Y.-W.; Stormer, H. L.; Kim, P., Experimental Observation of the Quantum Hall Effect and Berry's Phase in Graphene. *Nature*, **2005,** *438* (7065), 201-204.

39.   Han, T.-H.; Lee, Y.; Choi, M.-R.; Woo, S.-H.; Bae, S.-H., Extremely Efficient Flexible Organic Light-Emitting Diodes with Modified Graphene Anode. *Nature photonics*, **2012,** *6* (2), 105-110.

40.   Kim, S.-Y.; Kim, J.-J., Outcoupling Efficiency of Organic Light Emitting Diodes Employing Graphene as the Anode. *Organic Electronics*, **2012,** *13* (6), 1081-1085.

41.   Wu, J.; Agrawal, M.; Becerril, H. A.; Bao, Z.; Liu, Z., Organic Light-Emitting Diodes on Solution-Processed Graphene Transparent Electrodes. *ACS Nano*, **2010,** *4* (1), 43-48.

42.   Bae, S.; Kim, H.; Lee, Y.; Xu, X. F.; Park, J.-S.; Zheng, Y.; Balakrishnan, J.; Lei, T.; Ri Kim, H.; Song, Y. I.; Kim, Y.-J.; Kim, K. S.; Ozyilmaz, B.; Ahn, J.-H.; Hong, B. H.; Iijima, S., Roll-to-Roll Production of 30-Inch Graphene Films for Transparent Electrodes. *Nature Nanotechnology*, **2010,** *5* (8), 574-578.

43.   Lee, J.; Cole, M. T.; Lai, J. C. S.; Nathan, A., An Analysis of Electrode Patterns in Capacitive Touch Screen Panels. *Journal of Display Technology*, **2014,** *10* (5), 362-366.

44.   Jaeho, K.; Masatou, I.; Yoshinori, K.; Kazuo, T.; Masataka, H.; Sumio, I., Low-Temperature Synthesis of Large-Area Graphene-Based Transparent Conductive Films Using Surface Wave Plasma Chemical Vapor Deposition. *Applied Physics Letters*, **2011,** *98* (9), 091502.

45.   Lin, P.; Choy, W. C. H.; Zhang, D.; Xie, F.; Xin, J.; Leung, C. W., Semitransparent Organic Solar Cells with Hybrid Monolayer Graphene/Metal Grid as Top Electrodes. *Applied Physics Letters*, **2013,** *102* (11), 113303.

46.   Park, H.; Brown, P. R.; Bulovic, V.; Kong, J., Graphene as Transparent Conducting Electrodes in Organic Photovoltaics: Studies in Graphene Morphology, Hole Transporting Layers, and Counter Electrodes. *Nano Letters*, **2012,** *12* (1), 133-140.

47.   Un Jung, Y.; Na, S.-I.; Kim, H.-K.; Jun Kang, S., Organic Photovoltaic Devices with Low Resistance Multilayer Graphene Transparent Electrodes. *Journal of Vacuum Science & Technology A*, **2012,** *30* (5), 050604.

48.   Huang, Y.; Sutter, E.; Shi, N. N.; Zheng, J.; Yang, T.; Englund, D.; Gao, H.-J.; Sutter, P., Reliable Exfoliation of Large-Area High-Quality Flakes of Graphene and Other Two-Dimensional Materials. *ACS Nano*, **2015,** *9* (11), 10612-10620.

49.   Liu, N.; Luo, F.; Wu, H.; Liu, Y.; Zhang, C.; Chen, J., One-Step Ionic-Liquid-Assisted Electrochemical Synthesis of Ionic-Liquid-Functionalized Graphene Sheets Directly from Graphite. *Advanced Functional Materials*, **2008,** *18* (10), 1518-1525.

50.   Lu, J.; Yang, J.-x.; Wang, J.; Lim, A.; Wang, S.; Loh, K. P., One-Pot Synthesis of Fluorescent Carbon Nanoribbons, Nanoparticles, and Graphene by the Exfoliation of Graphite in Ionic Liquids. *ACS Nano*, **2009,** *3* (8), 2367-2375.

51.   Park, S.; Ruoff, R. S., Chemical Methods for the Production of Graphenes. *Nature Nanotechnology*, **2009,** *4* (4), 217-224.

52.   Wu, Y.; Hao, Y.; Jeong, H. Y.; Lee, Z.; Chen, S.; Jiang, W.; Wu, Q.; Piner, R. D.; Kang, J.; Ruoff, R. S., Crystal Structure Evolution of Individual Graphene Islands During Cvd Growth on Copper Foil. *Advanced Materials*, **2013,** *25* (46), 6744-6751.

53.   Torrisi, F.; Hasan, T.; Wu, W.; Sun, Z.; Lombardo, A.; Kulmala, T. S.; Hsieh, G.-W.; Jung, S. M.; Bonaccorso, F.; Paul, P. J.; Chu, D. P.; Ferrari, A. C., Inkjet-Printed Graphene Electronics. *ACS Nano*, **2012,** *6* (4), 2992-3006.

54.   Xu, K.; Cao, P.; Heath, J. R., Scanning Tunneling Microscopy Characterization of the Electrical Properties of Wrinkles in Exfoliated Graphene Monolayers. *Nano Letters*, **2009,** *9* (12), 4446-4451.

55.   Wu, X.; Zhong, G.; D'Arsié, L.; Sugime, H.; Esconjauregui, S.; Robertson, A. W.; Robertson, J., Growth of Continuous Monolayer Graphene with Millimeter-Sized Domains Using Industrially Safe Conditions. *Scientific Reports*, **2016,** *6*, 21152.

56.   Miseikis, V.; Convertino, D.; Mishra, N.; Gemmi, M.; Mashoff, T.; Heun, S.; Haghighian, N.; Bisio, F.; Canepa, M.; Piazza, V., Rapid Cvd Growth of Millimetre-Sized Single Crystal Graphene Using a Cold-Wall Reactor. *2D Materials*, **2015,** *2* (1), 014006.

57.   Zhou, H.; Yu, W. J.; Liu, L.; Cheng, R.; Chen, Y.; Huang, X.; Liu, Y.; Wang, Y.; Huang, Y.; Duan, X., Chemical Vapour Deposition Growth of Large Single Crystals of Monolayer and Bilayer Graphene. *Nature Communications*, **2013**, *4*, 2096.

58.   Yao, Y.; Wong, C.-P., Monolayer Graphene Growth Using Additional Etching Process in Atmospheric Pressure Chemical Vapor Deposition. *Carbon*, **2012**, *50* (14), 5203-5209.

59.   de la Rosa, C. J. L.; Sun, J.; Lindvall, N.; Cole, M. T.; Nam, Y.; Löffler, M.; Olsson, E.; Teo, K. B. K.; Yurgens, A., Frame Assisted H2o Electrolysis Induced H2 Bubbling Transfer of Large Area Graphene Grown by Chemical Vapor Deposition on Cu. *Applied Physics Letters*, **2013**, *102* (2), 022101.

60.   Celebi, K.; Cole, M. T.; Teo, K. B.; Park, H. G., Observations of Early Stage Graphene Growth on Copper. *Electrochemical and Solid-State Letters*, **2012**, *15* (1), K1-K4.

61.   Sun, J.; Lindvall, N.; Cole, M. T.; Teo, K. B. K.; Yurgens, A., Large-Area Uniform Graphene-Like Thin Films Grown by Chemical Vapor Deposition Directly on Silicon Nitride. *Applied Physics Letters*, **2011**, *98* (25), 252107.

62.   Celebi, K.; Cole, M. T.; Choi, J. W.; Wyczisk, F.; Legagneux, P.; Rupesinghe, N.; Robertson, J.; Teo, K. B.; Park, H. G., Evolutionary Kinetics of Graphene Formation on Copper. *Nano Letters*, **2013**, *13* (3), 967-974.

63.   Bae, S.; Kim, H.; Lee, Y.; Xu, X.; Park, J.-S.; Zheng, Y.; Balakrishnan, J.; Lei, T.; Ri Kim, H.; Song, Y. I.; Kim, Y.-J.; Kim, K. S.; Ozyilmaz, B.; Ahn, J.-H.; Hong, B. H.; Iijima, S., Roll-to-Roll Production of 30-Inch Graphene Films for Transparent Electrodes. *Nature Nano*, **2010**, *5* (8), 574-578.

64.   Huang, P. Y.; Ruiz-Vargas, C. S.; van der Zande, A. M.; Whitney, W. S.; Levendorf, M. P.; Kevek, J. W.; Garg, S.; Alden, J. S.; Hustedt, C. J.; Zhu, Y.; Park, J.; McEuen, P. L.; Muller, D. A., Grains and Grain Boundaries in Single-Layer Graphene Atomic Patchwork Quilts. *Nature*, **2011**, *469* (7330), 389-392.

65.   Chen, Z.; Huang, T.; Jin, B. C.; Hu, J.; Lu, H.; Nutt, S., High Yield Synthesis of Single-Layer Graphene Microsheets with Dimensional Control. *Carbon*, **2014**, *68*, 167-174.

66.   Kang, J.; Shin, D.; Bae, S.; Hong, B. H., Graphene Transfer: Key for Applications. *Nanoscale*, **2012**, *4* (18), 5527-5537.

67.   Li, X.; Cai, W.; An, J.; Kim, S.; Nah, J.; Yang, D.; Piner, R.; Velamakanni, A.; Jung, I.; Tutuc, E.; Banerjee, S. K.; Colombo, L.; Ruoff, R. S., Large-Area Synthesis of High-Quality and Uniform Graphene Films on Copper Foils. *Science*, **2009**, *324* (5932), 1312-1314.

68.   Kim, K. S.; Zhao, Y.; Jang, H.; Lee, S. Y.; Kim, J. M.; Kim, K. S.; Ahn, J. H.; Kim, P.; Choi, J. Y.; Hong, B. H., Large-Scale Pattern Growth of Graphene Films for Stretchable Transparent Electrodes. *Nature*, **2009**, *457* (7230), 706-710.

69.   Suk, J. W.; Kitt, A.; Magnuson, C. W.; Hao, Y.; Ahmed, S. A.; An, J.; Swan, A. K.; Goldberg, B. B.; Ruoff, R. S., Transfer of Cvd-Grown Monolayer Graphene onto Arbitrary Substrates. *ACS Nano*, **2011**, *5* (9), 6916-6924.

70.   Hallam, T.; Wirtz, C.; Duesberg, G. S., Polymer-Assisted Transfer Printing of Graphene Composite Films. *Physica Status Solidi (b)*, **2013**, *250* (12), 2668-2671.

71.   Her, M.; Beams, R.; Novotny, L., Graphene Transfer with Reduced Residue. *Physics Letters A*, **2013**, *377* (21–22), 1455-1458.

72.   Sharon, M.; Sharon, M.; Shinohara, H.; Tiwari, A., *Graphene: An Introduction to the Fundamentals and Industrial Applications*. Wiley: 2015.

73.   Martins, L. G. P.; Song, Y.; Zeng, T.; Dresselhaus, M. S.; Kong, J.; Araujo, P. T., Direct Transfer of Graphene onto Flexible Substrates. *Proceedings of the National Academy of Sciences*, **2013**, *110* (44), 17762-17767.

74.   Suk, J. W.; Kitt, A.; Magnuson, C. W.; Hao, Y.; Ahmed, S.; An, J.; Swan, A. K.; Goldberg, B. B.; Ruoff, R. S., Transfer of Cvd-Grown Monolayer Graphene onto Arbitrary Substrates. *ACS Nano*, **2011**, *5* (9), 6916-6924.

75.   Kang, M. H.; Prieto López, L. O.; Chen, B.; Teo, K.; Williams, J. A.; Milne, W. I.; Cole, M. T., Mechanical Robustness of Graphene on Flexible Transparent Substrates. *ACS Applied Materials & Interfaces*, **2016**, *8* (34), 22506-22515.

76.   Kang, M. H.; Milne, W. I.; Cole, M. T., Temporal Stability of Metal-Chloride-Doped Chemical-Vapour-Deposited Graphene. *ChemPhysChem*, **2016**, *17* (16), 2545-2550.

77.   Blake, P.; Brimicombe, P. D.; Nair, R. R.; Booth, T. J.; Jiang, D.; Schedin, F.; Ponomarenko, L. A.; Morozov, S. V.; Gleeson, H. F.; Hill, E. W.; Geim, A. K.; Novoselov, K. S., Graphene-Based Liquid Crystal Device. *Nano Letters*, **2008**, *8* (6), 1704-1708.

78.   Tan, Y. W.; Zhang, Y.; Bolotin, K.; Zhao, Y.; Adam, S.; Hwang, E. H.; Das Sarma, S.; Stormer, H. L.; Kim, P., Measurement of Scattering Rate and Minimum Conductivity in Graphene. *Physical Review Letters*, **2007**, *99* (24), 246803.

79.   Ray, S., *Applications of Graphene and Graphene-Oxide Based Nanomaterials*. Elsevier Science: 2015.

80.   Lee, M.-S.; Lee, K.; Kim, S.-Y.; Lee, H.; Park, J.; Choi, K.-H.; Kim, H.-K.; Kim, D.-G.; Lee, D.-Y.; Nam, S.; Park, J.-U., High-Performance, Transparent, and Stretchable Electrodes Using Graphene–Metal Nanowire Hybrid Structures. *Nano Letters*, **2013**, *13* (6), 2814-2821.

81.   Jia, Y.; Chen, C.; Jia, D.; Li, S.; Ji, S.; Ye, C., Silver Nanowire Transparent Conductive Films with High Uniformity Fabricated Via a Dynamic Heating Method. *ACS Applied Materials & Interfaces*, **2016**, *8* (15), 9865-9871.

82.   Lee, D.; Lee, H.; Ahn, Y.; Jeong, Y.; Lee, D.-Y.; Lee, Y., Highly Stable and Flexible Silver Nanowire-Graphene Hybrid Transparent Conducting Electrodes for Emerging Optoelectronic Devices. *Nanoscale*, **2013**, *5* (17), 7750-7755.

83.   Cowern, N.; Colombeau, B.; Roozeboom, F.; Hopstaken, M.; Snijders, H.; Meunier-Beillard, P.; Lerch, W. In *Diffusion Suppression in Silicon by Substitutional C Doping*, Solid-State Device Research Conference, 2002. Proceeding of the 32nd European, 24-26 September 2002; 2002; pp 203-206.

84.   Spear, W. E.; Le Comber, P. G., Substitutional Doping of Amorphous Silicon. *Solid State Communications*, **1975**, *17* (9), 1193-1196.

85.   Tsetseris, L.; Wang, B.; Pantelides, S. T., Substitutional Doping of Graphene: The Role of Carbon Divacancies. *Physical Review B*, **2014**, *89* (3), 035411.

86.   Meng, F.; Ouyang, B.; Song, J., First-Principles Study of Dislocation Slips in Impurity-Doped Graphene. *The Journal of Physical Chemistry C*, **2015**, *119* (6), 3418-3427.

87.   Dettlaff-Weglikowska, U.; Skakalova, V.; Graupner, R.; Jhang, S. H.; Kim, B. H.; Lee, H. J.; Ley, L.; Park, Y. W.; Berber, S.; Tomanek, D.; Roth, S., Effect of Socl2 Treatment on Electrical and Mechanical Properties of Single-Wall Carbon Nanotube Networks. *Journal of the American Chemical Society*, **2005**, *127* (14), 5125-5131.

88.   Gunes, F.; Shin, H. J.; Biswas, C.; Han, G. H.; Kim, E. S.; Chae, S. J.; Choi, J. Y.; Lee, Y. H., Layer-by-Layer Doping of Few-Layer Graphene Film. *ACS Nano*, **2010**, *4* (8), 4595-4600.

89.   Kasry, A.; Kuroda, M. A.; Martyna, G. J.; Tulevski, G. S.; Bol, A. A., Chemical Doping of Large-Area Stacked Graphene Films for Use as Transparent, Conducting Electrodes. *ACS Nano*, **2010**, *4* (7), 3839-3844.

90.   Shin, H. J.; Choi, W. M.; Choi, D.; Han, G. H.; Yoon, S. M.; Park, H. K.; Kim, S. W.; Jin, Y. W.; Lee, S. Y.; Kim, J. M.; Choi, J. Y.; Lee, Y. H., Control of Electronic Structure of Graphene by Various Dopants and Their Effects on a Nanogenerator. *Journal of the American Chemical Society*, **2010**, *132* (44), 15603-15609.

91.   Li, X.; Xie, D.; Park, H.; Zhu, M.; Zeng, T. H.; Wang, K.; Wei, J.; Wu, D.; Kong, J.; Zhu, H., Ion Doping of Graphene for High-Efficiency Heterojunction Solar Cells. *Nanoscale*, **2013**, *5* (5), 1945-1948.

92.   Geng, H.-Z.; Kim, K. K.; Song, C.; Xuyen, N. T.; Kim, S. M.; Park, K. A.; Lee, D. S.; An, K. H.; Lee, Y. S.; Chang, Y.; Lee, Y. J.; Choi, J. Y.; Benayad, A.; Lee, Y. H., Doping and De-Doping of Carbon Nanotube Transparent Conducting Films by Dispersant and Chemical Treatment. *Journal of Materials Chemistry*, **2008**, *18* (11), 1261-1266.

93.   Hee Shin, D.; Min Kim, J.; Wook Jang, C.; Hwan Kim, J.; Kim, S.; Choi, S.-H., Annealing Effects on the Characteristics of Aucl3-Doped Graphene. *Journal of Applied Physics*, **2013**, *113* (6), 064305.

Chapter 2   Fundamentals and Applications of Graphene

2.1   Introduction

The development of electronics has proceeded at an unprecedented pace in recent history; a new generation of transparent, flexible and electrically conductive materials is coming to the fore with the advent of graphene. To successfully integrate graphene heterogeneously and at commercially viable large scales, a clear understanding of the fundamental characteristics and means of synthesis and transfer are critical, as are a firm understanding of the underlying physical properties of this unique material.

2.2   Two-Dimensional Carbon Sheets

Carbon atoms have six electrons distributed in the atomic orbitals as $1s^2\ 2s^2\ 2p^2$. 1s core electrons are essentially inert and do not contribute to the chemical bond and electron transport. The four outer valence electrons are central to the action of chemical and electrical actions.[1] In graphene, the 2s, $2p_x$ and $2p_y$ orbitals are hybridized to form three new planar orbitals, termed sp^2, which are the source of sigma bonds in carbon solids.[2] The chemical bonding of the carbon atoms in graphene is maintained by these three orbitals, and the mechanical properties of graphene are therefore dependent on the bond strength of these chemical bonds.[2-4]

Graphene is an atomically thin planar sheet of sp^2 bonded carbon atoms arranged in a honeycomb lattice.[5-7] The honeycomb lattice consists of the combination of two Bravais lattices, as illustrated in **Figure 2.1** (a). An atom on the A sublattice (red sphere) has three nearest neighbours in the same sublattice, situated at the upper right, upper left and lower positions. The structure can be seen as a triangular lattice for a unit Bravais lattice rather than a hexagon.[8] The lattice vectors can be written as

$$a_1 = \frac{a}{2}(3, \sqrt{3}), \qquad a_2 = \frac{a}{2}(3, -\sqrt{3}) \tag{2.1}$$

where a = 1.42 Å is the lattice constant meaning the distance between nearest neighbour carbons. The three nearest neighbour vectors in real space area given by

$$\delta_1 = \frac{a}{2}(1, \sqrt{3}), \qquad \delta_2 = \frac{a}{2}(1, -\sqrt{3}), \qquad \delta_3 = -a(1,0) \tag{2.2}$$
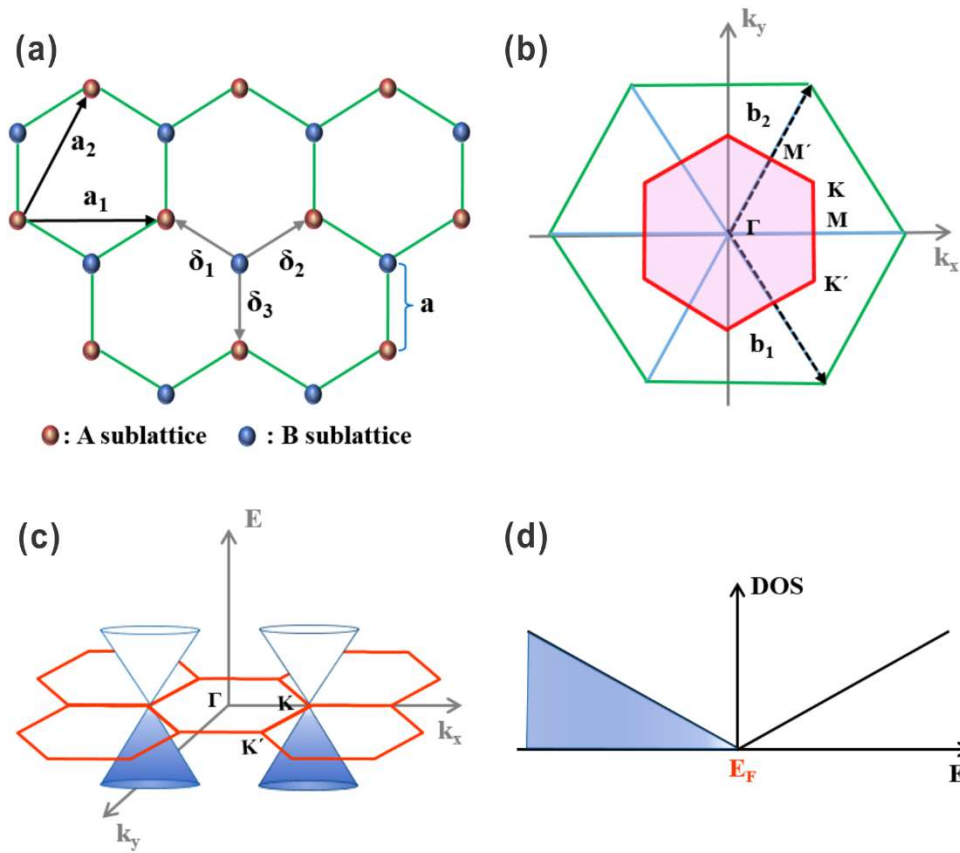
Figure 2.1 (a) Atomic structure of graphene in real space, (The vector a₁ and a₂ are basis vectors of the Bravais lattice), (b) the reciprocal lattice (red hexagon) of the graphene lattice in momentum (k) space (b₁ and b₂ are the primitive lattice vectors and the pink area is the First Brillouin Zone). (c) The linear energy-momentum (E-k) relation of graphene at K and K' point of monolayer pristine graphene.

The reciprocal lattice of graphene is illustrated in **Figure 2.1** (b). The reciprocal lattice vectors area is given by

$$b_1 = \frac{2\pi}{3a}(1, \sqrt{3}), \qquad b_2 = \frac{2\pi}{3a}(1, -\sqrt{3}) \tag{2.3}$$

Of particular importance for the physical properties of graphene are the two points K and K' at the corners of the graphene Brillouin zone. Their positions in momentum space are given by

$$K = \left(\frac{2\pi}{3a}, \frac{2\pi}{3\sqrt{3}a}\right), \qquad K' = \left(\frac{2\pi}{3a}, -\frac{2\pi}{3\sqrt{3}a}\right) \qquad (2.4)$$

Figure 2.1 (c) shows the energy bands of graphene as a function of momentum.   Graphene has a carbon atom located at each hexagonal vertex. When the atoms are placed onto the hexagonal lattice, there is no overlap between the p_z orbitals by symmetry and the p_z electrons forming the π bands therefore are treated independently.[9] Within the π-band approximation, using the conventional tight-binding model, the E-K relation of graphene can be described linearly as

$$E = \hbar v_F \sqrt{k_x^2 + k_y^2} \qquad (2.5)$$

where the k_x and k_y are the x and y components of the wave vector, k measured from the Dirac points (zero energy).[8] The valence and the conduction bands touch one another at a number of finite momentum values.[2] The momentum values at which the two bands touch are termed Dirac points (K and K' in the first Brillouin zone). As a result, graphene's spectrum does not present an energy gap. On the other hand, since the bands only touch at two momentum points, the density of states (DOS) is zero at the corresponding energy, as described in **Figure 2.1** (d). Therefore, graphene is termed a zero-gap semiconductor with a vanishingly small density of states at the Fermi energy (E_F).[2, 10-14]

We have a paradox. Here the use of the term semiconductor is a contradiction. As graphene has a zero bandgap it is not, in many regards a semiconductor. A semiconductor is defined as a material which has a small, yet non-zero, bandgap between the electron-filled valence band and the unoccupied conduction band; the bandgap is defined as the energy gap crossed by excited electrons from the valence band to the conduction band at room temperature.[15] The valence band of pristine graphene is completely filled and the conduction band is empty. This is consistent with standard semiconducting materials, however there is a significant difference in graphene's electronic structure. The E_F of graphene is located on a Dirac point rather than in the bandgap. Thus, charge carriers can be tuned continuously between electrons and holes therein allowing for a wide variety of fascinating potential.[16-20] Graphene is also considered as a transparent conductor due to its zero bandgap, high Fermi velocity (10^6 m/s)[21] and high electron mobility (200,000 $cm^2V^{-1}s^{-1}$ at electron densities of ~2 x 10^{11} cm-

^{2}).[22] More details on the use of graphene in large area electronics such as in light emitting diode (OLEDs) will be included in the next section.

2.3   Graphene as a Transparent Electrode in OLED

In the last five years alone, the number of graphene papers related to OLEDs has increased by 250%, and the number of filed patents by 357%.[23] Graphene is perceived as the perfect material for use in flexible and transparent OLED based displays.[24-29] Indium Tin Oxide (ITO) has been commonly used as an anode in OLED displays given its high optical transparency and suitably high conductivity. Nevertheless, ITO lacks flexibility. ITO is especially brittle when subjected to repetitive strain stress, with micro-crack formation occurring at only 1.2% strain.[30-33] Additionally, the cost of ITO has increased by 235% from 170 USD/kg in 2003 to 570 USD/kg in 2013[34-35]. Though there has been a dramatic rise in the use of ITO, there has been a general decline in the mining of the necessary indium. This has led to notable price inflation. Furthermore, indium mines are not uniformly distributed globally. Rather, they are concentrated in the People's Republic of China which is estimated to control between 60 and 70% of the global market.[36] Collectively these issues have led many to question the wider, long term use of indium based transparent electronic materials.

Carbon nanotubes (CNTs) have attracted interest for many years. Carbon is one of the most abundant elements on earth, whilst the worldwide supply of indium is limited [37]. Carbon CNTS are well placed to provide a transparent conductor due to their high flexibility and low resistance (~350 Ω/sq. with ~80% optical transparency at 550 nm).[37-40] Many research groups reported successful fabrication of OLED using conductive CNT electrodes.[40-45] However, current flow is guided by the CNT network resulting in luminous non-uniformity and stronger electric field at the top or bottom edges of CNT which can cause breakdown at high voltages.[46-47]

As an alternative, silver nanowires (AgNWs)[44, 48-55] can be easily spin- or spray-coated onto a target substrate. AgNW networks can be flexed without cracking and have proven significantly more functional than ITO in bendable applications. However, AgNW electrodes have voids between the wires which can be in the range of $\sim \mu m^2$ when coated with ~ 10 mg/ml concentration with a sheet resistance of 20 -30 Ω/sq..[56] Charge carriers located in the wires easily travel through the OLEDs organic layers, but in the void areas few to no carriers are injected causing notable non-uniformities in the resulting luminance.

Poly(3,4-ethylenedioxythiophene):poly(styrenesulfonate) (PEDOT:PSS) is one of the most studied conducting polymers to date. It can be uniformly deposited over large areas with a complete absence of voids.[57-59] Despite this, the electrical resistance of PEDOT:PSS (1500 Ω/sq., Aldrich. Co. Ltd.)[60] is still higher than ITO and has failed to compete with ITO in almost all applications this past decade. Although many attempts have been made to decrease the resistance by adding various solvents (isopropyl alcohol, glycerol or ethylene glycol),[57, 61] the improvement is limited due to the chemical degradation of the PEDOT:PSS, such as chain scission and disruption of the attractive interaction between the PEDOT and the PSS.[62] The resistance of PEDOT:PSS increases further during stretching or bending. This behaviour is primarily attributed to the directional alignment of the polymer chains along the direction of mechanical stress and the subsequent structural change from entangled chains to linear chains.[63]

Graphene may be the most viable candidate for applications as a transparent conductor with one of the highest optical transparencies yet reported (theoretically 2.3 % per graphene layer).[12, 64] Electrical resistance of multilayer CVD graphene as low as 450 Ω/sq. with 83% optical transparency have been reported.[65-67] Graphene is a 2D, uniform carbon film with no directional anisotropy (unlike the nanowires) allowing for uniform charge carrier injection. Moreover, the high flexibility of graphene with high Young's modulus (~ 1TPa)[9, 68-69] will allow for the possibility of flexible OLED displays. The highlights of the current state-of-the-art in graphene-based OLED research will be examined in the following paragraphs.
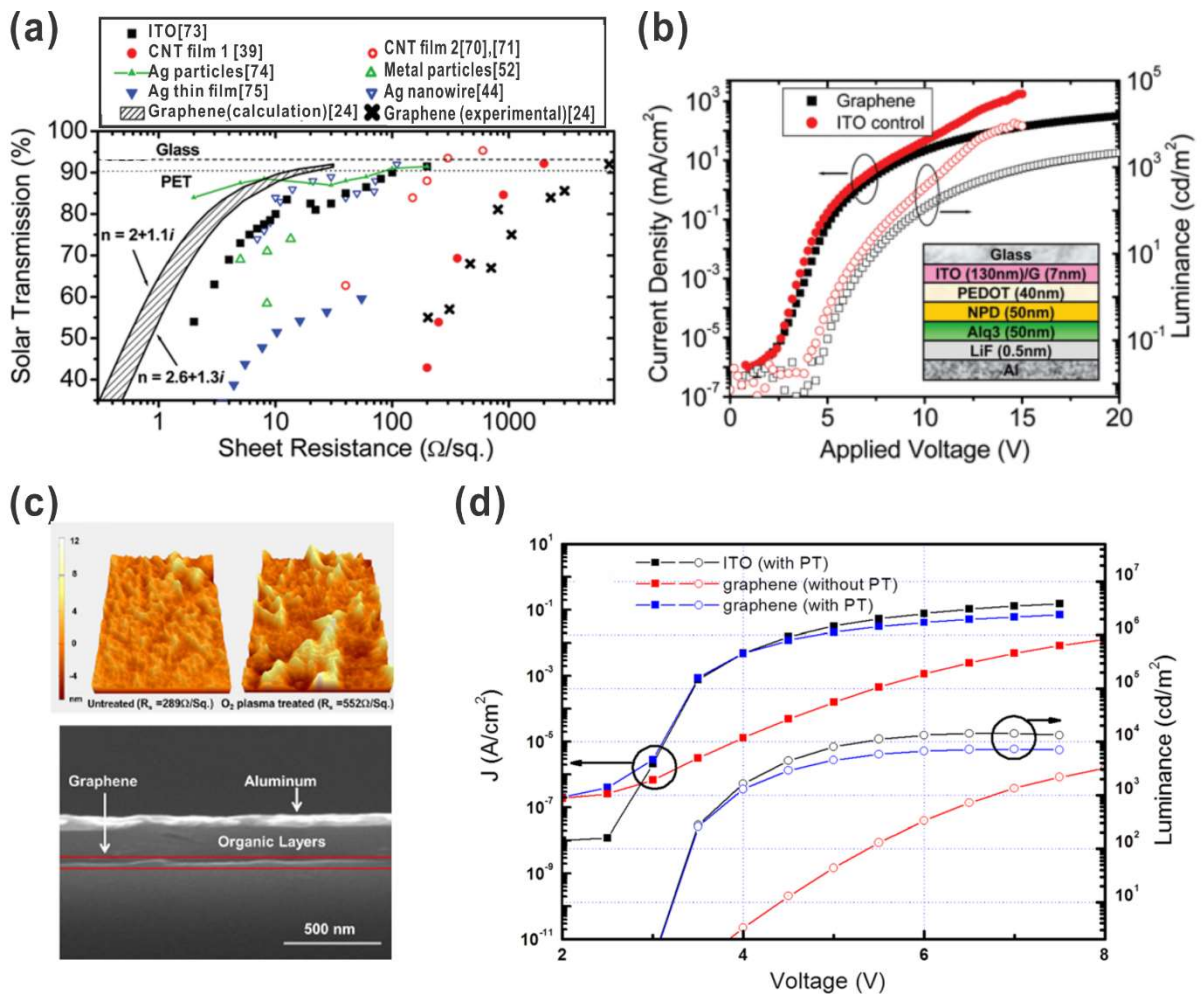
Figure 2.2 (a) The comparison of optical transmission versus sheet resistance of graphene with seven different kinds of transparent conductors, [24, 39, 44, 52, 70-75] (b) current density and luminance versus forward bias for an OLED on graphene and ITO anodes,[24] (c) the AFM images of O₂ plasma treated graphene and pristine graphene and the cross-sectional SEM image of OLED device fabricated on graphene, and (d) current density and luminance of OLED on ITO anodes and plasma-treated(PT) graphene anode.[26] Adapted from [24, 26].

As an early trial, Wu *et. al.* reported their study on the performance of OLEDs fabricated on solution-processed graphene transparent electrodes.[24] The solution of graphene flakes was spin-cast onto quartz substrates followed by a vacuum anneal step to evaporate residual solvents. **Figure 2.2** (a) summarises the optical transmission (%) at 550 nm, as a function of

sheet resistance (R_S) for different candidate transparent conductors. The %T and R_S of the graphene was calculated using the transfer matrix method[24] using the mean refractive indices reported in literature.[76-78] In that study, the thickness of the multilayer graphene films was ~ 7nm corresponding to an R_S of ~ 800 Ω/sq. and %T (550 nm) of 82 %. Considering the theoretical thickness of monolayer graphene (~0.345 nm), 7 nm thickness indicates at least 20 carbon layers ; too thick to be called graphene since eleven or more layers of stacked carbon films have a band structure similar to that of graphite rather than graphene.[12, 79] Even with the much thicker layer, the R_S of their graphene was 100 times higher than theoretical estimates would suggest. This might be attributed to the fact that the spin-casted graphene solution is especially rich in grain boundaries and traps compared to those films considered in theoretical calculations, therein limiting charge carrier transport.[7]

Figure 2.2 (b) shows the OLED layer structure (inset) and the current density and luminance of the graphene-OLED as a function of the voltage between the aluminium cathode and graphene (or ITO control) anode. Graphene-based OLEDs have been reported to exhibit comparable light-emission intensity and current density to conventional ITO-OLEDS at lower than 7 V, but the high R_S of graphene led to a voltage drop in the anode resulting in degraded current and hence luminance at biases > 7 V. Though solution-processed graphene provides simplicity of fabrication, spatial non-uniformities associated with deposition methods and the high R_S crucially diminish OLED performance. For this reason, CVD graphene is deemed to be a more sensible and industrially viable option for use in OLED displays given the large area uniform and truly monolayer growth. Issues however remain in the ability to transfer these materials to a range of flexible transparent substrates.

Hwang *et. al.* reported the use of a multilayer graphene anode for blue phosphorescent OLEDs using graphene synthesised by Ni catalysed thermal CVD.[26] The synthesised graphene was transferred from the Ni catalyst to a glass substrate and treated with O_2 plasma under mild conditions (1 min with 3 sccm O_2 , 300 W RF) to improve hole injection. As shown in **Figure 2.2** (d), the untreated graphene-OLED had a lower current density and luminance than the conventional ITO-OLED. However, the OLED with plasma-treated graphene showed nearly identical performance with the ITO-OLED. Here the authors' claimed that the improved OLED luminance and the lowered turn-on voltage were due to the enhancement of the hole injection from the plasma treated graphene.[26] Plasma treatments

have been widely used to improve the hole-injection from the graphene anode to the hole transport layer in OLEDs.[80-81] Enhanced hole injection is attributed to the modified work function following O_2-plasma exposure.[80] Since the work function of graphene (4.5 eV) is lower than the highly occupied molecular orbital (HOMO) level of the organic layer (~5.5 eV), a work function shift of graphene near to that of the organic layer demonstrably enhances hole injection.[26, 80]

However, O_2 plasma treatment has also been shown to increase the sheet resistance and surface roughness of the as-deposited graphene, as shown in the AFM roughness profile in **Figure 2.2** (c). This is a serious drawback for OLED luminance. If graphene-OLEDs are to become a commercial reality, there is a pressing need to establish a standardised approach for the production of efficient graphene-based OLED instead of using plasma treatment in order to uniformly decrease the R_S of graphene and enhance the carrier injection from graphene.

Han *et. al.* suggested the use of multilayer graphene and subsequent modification of its work function to improve OLED luminous efficiency.[25] In this study, graphene was synthesised on Cu foil using CVD with the subsequent multilayer graphene being transferred onto quartz substrates using the repeated application of the thermal release tape (TRT).[25, 82-83] To achieve a high current efficiency in OLEDs with graphene anodes, the hole injection efficiency from the graphene anode to the overlaying organic layers must be improved. To explore this, in this study the authors' embedded a self-organised gradient hole injection layer (GraHIL) between the graphene and hole transporting organic layer, as illustrated in **Figure 2.3** (a). The theoretical work function of graphene is around 4.5 eV. This is relatively low and thus does not match with the standard hole transporting organic layers, such as NPB (N,N´-Di(1-naphthyl)-N,N´-diphenyl-(1,1´-biphenyl)-4,4´-diamine) or CBP (4,4´-Bis(N-carbazolyl)-1,1´-biphenyl).
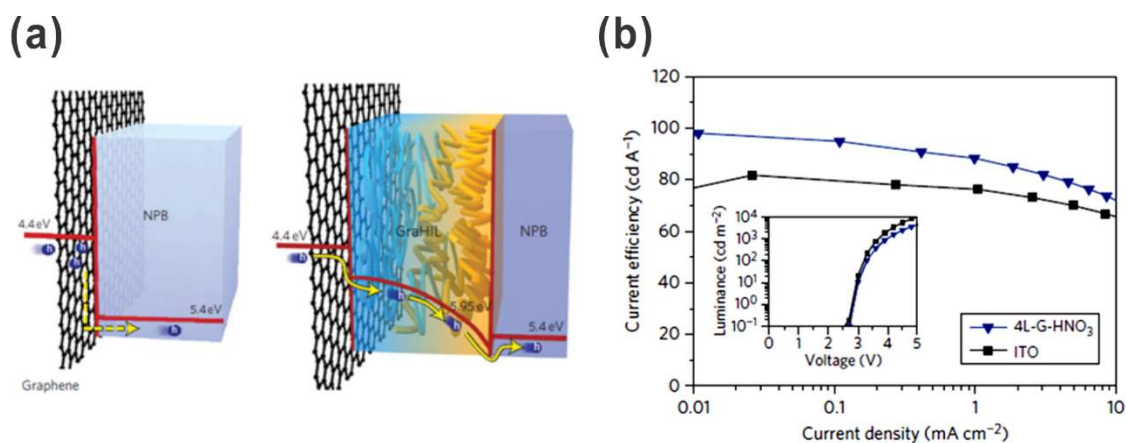
Figure 2.3 (a) A schematic illustration of hole injection from a graphene anode to a conventional hole transport layer (NPB) (left) and to GraHIL/NPB layer (right), (b) Current efficiency comparison between OLED devices using fourlayer graphene and ITO anodes. Inset: luminance as a function of voltage. Adapted from [25].

The concept of a work function gradient layer is illustrated in **Figure 2.3** (a). The polymeric GraHIL was composed of poly(3,4-ethylenedioxythiophene) polystyrene sulfonate (PEDOT:PSS) and tetrafluoroethyleneperfluoro- 3,6-dioxa-4-methyl-7-octenesulphonic in a 1:1 ratio, which was spin-coated to give a 50 nm-thick film on top of the graphene anode. This was then baked, immediately upon application, on a hot plate in air at 150℃ for 30 min. The R_S of the four-layered graphene was around 30 Ω/sq. after doping with HNO_3. The work function of the GraHIL was 5.95 eV, which is close to 5.4 eV; the work function of the hole transporting organic layer (NPB). As shown in **Figure 2.3** (b), the current efficiency of the OLED on graphene was higher (~98.1 cd/A) than the OLED on ITO (~81.8 cd/A). The efficiency they achieved using graphene is slightly higher than that of phosphorescent OLEDs using standard organic materials (CBP / Ir(ppy)$_2$(acac) / TPBi) and ITO (93.8 cd/A).[84] They claimed that the high efficiency of the graphene based OLED can be attributed to the increased hole injection caused by the modified structure using GraHIL.[25]

The R_S of the graphene anode is an essential factor to improve the OLED current-to-luminous efficiency. To decrease the R_S, a hybrid structure, consisting of graphene and metal nanowires has also been researched.[85-92] This combined architecture provides

complementary assistance to both graphene and the nanowires. Graphene patches separated during synthesis or transfer can be electrically linked by the highly conductive nanowires, whilst the graphene covers the sporadic voids in the nanowire network. As a result, a low R_S (25 Ω/sq.[92], 86 Ω/sq.[88], 16 Ω/sq.[93] and 42 Ω/sq.[94]) has been obtained in such hybrid structures.
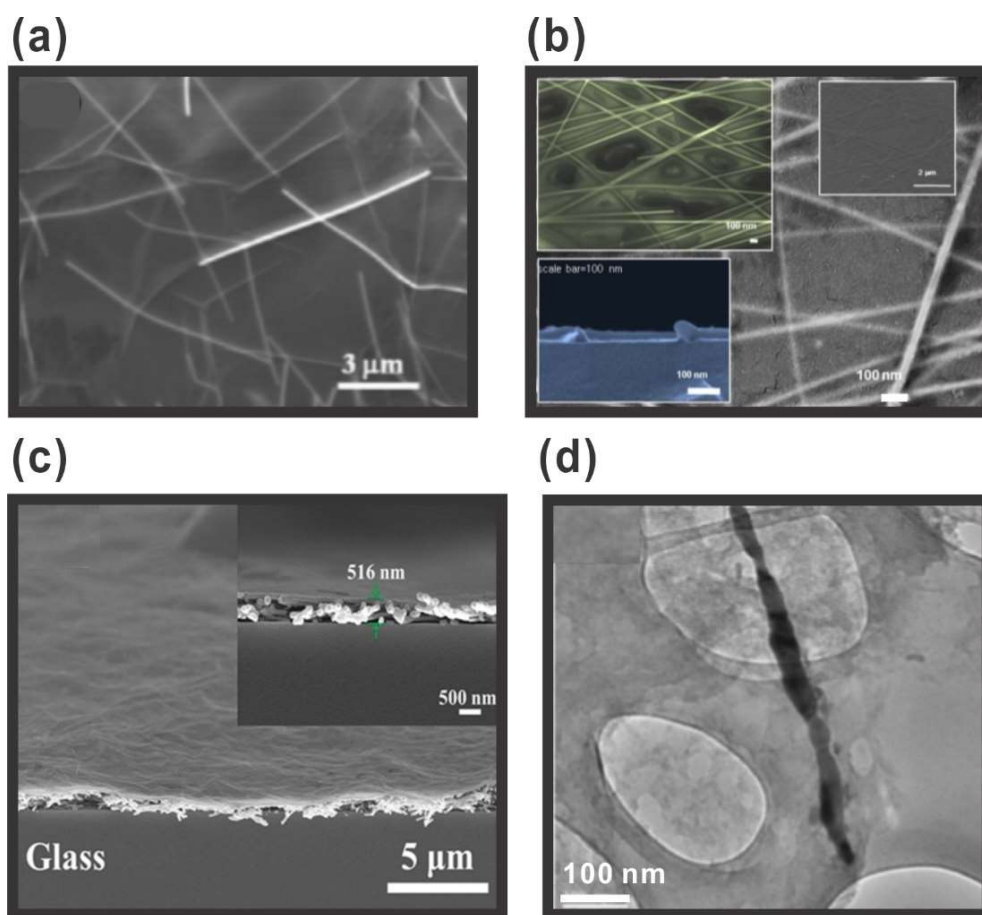
Figure 2.4 Scanning Electron Microscopy (SEM) ((a) – (c)) and Transmission Electron Microscopy (TEM) (d) images of graphene/silver nanowire hybrid structure. Adapted from [86-88, 92].

However, after forming a nanowire layer, such a hybrid film has a higher surface roughness compared to the pristine graphene alone(**Figure 2.4**).[86-88, 92] For instance, the thickness of silver nanowire is 40 -60 nm[95] which is about a hundred times thicker than graphene (~0.4

25

nm)[76-78]. The hybrid is not a genuine thin film, but rather a rough conductive mesh. The coarse surface of the hybrid electrode creates spatial non-uniformities in the sheet resistance which effects the uniformity of the light-emission.
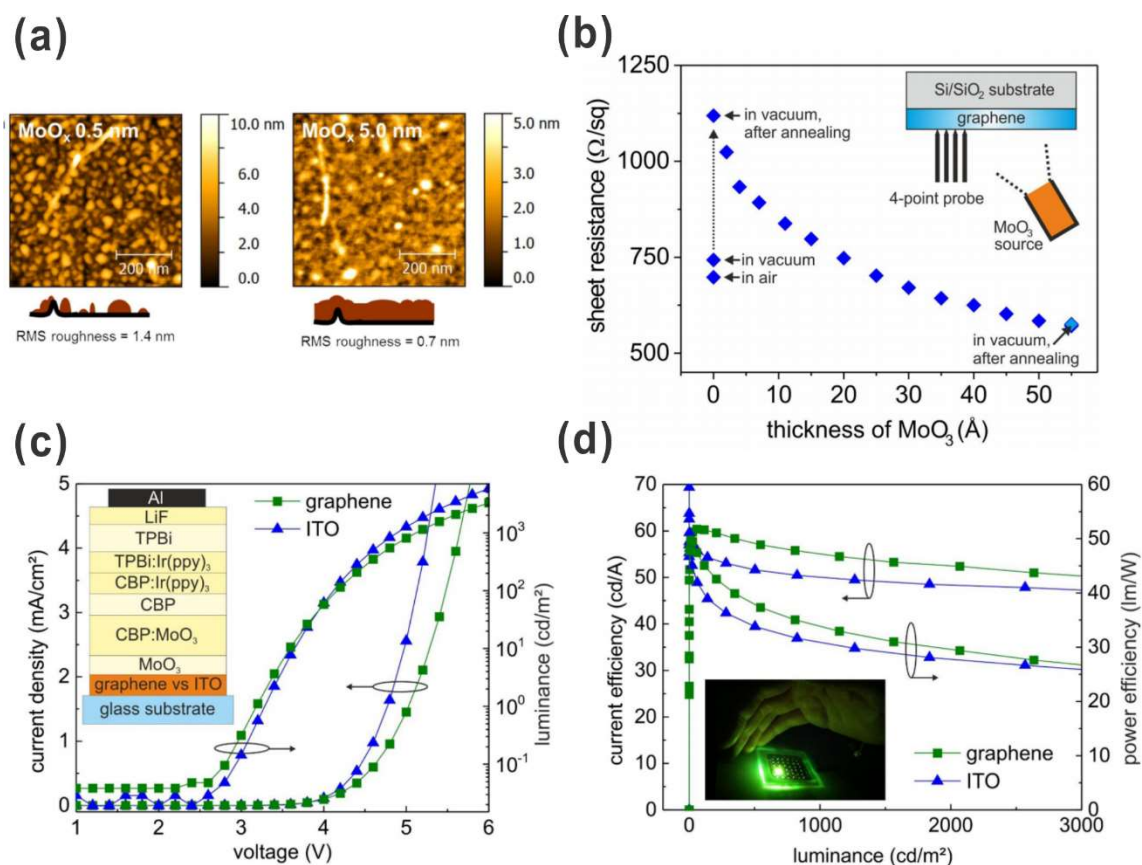
Figure 2.5 (a) AFM images of 0.5 nm and 5 nm thick MoO₃ deposited on monolayer graphene, (b) in-situ R$_S$ measurements of monolayer graphene in air and in vacuum, (c) current density and luminance characteristics of OLED with either MoO₃-doped monolayer graphene or ITO electrode, and (d) current and power efficiency versus luminance. Insets in (c) and (d) are the OLED layer stack comprising ITO or graphene and a photograph of light emission from this graphene -based OLED. Adapted from [96].

Charge transfer doping is one option to enhance the luminous efficiency of graphene-OLEDs. An OLED device fabricated with a thermally evaporated molybdenum trioxide (MoO₃) layer

on CVD graphene to induce the charge transfer doping has been reported.[96] The MoO_3 thin film produced a 1.9 eV interface dipole between the graphene and the organic layers, and the conduction band of the MoO_3 subsequently bent toward the graphene's E_F leading to well aligned transport carrier levels. **Figure 2.5** (a) shows AFM images of 0.5 nm and 5 nm thick MoO_3 deposited on CVD graphene transferred onto SiO_2. Increasing the MoO_3 thickness reduced the surface roughness and the R_S. With a 5 nm MoO_3 layer, the surface roughness was ~0.7 nm whilst the R_S was ~ 600 Ω/sq., as shown in **Figure 2.5** (a) and (b). The structure of the OLED device employing MoO_3-deposited graphene and measured OLED characteristics are shown in the inset in **Figure 2.5** (c). As shown, the luminance curve versus voltage with MoO_3/graphene appear nearly indistinguishable from that of the ITO-OLED, while it showed higher current efficiency and power efficiency than the ITO-OLED, as shown in **Figure 2.5** (d). The deposited MoO_3 induces a surface charge on the graphene. Thus, the graphene is strongly *p*-type doped offering abundant holes, thereby lowering R_S and increasing hole injection into the organic layers.[96]

Although graphene offers a remarkably high mobility, the concentration of the carriers is generally low (~10^{12} cm^{-2}).[97] This leads to an overall unimpressive electrode performance. Thus, stable doping has become a key challenge in engineering graphene into a highly conductive material with a high carrier concentration that is suitable for OLED applications. In addition to high conductivity a transparent graphene electrode should also efficiently inject charge carriers into the organic layers. Charge transfer doping by thin film deposition or chemical doping will open the door to many graphene-based flexible electronics applications, including OLEDs, and are as a result herein studied further in the following chapters.

2.4 Summary

This chapter presented a literature review on the fundamental physical and electronic structure of graphene and the developmental history of graphene applications, with a focus on OLEDs. Graphene has been considered as a new electrode material in OLEDs, but its gapless Dirac cone band structure and low carrier concentration needs modification for use in such

applications. Upon reviewing the developed approaches for several years, molecular doping is considered the most effective way for the modification and is further study in the subsequent chapters.

References

1.   Greenwood, N. N.; Earnshaw, A., *Chemistry of the Elements*. Elsevier Science: 2012.

2.   Peres, N. M. R., Graphene, New Physics in Two Dimensions. http://www.europhysicsnews.org/articles/epn/pdf/2009/03.

3.   Gan, Y. X., Effect of Interface Structure on Mechanical Properties of Advanced Composite Materials. *International Journal of Molecular Sciences*, **2009,** *10* (12), 5115-5134.

4.   Salvetat, J.-P.; Bonard, J.-M.; Thomson, N.; Kulik, A.; Forro, L.; Benoit, W.; Zuppiroli, L., Mechanical Properties of Carbon Nanotubes. *Applied Physics A*, **1999,** *69* (3), 255-260.

5.   Sur, U. K., Graphene: A Rising Star on the Horizon of Materials Science. *International Journal of Electrochemistry*, **2012,** *2012*, 12.

6.   Allen, M. J.; Tung, V. C.; Kaner, R. B., Honeycomb Carbon: A Review of Graphene. *Chemical reviews*, **2009,** *110* (1), 132-145.

7.   Mattevi, C.; Eda, G.; Agnoli, S.; Miller, S.; Mkhoyan, K. A.; Celik, O.; Mastrogiovanni, D.; Granozzi, G.; Garfunkel, E.; Chhowalla, M., Evolution of Electrical, Chemical, and Structural Properties of Transparent and Conducting Chemically Derived Graphene Thin Films. *Advanced Functional Materials*, **2009,** *19* (16), 2577-2583.

8.   Castro Neto, A. H.; Guinea, F.; Peres, N. M. R.; Novoselov, K. S.; Geim, A. K., The Electronic Properties of Graphene. *Reviews of Modern Physics*, **2009,** *81* (1), 109-162.

9.   Graphene. https://en.wikipedia.org/wiki/Graphene.

10.   Cornard, E., A Bandgap Semiconductor Nanostructure Made Entirely from Graphene. http://www.graphenea.com/blogs/graphene-news/6969324-a-bandgap-semiconductor-nanostructure-made-entirely-from-graphene.

11.   Obeng, Y.; Srinivasan, P., Graphene: Is It the Future for Semiconductors? An Overview of the Material, Devices, and Applications. *Interface-Electrochemical Society*, **2011,** *20* (1), 47.

12.   Geim, A. K.; Novoselov, K. S., The Rise of Graphene. *Nature materials*, **2007,** *6* (3), 183-191.

13.   Saito, R.; Fujita, M.; Dresselhaus, G.; Dresselhaus, u. M., Electronic Structure of Chiral Graphene Tubules. *Applied Physics Letters*, **1992,** *60* (18), 2204-2206.

14.   Novoselov, K.; Geim, A. K.; Morozov, S.; Jiang, D.; Katsnelson, M.; Grigorieva, I.; Dubonos, S.; Firsov, A., Two-Dimensional Gas of Massless Dirac Fermions in Graphene. *Nature*, **2005,** *438* (7065), 197-200.

15.   Kittel, C., *Introduction to Solid State Physics*. Wiley: 2004.

16.   Jia, T.-T.; Zheng, M.-M.; Fan, X.-Y.; Su, Y.; Li, S.-J.; Liu, H.-Y.; Chen, G.; Kawazoe, Y., Dirac Cone Move and Bandgap on/Off Switching of Graphene Superlattice. *Scientific Reports*, **2016,** *6*, 18869.

17.   Chiu, H.-Y.; Perebeinos, V.; Lin, Y.-M.; Avouris, P., Controllable P-N Junction Formation in Monolayer Graphene Using Electrostatic Substrate Engineering. *Nano Letters*, **2010,** *10* (11), 4634-4639.

18.   Lin, L.; Liao, L.; Yin, J.; Peng, H.; Liu, Z., Building Graphene P–N Junctions for Next-Generation Photodetection. *Nano Today*, **2015,** *10* (6), 701-716.

19.   Yu, X.; Shen, Y.; Liu, T.; Wu, T.; Jie Wang, Q., Photocurrent Generation in Lateral Graphene P-N Junction Created by Electron-Beam Irradiation. *Scientific Reports*, **2015,** *5*, 12014.

20.   Ryzhii, V.; Semenikhin, I.; Ryzhii, M.; Svintsov, D.; Vyurkov, V.; Satou, A.; Otsuji, T., Double Injection in Graphene P-I-N Structures. *Journal of Applied Physics*, **2013,** *113* (24), 244505.

21.   Hwang, C.; Siegel, D. A.; Mo, S.-K.; Regan, W.; Ismach, A.; Zhang, Y.; Zettl, A.; Lanzara, A., Fermi Velocity Engineering in Graphene by Substrate Modification. *Scientific Reports*, **2012,** *2*, 590.

22.   Bolotin, K. I.; Sikes, K.; Jiang, Z.; Klima, M.; Fudenberg, G.; Hone, J.; Kim, P.; Stormer, H., Ultrahigh Electron Mobility in Suspended Graphene. *Solid State Communications*, **2008,** *146* (9), 351-355.

23.   Google Scholar Search. https://scholar.google.co.uk/.

24.   Wu, J.; Agrawal, M.; Becerril, H. A.; Bao, Z.; Liu, Z., Organic Light-Emitting Diodes on Solution-Processed Graphene Transparent Electrodes. *ACS Nano*, **2010,** *4* (1), 43-48.

25.   Han, T.-H.; Lee, Y.; Choi, M.-R.; Woo, S.-H.; Bae, S.-H., Extremely Efficient Flexible Organic Light-Emitting Diodes with Modified Graphene Anode. *Nature photonics*, **2012,** *6* (2), 105-110.

26.   Hwang, J.; Kyw Choi, H.; Moon, J.; Yong Kim, T.; Shin, J.-W.; Woong Joo, C.; Han, J.-H.; Cho, D.-H.; Woo Huh, J.; Choi, S.-Y.; Lee, J.-I.; Yong Chu, H., Multilayered Graphene Anode for Blue Phosphorescent Organic Light Emitting Diodes. *Applied Physics Letters*, **2012,** *100* (13), 133304.

27.   Hwang, J.; Choi, H. K.; Moon, J.; Shin, J.-W.; Joo, C. W.; Han, J.-H.; Cho, D.-H.; Huh, J. W.; Choi, S.-Y.; Lee, J.-I.; Chu, H. Y., Blue Fluorescent Organic Light Emitting Diodes with Multilayered Graphene Anode. *Materials Research Bulletin*, **2012,** *47* (10), 2796-2799.

28.   Kim, S.-Y.; Kim, J.-J., Outcoupling Efficiency of Organic Light Emitting Diodes Employing Graphene as the Anode. *Organic electronics*, **2012,** *13* (6), 1081-1085.

29.   Park, H.; Brown, P. R.; Bulovic, V.; Kong, J., Graphene as Transparent Conducting Electrodes in Organic Photovoltaics: Studies in Graphene Morphology, Hole Transporting Layers, and Counter Electrodes. *Nano Lett,* **2012,** *12* (1), 133-40.

30.   Indium Price Soars as Demand for Display Continue to Grow. https://www.compoundsemiconductor.net/article/-Indium-price-soars-as-demand-for-displays-continues-to-grow.html.

31.   Scott, J. C.; Kaufman, J. H.; Brock, P. J.; DiPietro, R.; Salem, J.; Goitia, J. A., Degradation and Failure of Meh-Ppv Light-Emitting Diodes. *Journal of Applied Physics,* **1996,** *79* (5), 2745-2751.

32.   Boehme, M.; Charton, C., Properties of Ito on Pet Film in Dependence on the Coating Conditions and Thermal Processing. *Surface and Coatings Technology,* **2005,** *200* (1–4), 932-935.

33.   Lim, C.-Y.; Park, J.-K.; Kim, Y.-H.; Han, J.-I., Mechanical and Electrical Stability Indium-Tin-Oxide Coated Polymer Substrates under Continuous Bending Stress Condition. *Journal of International Council on Electrical Engineering,* **2012,** *2* (3), 237-241.

34.   George, M. W. *Indium*; 2003.

35.   Tolcin, A. C. *Indium*; 2014.

36.   Tveita, J. E., Value Growth and Vision. http://www.slideshare.net/kwoodwardsoam/sac-may-presentation-2012.

37.   Wikipedia, Abundance of Elements in Earth's Crust. https://en.wikipedia.org/wiki/Abundance_of_elements_in_Earth's_crust.

38.   Geng, H.-Z.; Kim, K. K.; So, K. P.; Lee, Y. S.; Chang, Y.; Lee, Y. H., Effect of Acid Treatment on Carbon Nanotube-Based Flexible Transparent Conducting Films. *Journal of the American Chemical Society,* **2007,** *129* (25), 7758-7759.

39.   Kymakis, E.; Stratakis, E.; Koudoumas, E., Integration of Carbon Nanotubes as Hole Transport Electrode in Polymer/Fullerene Bulk Heterojunction Solar Cells. *Thin Solid Films,* **2007,** *515* (24), 8598-8600.

40.   Zhang, D.; Ryu, K.; Liu, X.; Polikarpov, E.; Ly, J.; Tompson, M. E.; Zhou, C., Transparent, Conductive, and Flexible Carbon Nanotube Films and Their Application in Organic Light-Emitting Diodes. *Nano Letters,* **2006,** *6* (9), 1880-1886.

41.   Aguirre, C.; Auvray, S.; Pigeon, S.; Izquierdo, R.; Desjardins, P.; Martel, R., Carbon Nanotube Sheets as Electrodes in Organic Light-Emitting Diodes. *Applied Physics Letters,* **2006,** *88* (18), 183104-1.

42.   Chien, Y.-M.; Lefevre, F.; Shih, I.; Izquierdo, R., A Solution Processed Top Emission Oled with Transparent Carbon Nanotube Electrodes. *Nanotechnology,* **2010,** *21* (13), 134020.

43.   Peltola, J.; Weeks, C.; Levitsky, I.; Britz, D.; Glatkowski, P.; Trottier, M.; Huang, T., Carbon-Nanotube Transparent Electrodes for Flexible Displays. *Information Display,* **2007,** *23* (2), 20.

44.   Lee, J.-Y.; Connor, S. T.; Cui, Y.; Peumans, P., Solution-Processed Metal Nanowire Mesh Transparent Electrodes. *Nano Letters,* **2008,** *8* (2), 689-692.

45.   Wu, J.; Agrawal, M.; Becerril, H. A.; Bao, Z.; Liu, Z.; Chen, Y.; Peumans, P., Organic Light-Emitting Diodes on Solution-Processed Graphene Transparent Electrodes. *ACS Nano*, **2009,** *4* (1), 43-48.

46.   Rostedt, M.; Hall, M.; Shi, L.; Matthews, R., Spark Breakdown Voltage and Surface Degradation of Multiwalled Carbon Nanotube Electrode Surfaces. *World Academy of Science, Engineering and Technology, International Journal of Mechanical, Aerospace, Industrial, Mechatronic and Manufacturing Engineering,* *7* (2), 334-339.

47.   Hu, L.; Li, J.; Liu, J.; Grüner, G.; Marks, T., Flexible Organic Light-Emitting Diodes with Transparent Carbon Nanotube Electrodes: Problems and Solutions. *Nanotechnology,* **2010,** *21* (15), 155202.

48.   Maisch, P.; Tam, K. C.; Lucera, L.; Egelhaaf, H.-J.; Scheiber, H.; Maier, E.; Brabec, C. J., Inkjet Printed Silver Nanowire Percolation Networks as Electrodes for Highly Efficient Semitransparent Organic Solar Cells. *Organic Electronics,* **2016,** *38*, 139-143.

49.   Kim, A.; Lee, H.; Kwon, H.-C.; Jung, H. S.; Park, N.-G.; Jeong, S.; Moon, J., Fully Solution-Processed Transparent Electrodes Based on Silver Nanowire Composites for Perovskite Solar Cells. *Nanoscale,* **2016,** *8* (12), 6308-6316.

50.   Kim, Y.; Kim, J.-W., Silver Nanowire Networks Embedded in Urethane Acrylate for Flexible Capacitive Touch Sensor. *Applied Surface Science,* **2016,** *363*, 1-6.

51.   dos Reis Benatto, G. A.; Roth, B.; Corazza, M.; Søndergaard, R. R.; Gevorgyan, S. A.; Jørgensen, M.; Krebs, F. C., Roll-to-Roll Printed Silver Nanowires for Increased Stability of Flexible Ito-Free Organic Solar Cell Modules. *Nanoscale,* **2016,** *8* (1), 318-326.

52.   Kang, M. G.; Guo, L. J., Nanoimprinted Semitransparent Metal Electrodes and Their Application in Organic Light-Emitting Diodes. *Advanced Materials,* **2007,** *19* (10), 1391-1396.

53.   Pschenitzka, F.; Shen, Y., Transparent Conductive Network of Silver Nanowires as Oled Electrode. *SID Symposium Digest,* **2012,** *43* (1), 1488-1491.

54.   Hu, L.; Choi, J. W.; Yang, Y.; Jeong, S.; La Mantia, F.; Cui, L.-F.; Cui, Y., Highly Conductive Paper for Energy-Storage Devices. *Proceedings of the National Academy of Sciences,* **2009,** *106* (51), 21490-21494.

55.   Zeng, X. Y.; Zhang, Q. K.; Yu, R. M.; Lu, C. Z., A New Transparent Conductor: Silver Nanowire Film Buried at the Surface of a Transparent Polymer. *Advanced Materials,* **2010,** *22* (40), 4484-4488.

56.   Bormann, L.; Selzer, F.; Weiß, N.; Kneppe, D.; Leo, K.; Müller-Meskamp, L., Doped Hole Transport Layers Processed from Solution: Planarization and Bridging the Voids in Noncontinuous Silver Nanowire Electrodes. *Organic Electronics,* **2016,** *28*, 163-171.

57.   Zhang, X.; Wu, J.; Wang, J.; Zhang, J.; Yang, Q.; Fu, Y.; Xie, Z., Highly Conductive Pedot: Pss Transparent Electrode Prepared by a Post-Spin-Rinsing Method for Efficient Ito-Free Polymer Solar Cells. *Solar Energy Materials and Solar Cells,* **2016,** *144*, 143-149.

58.   Yoon, D. H.; Yoon, S. H.; Ryu, K.-S.; Park, Y. J., Pedot: Pss as Multi-Functional Composite Material for Enhanced Li-Air-Battery Air Electrodes. *Scientific Reports,* **2016,** *6*.

59.	Yagci, Ö.; Yesilkaya, S. S.; Yüksel, S. A.; Ongül, F.; Varal, N. M.; Kus, M.; Günes, S.; Icelli, O., Effect of Boric Acid Doped Pedot: Pss Layer on the Performance of P3ht: Pcbm Based Organic Solar Cells. *Synthetic Metals*, **2016,** *212*, 12-18.

60.	*Product Specification.* http://www.sigmaaldrich.com/Graphics/COfAInfo/SigmaSAPQM/SPEC/65/655201/655201-BULK_____ALDRICH__.pdf

61.	Lee, S., Conductivity Enhancement of Pedot: Pss Films through the Surface Treatment with Organic Solvent. *Journal of Nanoscience and Nanotechnology*, **2016,** *16* (3), 2880-2882.

62.	Oostra, A. J.; van den Bos, K. H. W.; Blom, P. W. M.; Michels, J. J., Disruption of the Electrical Conductivity of Highly Conductive Poly(3,4-Ethylenedioxythiophene):Poly(Styrene Sulfonate) by Hypochlorite. *The Journal of Physical Chemistry B*, **2013,** *117* (37), 10929-10935.

63.	Lee, Y.-Y.; Choi, G. M.; Lim, S.-M.; Cho, J.-Y.; Choi, I.-S.; Nam, K. T.; Joo, Y.-C., Growth Mechanism of Strain-Dependent Morphological Change in Pedot: Pss Films. *Scientific Reports*, **2016,** *6*.

64.	Nair, R. R.; Blake, P.; Grigorenko, A. N.; Novoselov, K. S.; Booth, T. J.; Stauber, T.; Peres, N. M.; Geim, A. K., Fine Structure Constant Defines Visual Transparency of Graphene. *Science*, **2008,** *320* (5881), 1308-1308.

65.	Kim, K. S.; Zhao, Y.; Jang, H.; Lee, S. Y.; Kim, J. M.; Kim, K. S.; Ahn, J.-H.; Kim, P.; Choi, J.-Y.; Hong, B. H., Large-Scale Pattern Growth of Graphene Films for Stretchable Transparent Electrodes. *Nature*, **2009,** *457* (7230), 706-710.

66.	Li, X.; Cai, W.; Colombo, L.; Ruoff, R. S., Evolution of Graphene Growth on Ni and Cu by Carbon Isotope Labeling. *Nano Letters*, **2009,** *9* (12), 4268-4272.

67.	Wassei, J. K.; Kaner, R. B., Graphene, a Promising Transparent Conductor. *Materials today*, **2010,** *13* (3), 52-59.

68.	Jiang, J.-W.; Wang, J.-S.; Li, B., Young's Modulus of Graphene: A Molecular Dynamics Study. *Physical Review B*, **2009,** *80* (11), 113405.

69.	Lee, C.; Wei, X.; Kysar, J. W.; Hone, J., Measurement of the Elastic Properties and Intrinsic Strength of Monolayer Graphene. *Science*, **2008,** *321* (5887), 385-388.

70.	Li, J.; Hu, L.; Wang, L.; Zhou, Y.; Grüner, G.; Marks, T. J., Organic Light-Emitting Diodes Having Carbon Nanotube Anodes. *Nano Letters*, **2006,** *6* (11), 2472-2477.

71.	Gruner, G., Carbon Nanotube Films for Transparent and Plastic Electronics. *Journal of Materials Chemistry*, **2006,** *16* (35), 3533-3539.

72.	Charton, C.; Fahland, M., Optical Properties of Thin Ag Films Deposited by Magnetron Sputtering. *Surface and Coatings Technology*, **2003,** *174–175*, 181-186.

73.	Kim, D.-H.; Park, M.-R.; Lee, H.-J.; Lee, G.-H., Thickness Dependence of Electrical Properties of Ito Film Deposited on a Plastic Substrate by Rf Magnetron Sputtering. *Applied Surface Science*, **2006,** *253* (2), 409-411.

74.	Camacho, J. M.; Oliva, A. I., Surface and Grain Boundary Contributions in the Electrical Resistivity of Metallic Nanofilms. *Thin Solid Films*, **2006,** *515* (4), 1881-1885.

75. O'Connor, B.; Haughn, C.; An, K.-H.; Pipe, K. P.; Shtein, M., Transparent and Conductive Electrodes Based on Unpatterned, Thin Metal Films. *Applied Physics Letters*, **2008,** *93* (22), 223304.

76. Blake, P.; Hill, E. W.; Castro Neto, A. H.; Novoselov, K. S.; Jiang, D.; Yang, R.; Booth, T. J.; Geim, A. K., Making Graphene Visible. *Applied Physics Letters*, **2007,** *91* (6), 063124.

77. Nair, R. R.; Blake, P.; Grigorenko, A. N.; Novoselov, K. S.; Booth, T. J.; Stauber, T.; Peres, N. M. R.; Geim, A. K., Fine Structure Constant Defines Visual Transparency of Graphene. *Science*, **2008,** *320* (5881), 1308-1308.

78. Ni, Z. H.; Wang, H. M.; Kasim, J.; Fan, H. M.; Yu, T.; Wu, Y. H.; Feng, Y. P.; Shen, Z. X., Graphene Thickness Determination Using Reflection and Contrast Spectroscopy. *Nano Letters*, **2007,** *7* (9), 2758-2763.

79. Partoens, B.; Peeters, F. M., From Graphene to Graphite: Electronic Structure around the K Point. *Physical Review B*, **2006,** *74* (7), 075404.

80. Chan, I. M.; Hong, F. C.-N., Plasma Treatments of Indium Tin Oxide Anodes in Carbon Tetrafluorinde (Cf4)/Oxygen (O2) to Improve the Performance of Organic Light-Emitting Diodes. *Thin Solid Films*, **2003,** *444* (1–2), 254-259.

81. Jesuraj, P. J.; Parameshwari, R.; Kanthasamy, K.; Koch, J.; Pfnür, H.; Jeganathan, K., Hole Injection Enhancement in Organic Light Emitting Devices Using Plasma Treated Graphene Oxide. *Applied Surface Science*, **2017,** *397*, 144-151.

82. Roll-to-Roll Production of 30-Inch Graphene Films for Transparent Electrodes. *Nature Nanotechnology*, **2010,** *5*, 574.

83. Kang, J.; Shin, D.; Bae, S.; Hong, B. H., Graphene Transfer: Key for Applications. *Nanoscale*, **2012,** *4* (18), 5527-5537.

84. Helander, M. G.; Wang, Z. B.; Qiu, J.; Greiner, M. T.; Puzzo, D. P.; Liu, Z. W.; Lu, Z. H., Chlorinated Indium Tin Oxide Electrodes with High Work Function for Organic Device Compatibility. *Science*, **2011,** *332* (6032), 944-947.

85. Ok, K.-H.; Kim, J.; Park, S.-R.; Kim, Y.; Lee, C.-J.; Hong, S.-J.; Kwak, M.-G.; Kim, N.; Han, C. J.; Kim, J.-W., Ultra-Thin and Smooth Transparent Electrode for Flexible and Leakage-Free Organic Light-Emitting Diodes. *Scientific Reports*, **2015,** *5*, 9464.

86. Chen, J.; Bi, H.; Sun, S.; Tang, Y.; Zhao, W.; Lin, T.; Wan, D.; Huang, F.; Zhou, X.; Xie, X.; Jiang, M., Highly Conductive and Flexible Paper of 1d Silver-Nanowire-Doped Graphene. *ACS Applied Materials & Interfaces*, **2013,** *5* (4), 1408-1413.

87. Al-Mamun, M.; Kim, J.-Y.; Sung, Y.-E.; Lee, J.-J.; Kim, S.-R., Pt and Tco Free Hybrid Bilayer Silver Nanowire–Graphene Counter Electrode for Dye-Sensitized Solar Cells. *Chemical Physics Letters*, **2013,** *561–562*, 115-119.

88. Tien, H.-W.; Hsiao, S.-T.; Liao, W.-H.; Yu, Y.-H.; Lin, F.-C.; Wang, Y.-S.; Li, S.-M.; Ma, C.-C. M., Using Self-Assembly to Prepare a Graphene-Silver Nanowire Hybrid Film That Is Transparent and Electrically Conductive. *Carbon*, **2013,** *58*, 198-207.

89. Choi, H. O.; Yang, S. B.; Min, B. H.; Kim, D. W.; Cho, K. M.; Jung, H.-T., Solution-Processable Graphene-Silver Nanowire Hybrids as Transparent Conducting Films. *Science of Advanced Materials*, **2014,** *6* (11), 2304-2311.

90. Dong, H.; Wu, Z.; Jiang, Y.; Liu, W.; Li, X.; Jiao, B.; Abbas, W.; Hou, X., A Flexible and Thin Graphene/Silver Nanowires/Polymer Hybrid Transparent Electrode for Optoelectronic Devices. *ACS Applied Materials & Interfaces*, **2016,** *8* (45), 31212-31221.

91. Zhang, Q.; Di, Y.; Huard, C. M.; Guo, L. J.; Wei, J.; Guo, J., Highly Stable and Stretchable Graphene-Polymer Processed Silver Nanowires Hybrid Electrodes for Flexible Displays. *Journal of Materials Chemistry C*, **2015,** *3* (7), 1528-1536.

92. Moon, I. K.; Kim, J. I.; Lee, H.; Hur, K.; Kim, W. C.; Lee, H., 2d Graphene Oxide Nanosheets as an Adhesive over-Coating Layer for Flexible Transparent Conductive Electrodes. *Scientific Reports*, **2013,** *3*, 1112.

93. Xu, S.; Man, B.; Jiang, S.; Liu, M.; Yang, C.; Chen, C.; Zhang, C., Graphene-Silver Nanowire Hybrid Films as Electrodes for Transparent and Flexible Loudspeakers. *CrystEngComm*, **2014,** *16* (17), 3532-3539.

94. Mankowski, T.; Zhu, Z.; Balakrishnan, K.; Shikoh, A. S.; Touati, F.; Benammar, M.; Mansuripur, M.; Falco, C. M. In *Metal Nanowire-Graphene Composite Transparent Electrodes*, 2014; pp 91770I-91770I-6.

95. Park, B.; Bae, I.-G.; Huh, Y. H., Aligned Silver Nanowire-Based Transparent Electrodes for Engineering Polarisation-Selective Optoelectronics. *Scientific Reports*, **2016,** *6*, 19485.

96. Meyer, J.; Kidambi, P. R.; Bayer, B. C.; Weijtens, C.; Kuhn, A.; Centeno, A.; Pesquera, A.; Zurutuza, A.; Robertson, J.; Hofmann, S., Metal Oxide Induced Charge Transfer Doping and Band Alignment of Graphene Electrodes for Efficient Organic Light Emitting Diodes. *Scientific Reports*, **2014,** *4*, 5380.

97. Zhang, Y.; Tan, Y.-W.; Stormer, H. L.; Kim, P., Experimental Observation of the Quantum Hall Effect and Berry's Phase in Graphene. *Nature*, **2005,** *438* (7065), 201-204.

Chapter 3   Graphene Synthesis & Transfer

3.1   Introduction

At present to realise the commercial exploitation of graphene in large-area applications, such as displays and solar cells, large area graphene must be synthesised and transferred onto a range of arbitrary substrates. This chapter focuses on the transfer of large-area CVD graphene. Before the introduction of new approaches, the following sections report conventional ways to produce and transfer graphene. What follows is the author's developed transfer approaches for large-area graphene as a means of overcoming many of the limitations associated with conventional transfer methods.

3.2   Graphene Isolation & Synthesis

3.2.1   Mechanical Exfoliation

Graphene has been isolated and synthesised in various ways on many different substrates. As the first production of graphene, Novoselov *et. al.*'s study used 3M scotch tape to exfoliate and therein isolate graphene from highly oriented pyrolytic graphite (HOPG), a process which was latterly termed mechanical exfoliation.[1] Possibly one of the simplest approaches to date, this approach exploits the weakly adhered, layered structure of graphite by easily peeling off each graphene layer. This method is still used by many research groups although it has a variety of limitations.[2-7]

Mechanical exfoliation cannot produce large area uniform monolayer graphene. The graphene exfoliated from HOPG using the scotch tape splits into small pieces (diameter <500 μm), as shown in **Figure 3.1** resulting in non-contiguous layers.[8-9] Huang *et. al.* suggested a modified mechanical exfoliation approach.[9] They claimed that the key for producing a large graphene flake is the degree of adhesion between the flake and substrate surface. Consequently, in their efforts they included a substrate cleaning stage using oxygen plasma prior to contacting their graphite-loaded tape. Then, the loaded graphite was annealed for 2 – 5 min at 100°C in air on a hot plate. After the sample was cooled to room temperature the loaded graphite scotch tape was peeled off. They obtained larger graphene flakes compared to standard exfoliation methods, nonetheless the largest flake they achieved was of the order of 300 μm x 500 μm (**Figure 3.1** (d)) - still too small to be used in large area flexible electronics. The mechanical exfoliation method produces only small graphene fragments rather than the large-area monolayer graphene required.
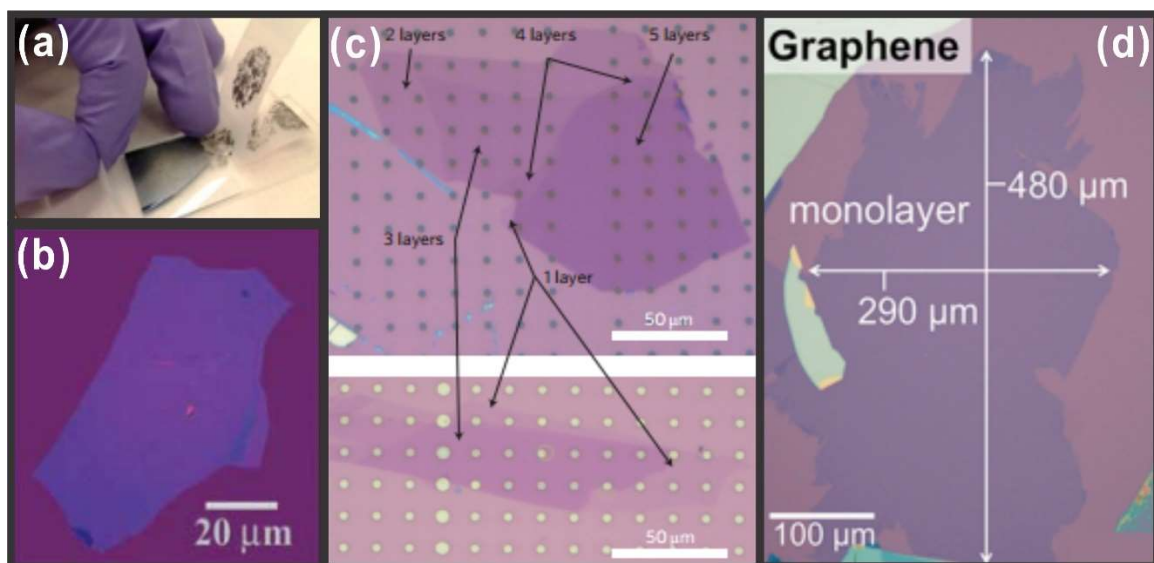
Figure 3.1 (a) A photograph demonstrating mechanical exfoliation of graphene using a scotch tape,[9] (b) a microscopic optical image of a graphene flake on an SiO₂/Si substrate,[1] (c) optical images of one layer to five layers of graphene on SiO₂,[2] and (d) an optical image of a monolayer graphene flake with modified mechanical exfoliation method including oxygen plasma and annealing processes.[9] Adapted from [1-2, 9] .

3.2.2 Liquid Phase Production

Several methods have been developed for the preparation of graphene in the liquid phase. [8, 10-14] Lee *et. al.* implemented graphene as a channel, gate source and drain electrodes in one of the first all-graphene FETs where they used multilayer-graphene oxide (GO) as a gate insulator which exhibited a dielectric constant of 3.1 (at 77K) and a surprisingly low leakage current (17 mA/cm^2).[10] The GO was coated using a Langmuir-Blodgett process, as illustrated in **Figure 3.2** (a). The GO flakes were dispersed in an aqueous phase; hexane was poured on the surface of the water, and ethanol was added to decrease the surface charge of the GO flakes. The decrease in interfacial energy at the immiscible water/hexane interface generates a capillary force which is strong relative to the gravitational force. This attracts and retains the GO flakes. [10, 15] The spontaneous evaporation of hexane leaves two-dimensional GO films floating on the water's uppermost surface. These are then scooped out onto any destination substrate. Authors argued that the GO flakes on the water surface were attached to each other and formed a continuous layer, as shown in **Figure 3.2** (b) and (c).[10] This is highly unlikely. Chemical exfoliation has been attempted for fabricating modified graphene such as GO and functionalised graphene.[16-18] However, such materials are not genuine monolayers and are rich in structural defects. [8, 18]
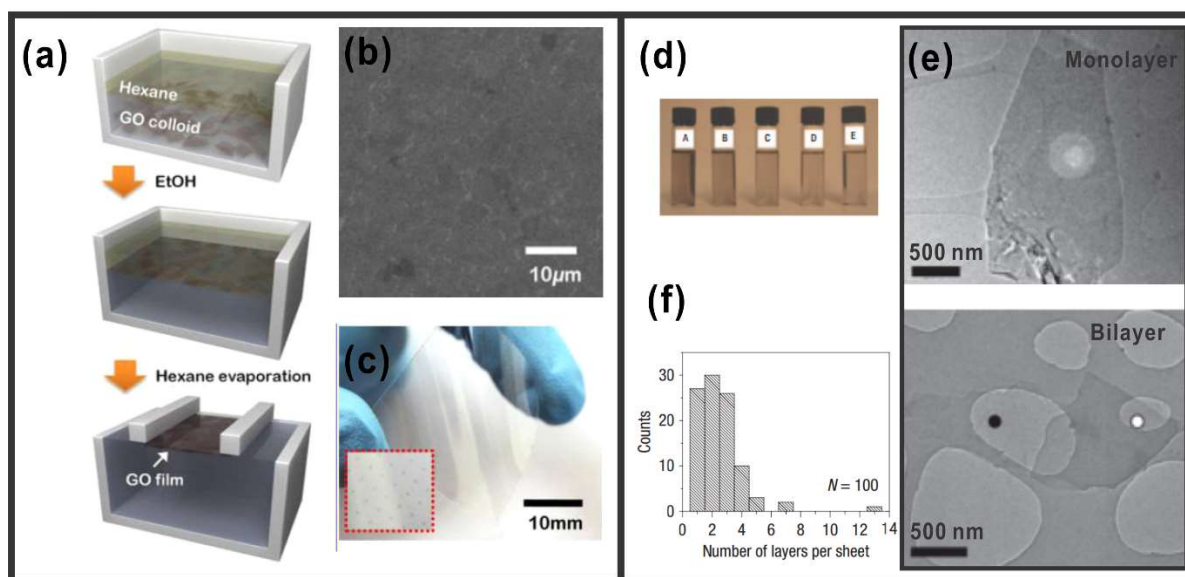
Figure 3.2 (a) schematics of the GO film formation process at the hexane/water interface, (b) SEM and (c) photographic image of GO film produced by chemical exfoliation using Langmuir Blodgett process, (d) graphene flake solved in N-methyl-pyrrolidone, (e) high-resolution transmission electron microscopy (TEM) images of solution-cast monolayer and bilayer of graphene, and (f) a histogram of the number of layers of spray-coated graphene on SiO_2. Adapted from [8, 10].

Coleman *et. al.* reported on the high yield production of graphene by sonication assisted liquid phase exfoliation.[8] As a chemical exfoliation method, they demonstrated graphene dispersion and exfoliation of graphite in an organic solvent; N-methyl-pyrrolidone. **Figure 3.2** (d) shows the graphite flakes in N-methyl-pyrrolidone for a range of concentrations from 6 μg/ml to 4 μg/ml. **Figure 3.2** (e) shows high-resolution transmission electron microscopy (TEM) images of monolayer and bilayer graphene produced by this solution based process. To prepare the samples, the graphene-flake solution was spin-coated after sonication for 30 min and annealed under forming gas at 400˚C for 4 hours to remove residual solvents.[8] The approach was an early confirmation that graphene can be dispersed, spray-coated or ink-jet printed via liquid phase processing. Nevertheless, it was not directly possible to control the number of layers with the produced films consisting of monolayers to multilayers, as shown in the TEM images (**Figure 3.2** (e)) and layer number histogram (**Figure 3.2** (f)).

Inkjet printing-based fabrication has been developed for graphene devices because it is rapid and cheap, without requiring high temperature annealing. This makes it possible to print on polymer substrates as a means of realising flexible electronics.[19-21] Torrisi *et. al.* fabricated a FET using graphene ink made with graphite flakes ultrasonicated in N-methane-pyrrolidone for 9 hours, as described in **Figure 3.3** (a). The samples were ultra-centrifuged at 10,000 rpm for an hour following filtration, to remove flakes > 1µm which might clog the nozzle.[22-23] They treated SiO_2 substrate with oxygen plasma and hexamethyldisilazane (HMDS), a common adhesion promoter, to improve wettability on the surface of the substrate before printing of the graphene ink. The fabricated FET with printed graphene channel layer exhibits on/off ratios of around 10 and field effect mobility of 95 cm^2/Vs.
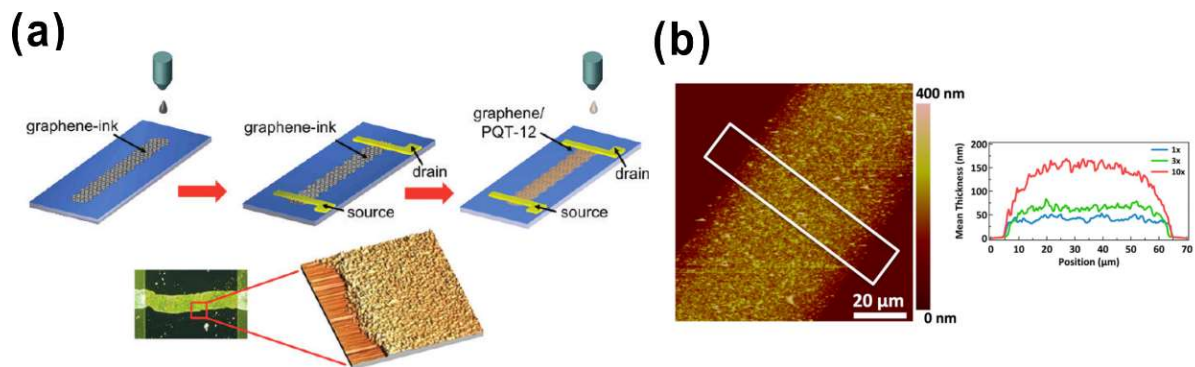
Figure 3.3 (a) A diagram of fabrication of FET using graphene ink printed on SiO₂ and an AFM image of the printed graphene ink, and (b) an AFM image and cross-sectional profile of a printed graphene line. Adapted from [20, 22].

Despite the fast and reproducible fabrication process of inkjet-printed graphene, flake sizes remain < 1 µm[22, 24-25]; the nozzle size ultimately restricts the maximum flake size. The printed ink is not monolayer, but rather a combination of multilayers, as seen in AFM images in **Figure 3.3** (b) resulting in spatially non-uniform electrical properties.

3.2.3 CVD Graphene for Large-Area Electronics

Chemical vapour deposition (CVD) has come to the fore as one of the few commercially viable large area deposition approaches. Rapid progress has been made this past five years on the CVD of graphene; very high quality and large-area graphene sheets can now be synthesised with ease on various metal catalyst surfaces.[26-31] Bottom-up CVD synthesis can scale up the synthesis with the maximum size only depending on the surface area of the catalytic material loaded into the CVD chamber.[27, 32-34] CVD offers accurate control over the growth rate by proxy control of the gas flow, pressure and chamber temperature.[35]
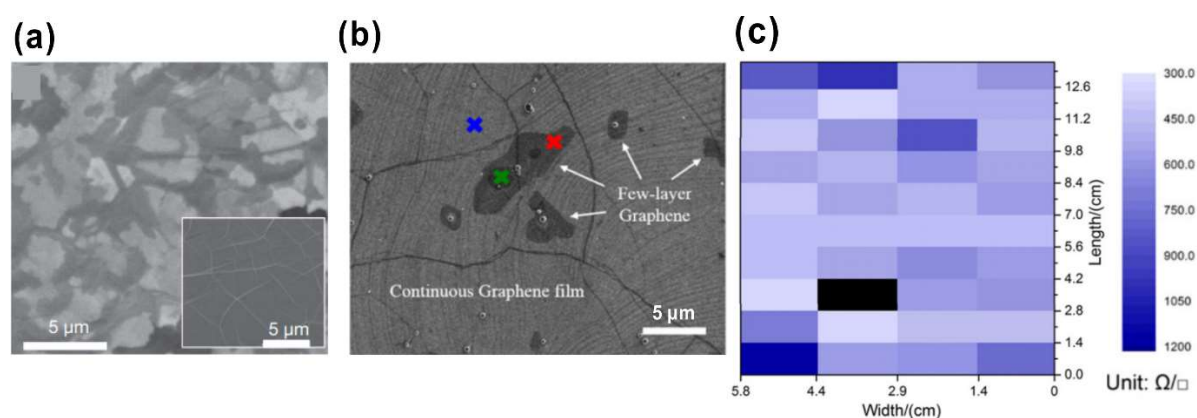
Figure 3.4 SEM images of (a) as-grown graphene films on thin Ni layers (300 nm) and (b) the continuous graphene films transferred from Cu foil onto SiO₂ substrate (300 nm), and (c) spatial distribution of sheet resistance of the CVD graphene sample. Adapted from [36-37]**.**

The properties of the resulting graphene films are strongly related to the growth mechanisms which themselves relate to the catalyst material of choice.[38] For Ni catalysts, hydrocarbon atoms diffuse into the Ni at an increasing rate, peaking at around 1000 ˚C. Graphene grows on the Ni when an appropriate cooling rate is adopted stimulating the high carbon concentration within the Ni catalyst to freeze out, and crystallise to form graphene.[37-38] For graphene on Cu, the growth mechanism is somewhat different from materials such as Ni and other transition metals in that Cu has an especially low carbon diffusion. The carbon atoms which are pyrolysed from the carbon feedstock; commonly methane (CH_4) gas diffuse little in the bulk Cu but rather crystallise immediately on the Cu surface.[35-36, 39] These initial

42

adsorbed carbon atoms, along with defects in the Cu lattice, act as growth seeds, with additional carbons bonding at these seed-sites. Graphene films grown using CVD show continuous monolayer coverage with over 90 % coverage being commonplace, as shown in the SEM images of **Figure 3.4** (a) and (b).[36-37, 40-41] The gain size of CVD graphene has also been significantly increased as the number of nucleation at the initial stage of CVD could be reduced by controlling the surface roughness of metallic catalysts.[42-43] **Figure 3.4** (c) shows the spatial distribution of R_S of bilayer CVD graphene after transfer onto a PET substrate (6 cm x 14 cm) using PMMA-transfer technique. The average value of the R_S was 808.2 Ω/sq. with a standard deviation, 197.5 Ω/sq.[37] This results indicates that CVD graphene is an especially promising approach for the realisation of large-area electronics necessitating uniform electrical properties.

3.3   Conventional Transfer Methods

Although the optical and electrical continuity of CVD graphene shows much merit, the primary limitation preventing the wider-scale adoption of CVD-based graphene-technologies is that it must be transferred to arbitrary substrates from its opaque conducting catalyst. The transfer method is crucial in realising useful devices as it intimately dictates the final device conductivity and transparency.

3.3.1   Transfer Using Polymer Support Layers

Soft transfer processes must be developed as the native quality of CVD graphene can be readily deteriorated through aggressive transfer processes. Perhaps the most commonly employed transfer method to date is that where the graphene is supported by a polymer handler, such as poly-methyl methacrylate (PMMA) or polydimethylsiloxane (PDMS), while the catalyst is chemically etched.[36, 40, 44-46]

Kim *et. al.* reported one of the first successes of this technique in their study on the transfer of graphene onto stretchable substrates.[36] Here they synthesised graphene using CVD on Ni.

The graphene was patterned using argon plasma, and transferred onto a SiO_2 substrate using PDMS (polydimethylsiloxane). As described in **Figure 3.5**, this study used soft-lithography as commonly used in the display field. The graphene attached on the surface of the PDMS was stamped onto a prepared SiO_2 substrate after the Ni catalyst was etched in aqueous $FeCl_3$. Graphene was released from the PDMS since the surface free energy of the SiO_2 substrate was higher than that of the PDMS. Another way to transfer graphene from Ni to SiO_2 is by etching the SiO_2 under the Ni using a Buffered Oxide Etchant (BOE) and then, etching the Ni using Hydrogen Fluoride (HF). The transferred graphene films show very low sheet resistance of 280 Ω/sq., with 80 % optical transparency.[36]
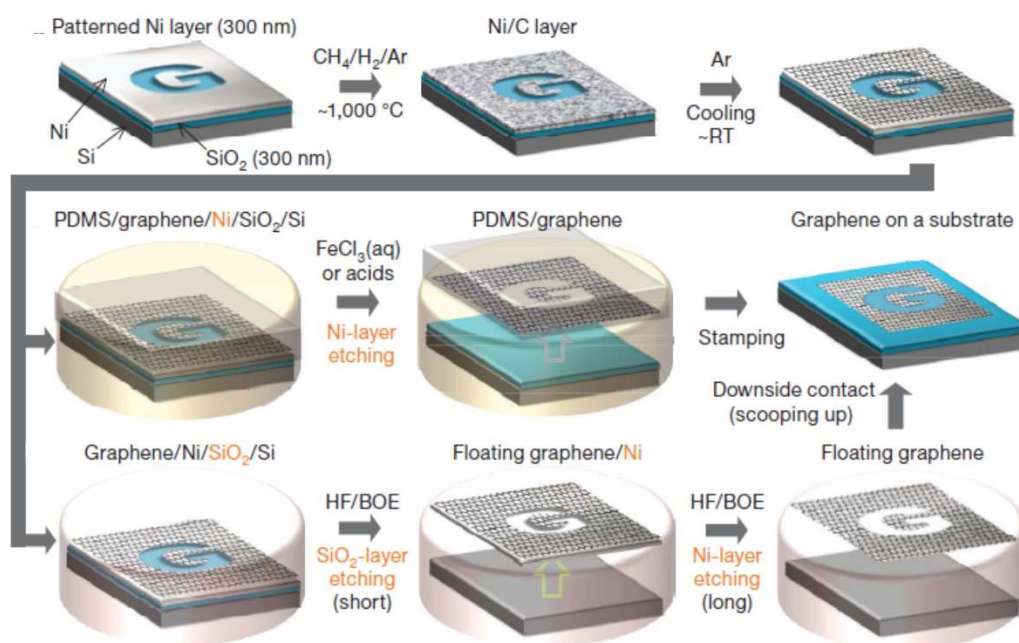
Figure 3.5 A schematic of synthesis, etching and transfer using PDMS supporter for the large scale and patterned graphene films. Adapted from [36].

PMMA is perhaps the most widely used polymer support for CVD graphene transfer. Unlike PDMS, which maintains weak van der Waals forces with graphene, PMMA coatings form covalent bonds with the graphene basal plane.[44] This is one advantage of the PMMA-transfer method as the strong binding prevents graphene from tearing during catalyst-etching.

The standard PMMA transfer approach has been modified and finessed by many research groups to improve the quality of transferred graphene. [44-45, 47-49] One optimised recipe for PMMA transfer is shown in **Figure 3.6**. As illustrated in **Figure 3.6** (a), PMMA is spin-coated at 3000 rpm for 35s onto as-grown graphene on its metallic catalyst. The coated PMMA is baked at 180 ˚C for 30 - 60s to ensure crosslinking to provide strong adhesion onto the graphene. It was found that the baking time affects the PMMA residue after the transfer processes. An overly extended bake time results in more PMMA residues.[47-48] It is critical that the baking time be optimised. The PMMA acts as a support during the catalyst etching process in aqueous ammonium persulfate ((NH_4)$_2$$S_2$$O_8$), as shown in **Figure 3.6** (b). Before the etching process, the backside of catalyst material was treated with a mild O_2 plasma (50 W, 150 mTorr) for 20s to remove this low-quality backside graphene and therein expose the Cu catalyst and promote catalyst etching. After the catalyst was completely etched, the PMMA supported graphene was scooped up and transferred onto a target substrate (**Figure 3.6** (c)). The sample was then left in air for at least 12 hours to evaporate the water between the graphene and the destination substrate. During this process, the graphene adheres to the substrate via Van der Waals attractive forces. Finally, the PMMA is removed in an acetone bath for 5 – 10 hours. The graphene on the target substrate was subsequently annealed at 180 ˚C for 10 min in air to evaporate residual acetone and further enhance the adhesion of the graphene to the substrate (**Figure 3.6** (d) and (e)).
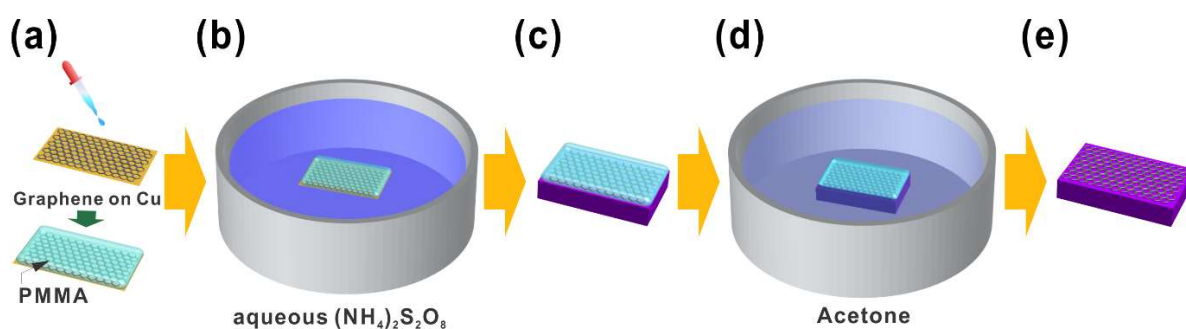
Figure 3.6 Schematic illustrations of the processes of graphene transfer using PMMA; (a) Coating and baking PMMA, (b) etching metallic catalyst, (c) scooping PMMA-supported graphene on a target substrate and drying out water in air, (d) removing away PMMA in acetone, and (e) washing out acetone and annealing.

The use of a polymer is attractive as, unlike rigid inorganic substrates, it is low cost, mechanically flexible and easily handled. Although polymers can transfer CVD-grown graphene without severe breakage or tearing, using an organic layer like PMMA can cause ripples or holes in weak single-layer graphene and the ripples can hamper full contact between graphene and substrates causing non-uniform transferring. Additionally, removing PMMA from the graphene after finishing the transfer is difficult and the PMMA residue can cause further degradation to the final films transport properties.

3.3.2   Transfer Using Thermal Release Tape

Polymer supported transfer is most likely to continue to be a popular method for laboratory scale graphene. However, handling PMMA/graphene on water surfaces requires skilled users and still results in low throughput and low yields, even from the most trained of users. Due to this the size of the transferred graphene is limited. The largest size of graphene transferred using PMMA is of the order of 10 cm x 10 cm; a laboratory level process. The transfer technique is not compatible with large area electronics in a mass-production context. Thermal release tape (TRT) can be used as an alternative to soft polymers.[50-52] Bae *et. al.* reported graphene transfer on large-area substrates (30 inch) using TRT in the first pseudo roll-to-roll process.[52] A scheme of this process is depicted in **Figure 3.7**. Firstly, the graphene on Cu was attached to TRT by passing through cold rollers. In the following step, the Cu was etched by aqueous ammonium persulphate solution ((NH_4)$_2S_2O_8$). Then, the graphene films were transferred from the TRT to a PET substrate. The TRT was removed by heating the rollers at high temperature (120˚C) causing the adhesion between the tape and the graphene to reduce to the extent where the two can be safely peeled apart.
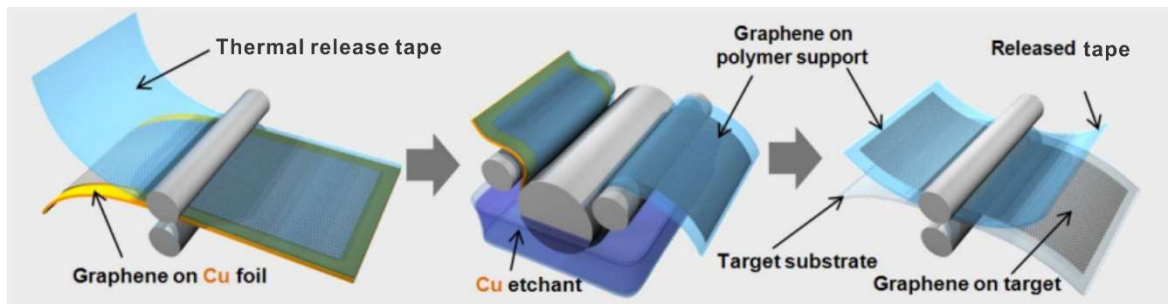
Figure 3.7 A schematic of roll to roll production of graphene films grown on a copper foil using thermal release tape. Adapted from [52].

The graphene sheet transferred using this method showed R_S as low as 125 Ω/sq. with 97 % optical transmittance after doping with 63 wt% HNO_3 for 5 min. The transfer method also allows them to transfer graphene layer by layer on the previously transferred graphene sheet resulting in the stacking of multilayers of graphene.[52] The rollers in the transfer method allowed for a high level of contact between the graphene and the tape, with the substrate at the final detaching step, otherwise the unattached regions of graphene tended to create holes, voids, and cracks that remain when the TRT was detached. Such contact issues were found to be exacerbated when a rigid substrate was used.
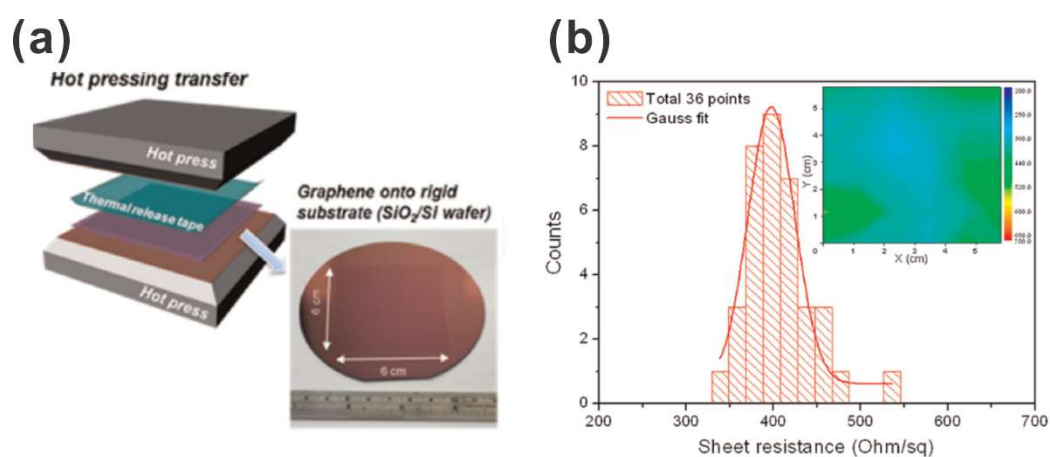
Figure 3.8 (a) A schematic of hot pressing transfer and (b) the R_S distribution transferred for three-layer graphene on a SiO₂ substrate. Adapted from [50].

The incomplete contact between the TRT and graphene generates undesired mechanical defects on the graphene when transferred by the roll-to-roll process. Kang *et. al.* developed a means of transferring large-area graphene films onto rigid substrates by hot pressing to provide better contact between the graphene and substrate.[50] The authors used TRT as a flexible polymer support to transfer graphene onto a SiO_2/Si wafer and a hot press machine rather than rollers to apply pressure when attaching the tape to the graphene and to detach it from graphene after transferring at high temperature. A schematic of the pressing transfer is shown in **Figure 3.8** (a). After etching the catalyst metal in aqueous $FeCl_3$ solution, the stacked layer of TRT/graphene/substrate was heated to 125°C at a pressure of 4 N/mm² for < 10 s. **Figure 3.8** (b) shows the R_S distribution of three-layers of graphene films transferred onto 6 cm x 6 cm SiO_2/Si wafer showing an average of 398 Ω/sq. with a standard deviation of 54 Ω/sq.[50]

Despite the fact that TRT transfer is simpler than PMMA transfer and is large area compatible, the incomplete contact of the TRT to the graphene can create cracks in the graphene and both PMMA and TRT leave notable residues.[52-55] Moreover, the transferred graphene using PMMA or TRT is attached on a substrate only by van der Waals attractive forces which are easily overcome. Such weak adhesion is a significant disadvantage when the

transferred graphene is to be used in flexible electronics that are intended to be exposed to repeated bending.

3.4   HPL & UVA Transfer

Weak interfacial adhesion of the graphene transferred onto a substrate using the polymer supported approaches, discussed above, remains a critical barrier in realising stable transfer for robust graphene-based thin film electronics. This thesis outlines the author's developments of two alternative transfer techniques (Hot-Press Lamination (HPL) and Ultra Violet Adhesive (UVA)-assisted transfer) both of which form strong adhesion between the graphene and substrates. Both of the proposed methods ensure mechanically stable graphene transfer with strong and long-lasting adhesion.

3.4.1   Method

Graphene was grown as reported in detail [56-57] using a commercially available Aixtron Black Magic Pro, hot-walled thermal CVD system on 25 μm Cu foil (99.999% Alfa Aesar) under 5 sccm CH_4 (99.5%) at 1000°C in Ar: H_2 (960 (99.9997%): 40 (99.9992%) sccm) at 25 mbar. Following 15-minute growth, samples were quenched under 2000 sccm N_2 (99.99%) to 250°C and were removed from the reactor. **Figure 3.9** shows a typical Raman spectrum (457 nm, Renishaw InVia) of the as-grown, graphene. The I_D/I_G ratio was 0.12 ± 0.05 suggesting high-quality graphene[58-59] and the I_{2D}/I_G ratio of 2.33 ± 0.6 was indicative of a bilayer material.[58-61] The full-width at half-maximum (FWHM) of the 2D peak was narrow; approximately 45-55 cm^{-1}, suggesting high graphitisation.[58-59]
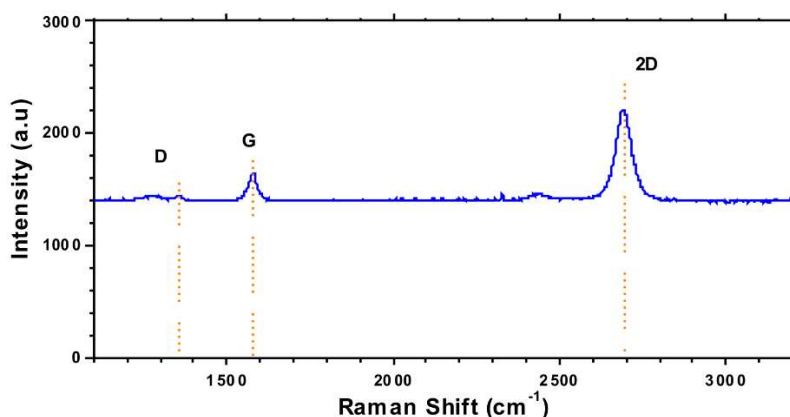
Figure 3.9 Raman spectra (457 nm) of the nascent Cu-foil catalysed graphene by thermal CVD.

Figure 3.10 (a) and (b) depict the HPL and UVA transfer methods, respectively. For HPL the graphene-on-catalyst was attached to commercially available thermally activated ethylene vinyl acetate (EVA) treated PET substrates (GBC Co.), herein termed a "laminate". As illustrated in **Figure 3.10** (a), first the as-synthesised graphene-on-catalyst was sandwiched between two EVA-PET (laminate) substrates (i), and then passed through a dual roller laminator, heated to 120℃ (ii). The backside EVA-PET was detached (iii), with the conformal graphene coating on this side being removed in the process. The now exposed Cu was then etched in $(NH_4)_2S_2O_8$ in de-ionized (DI) water (1 M) for 12 hours (iv). The PET-supported graphene samples were then rinsed with DI water and gently blow dried in ultra-high purity nitrogen (v). The transfer process is substrate invariant. It can be applied to a wide variety of polymeric substrates whose glass transition temperature is greater than the roller temperature.

50
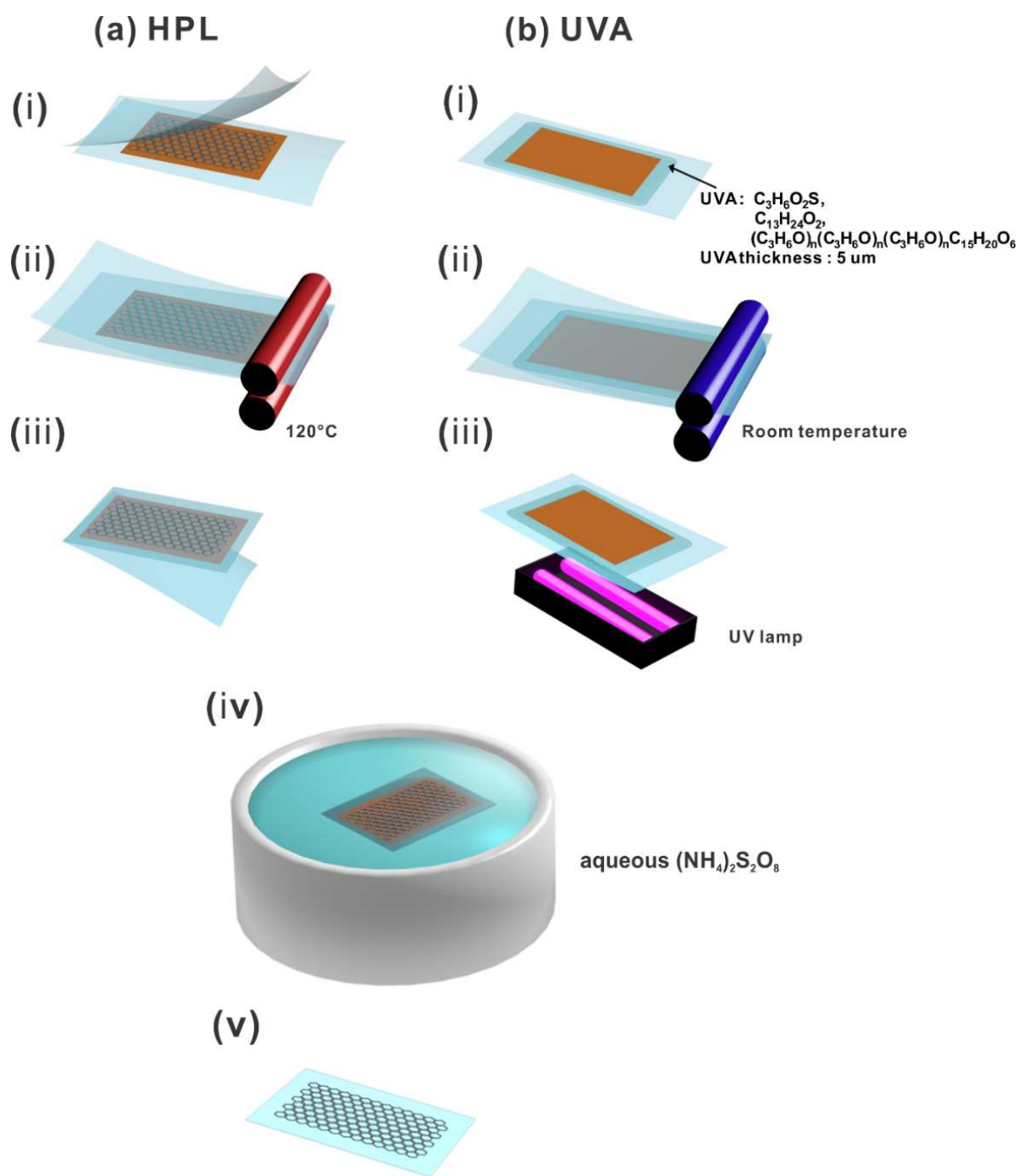
Figure 3.10 Schematic depiction of graphene transfer using (a) hot press lamination (HPL) and (b) UV-adhesive (UVA).

In the UV-assisted adhesive method, to chemically adhere the graphene I employ a UV-cured adhesive (Norland Co.), consisting of methyl thioglycoate ($C_3H_6O_2S$), isodecyl acrylate

($C_{13}H_{24}O_2$) and trimethylolpropane polypropylene glycol triacrylate (($C_3H_6O)_n(C_3H_6O)_n(C_3H_6O)_nC_{15}H_{20}O_6$). As illustrated in **Figure 3.10** (b), UVA was first coated onto the polymer substrate and the as-grown graphene-on-catalyst was placed in contact with the cast UVA (i). The sandwich was then compressed at 0.2 MPa using a cold-roll laminator, ensuring that all air pockets were removed to maximise the interface adhesion (ii). The UVA adhesive was cured by exposing the PET backside to a UV optical source (365 nm, 222 W/m^2) for 15 minutes (iii). Following UV curing, the Cu foil was etched in aqueous ($NH_4)_2S_2O_8$ for 12 hours (iv) and rinsed in DI water and dried in high-purity nitrogen, as before (v). Note that all UVA processing was undertaken at room temperature making the approach applicable to a wide range of polymer substrates. The suggested transfer approaches provide improved proximal contact between the graphene and the substrate which effectively prevents the formation of voids in the graphene following the transfer.

3.4.2 Electrical & Optical Properties

To attain a robust mechanical interface, the graphene requires proximal contact to the substrate.[62] In both transfer approaches, the as-grown graphene-on-catalyst achieves intimate contact with the EVA melt and to the low-viscosity UVA prior to curing. Photographs and energy-dispersive X-ray spectra (EDX) of the transferred graphene using the two approaches are shown in **Figure 3.11** (a) and (b), respectively. The EDX results suggest the absence of any Cu indicating that only the transferred carbon mediates the observed conductivity. The conductive carbon allotrope is most likely graphitic given the low transfer temperatures. In the case of the UVA-transferred graphene, there is some indication of sulphur (S), sourced most likely from the UV adhesive ($C_3H_6O_2S$, $C_{13}H_{24}O_2$, ($C_3H_6O)_n(C_3H_6O)_n(C_3H_6O)_nC_{15}H_{20}O_6$) under the graphene film. Sulphur is a known potent dopant of graphitic nanocarbons.[63-66] The Cu etching produces a significant unintentional, but nevertheless advantageous doping of the graphene prior to any further chemical treatments.
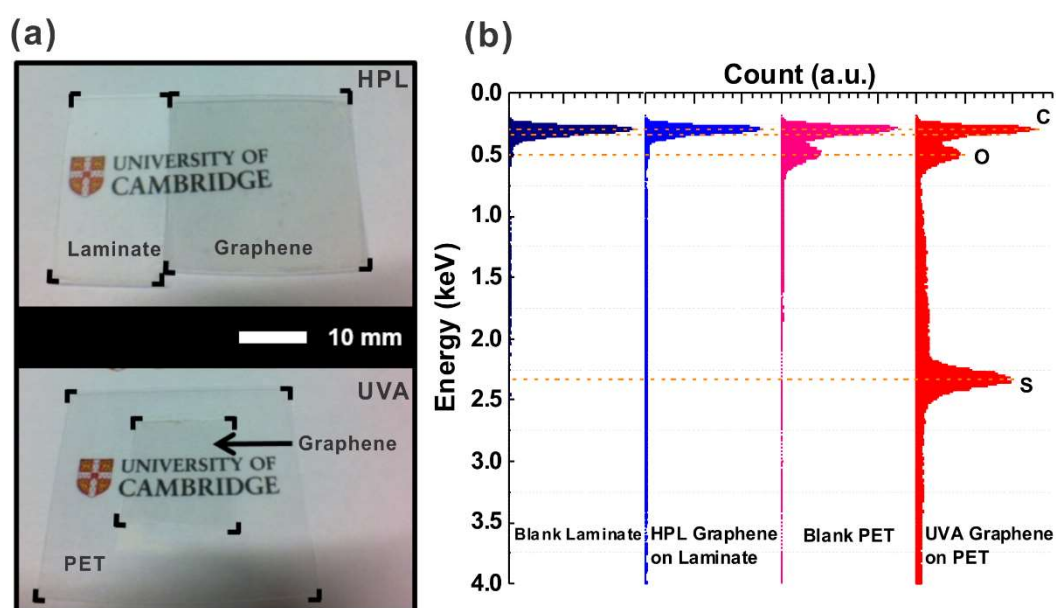
Figure 3.11 (a) Photographs of graphene transferred on PET using HPL (top) and UVA (bottom) transfer approaches and (b) energy-dispersive Xray spectroscopy (EDX) of a blank laminate (PET + EVA), a blank PET, and transferred graphene on the laminate and PET.

Figure 3.12 (a) shows the (ATI, Unicam UV2) optical transmittance spectra (%T) for graphene transferred using the two approaches. The transmittance of UVA-transferred graphene on PET and HPL-transferred graphene on laminate was 10 % and 12 % lower than the blank PET and blank laminate, respectively. These values are 7.7 % (UVA) - 11.7 % (HPL) higher than the theoretical light absorption of monolayer graphene 2.3%.[67-71] The unexpectedly high optical absorption might be attributed to the light absorption from 2 – 3 layers of graphene, the UV adhesive layer between the graphene and PET substrate or scattering effects associated with the substrate itself. Structural affects may also contribute; folding and wrinkling of the graphene during the transfer process could also decrease the %T by effectively increasing the mass density per unit area. As shown in **Figure 3.12** (b), the %T of the HPL graphene/laminate and UVA graphene/PET at 550 nm is 58.6±3.6 % and 76.5±3.8 %, respectively. The UVA transfer was around 18.1% more transparent than the HPL transfer, though both transfer techniques afforded an equivalent areal uniformity of < 4.0%.

53
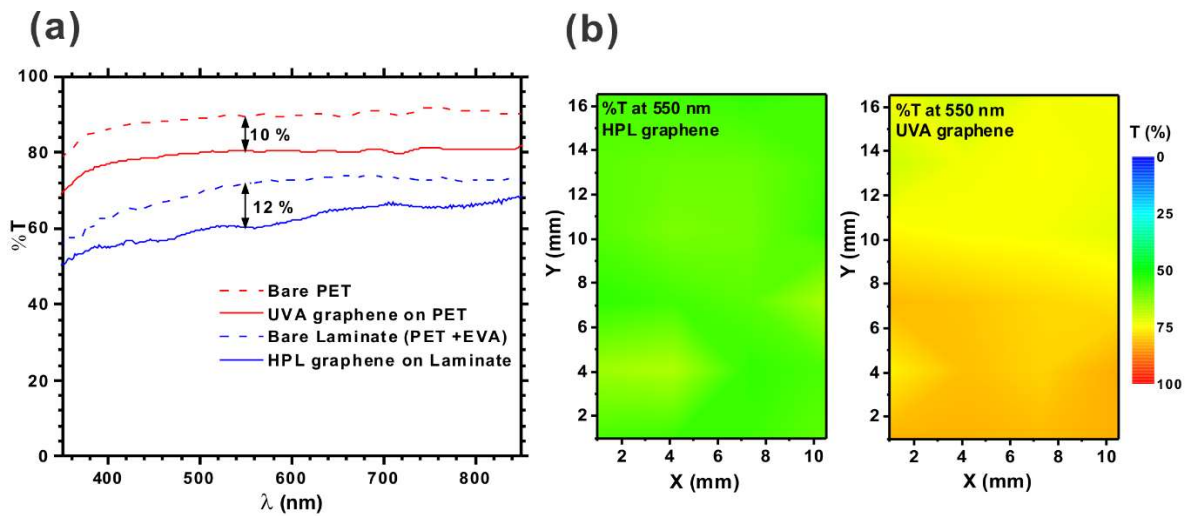
Figure 3.12 (a) Typical optical transmittance spectra and (b) optical transmittance distribution maps (550 nm) of HPL graphene on laminate and UVA graphene on PET.

The surface roughness measured by AFM (**Figure 3.13** (b)) indicated that HPL is more aggressive in terms of augmenting the morphology of the nascent two-dimensional crystal. The root mean square (RMS) surface roughness of the HPL graphene was 161 nm, some 26 % higher than the UVA graphene (119 nm). The maximum perturbation for HPL and UVA graphene was 949 nm and 551 nm, respectively. The spatial distribution of R_S (Jandel four-point probe) is shown in **Figure 3.13** (a). The R_S for the HPL transferred graphene on laminate samples was 9.9±3.8 kΩ/sq, whilst for the UVA graphene was 3.5±2.3 kΩ/sq. The growth and transfer process showed high reproducibility, though some slight variation in R_S and %T across sample sets was observed. The R_S of the as-grown graphene was assessed independently by transferring the as-grown material to quartz substrates using the conventional PMMA-approach, giving an R_S of 5.47±1.2 kΩ/sq. The HPL and UVA transferred samples showed an increase of 4.43 kΩ/sq. and, a decrease of 1.97 kΩ/sq. relative to the conventional PMMA approach, respectively. The decrease from UVA graphene may be attributed to the enhanced mass density associated with the closer contact between UVA graphene and PET substrate than between graphene and the quartz substrate. The UV-adhesive is a liquid of low room temperature viscosity (80 -95 cps).[72] Prior to curing by UV

exposure, it is this low viscosity that allows for near complete contact between the source graphene-on-catalsyt and the desitnation substrate.
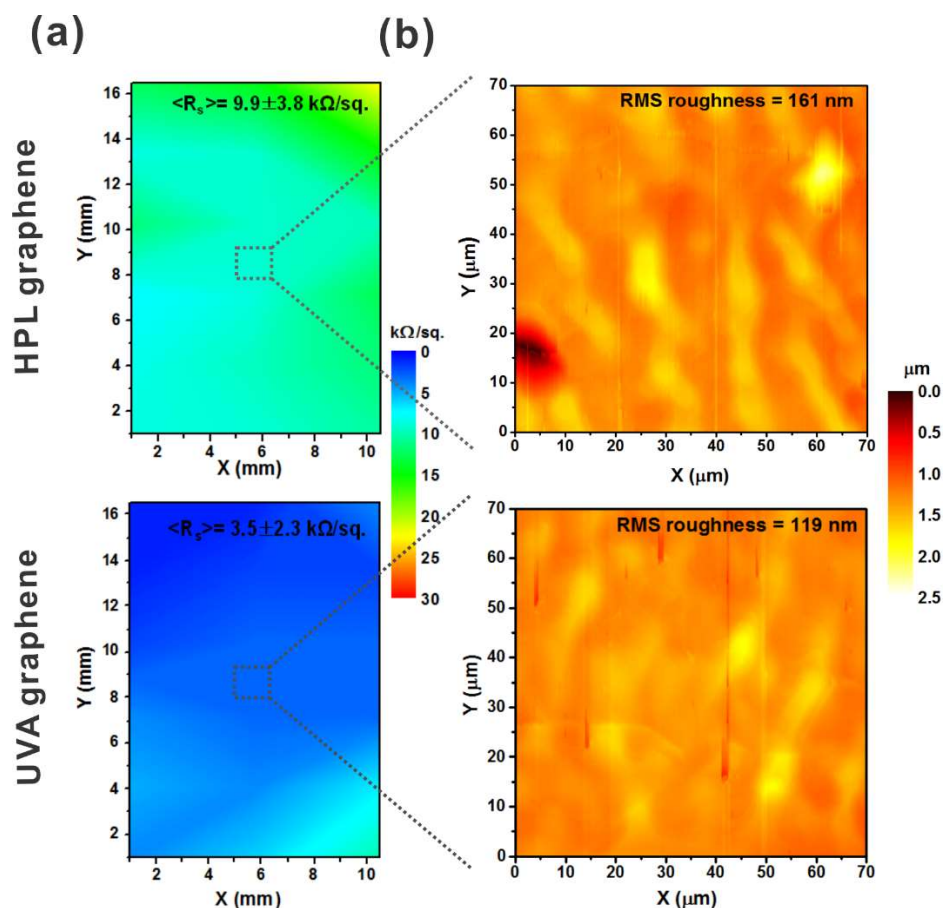
Figure 3.13 (a) Spatial distribution maps of R_S and (b) AFM micrographs of HPL-transferred graphene on laminate and UVA-transferred graphene on PET.

3.5   Summary

Full exploitation of the electrical properties of graphene require a method for the mass production of this remarkable material. CVD is considered as the key technique to realise large-area electronics using graphene. PMMA-transfer is the most widely used for laboratory scale graphene, but it has many varied problems with regards to commercialisation, such as

polymer residues, area limitations, and weak interfacial adhesion. To overcome these drawbacks, this thesis suggests two novel approaches to transfer graphene (HPL and UVA transfer). The R_S of HPL-transferred graphene showed ~4 kΩ/sq. higher, but UVA-transferred graphene showed ~2 kΩ/sq. lower R_S than conventional PMMA-transferred graphene. More in-depth analysis on the mechanical properties of the transferred graphene follow in the next chapter.

References

1.   Novoselov, K. S.; Geim, A. K.; Morozov, S. V.; Jiang, D.; Zhang, Y.; Dubonos, S. V.; Grigorieva, I. V.; Firsov, A. A., Electric Field Effect in Atomically Thin Carbon Films. *Science*, **2004,** *306* (5696), 666-669.

2.   Koenig, S. P.; Boddeti, N. G.; Dunn, M. L.; Bunch, J. S., Ultrastrong Adhesion of Graphene Membranes. *Nature Nano*, **2011,** *6* (9), 543-546.

3.   Koenig, S. P.; Wang, L.; Pellegrino, J.; Bunch, J. S., Selective Molecular Sieving through Porous Graphene. *Nature Nano*, **2012,** *7* (11), 728-732.

4.   Morozov, S. V.; Novoselov, K. S.; Katsnelson, M. I.; Schedin, F.; Elias, D. C.; Jaszczak, J. A.; Geim, A. K., Giant Intrinsic Carrier Mobilities in Graphene and Its Bilayer. *Physical Review Letters*, **2008,** *100* (1), 016602.

5.   Meyer, J. C.; Geim, A. K.; Katsnelson, M. I.; Novoselov, K. S.; Booth, T. J.; Roth, S., The Structure of Suspended Graphene Sheets. *Nature*, **2007,** *446* (7131), 60-63.

6.   Novoselov, K. S.; Geim, A. K.; Morozov, S. V.; Jiang, D.; Katsnelson, M. I.; Grigorieva, I. V.; Dubonos, S. V.; Firsov, A. A., Two-Dimensional Gas of Massless Dirac Fermions in Graphene. *Nature*, **2005,** *438* (7065), 197-200.

7.   Lee, C.; Wei, X.; Kysar, J. W.; Hone, J., Measurement of the Elastic Properties and Intrinsic Strength of Monolayer Graphene. *Science*, **2008,** *321* (5887), 385-388.

8.   Hernandez, Y.; Nicolosi, V.; Lotya, M.; Blighe, F. M.; Sun, Z.; De, S.; McGovern, I. T.; Holland, B.; Byrne, M.; Gun'Ko, Y. K.; Boland, J. J.; Niraj, P.; Duesberg, G.; Krishnamurthy, S.; Goodhue, R.; Hutchison, J.; Scardaci, V.; Ferrari, A. C.; Coleman, J. N., High-Yield Production of Graphene by Liquid-Phase Exfoliation of Graphite. *Nature Nano*, **2008,** *3* (9), 563-568.

9.   Huang, Y.; Sutter, E.; Shi, N. N.; Zheng, J.; Yang, T.; Englund, D.; Gao, H.-J.; Sutter, P., Reliable Exfoliation of Large-Area High-Quality Flakes of Graphene and Other Two-Dimensional Materials. *ACS Nano*, **2015,** *9* (11), 10612-10620.

10.   Lee, S. K.; Jang, H. Y.; Jang, S.; Choi, E.; Hong, B. H.; Lee, J.; Park, S.; Ahn, J. H., All Graphene-Based Thin Film Transistors on Flexible Plastic Substrates. *Nano Lett*, **2012,** *12* (7), 3472-6.

11.   Narita, A.; Verzhbitskiy, I. A.; Frederickx, W.; Mali, K. S.; Jensen, S. A.; Hansen, M. R.; Bonn, M.; De Feyter, S.; Casiraghi, C.; Feng, X.; Müllen, K., Bottom-up Synthesis of Liquid-Phase-Processable Graphene Nanoribbons with near-Infrared Absorption. *ACS Nano*, **2014,** *8* (11), 11622-11630.

12.   Quintana, M.; Tapia, J. I.; Prato, M., Liquid-Phase Exfoliated Graphene: Functionalization, Characterization, and Applications. *Beilstein Journal of Nanotechnology*, **2014,** *5*, 2328-2338.

13.   Güler, Ö.; Güler, S. H.; Selen, V.; Albayrak, M. G.; Evin, E., Production of Graphene Layer by Liquid-Phase Exfoliation with Low Sonication Power and Sonication Time from Synthesized Expanded Graphite. *Fullerenes, Nanotubes and Carbon Nanostructures*, **2016,** *24* (2), 123-127.

14.   Parvez, K.; Wu, Z.-S.; Li, R.; Liu, X.; Graf, R.; Feng, X.; Müllen, K., Exfoliation of Graphite into Graphene in Aqueous Solutions of Inorganic Salts. *Journal of the American Chemical Society*, **2014,** *136* (16), 6083-6091.

15.   Wang, Z.; Liu, Z.; Monne, M. A.; Wang, S.; Yu, Q.; Chen, M. Y., Interfacial Separation and Electrochemical Delamination of Cvd Grown Multilayer Graphene for Recyclable Use of Cu Powder. *RSC Advances*, **2016,** *6* (30), 24865-24870.

16.   Stankovich, S.; Dikin, D. A.; Dommett, G. H. B.; Kohlhaas, K. M.; Zimney, E. J.; Stach, E. A.; Piner, R. D.; Nguyen, S. T.; Ruoff, R. S., Graphene-Based Composite Materials. *Nature*, **2006,** *442* (7100), 282-286.

17.   Stankovich, S.; Dikin, D. A.; Piner, R. D.; Kohlhaas, K. A.; Kleinhammes, A.; Jia, Y.; Wu, Y.; Nguyen, S. T.; Ruoff, R. S., Synthesis of Graphene-Based Nanosheets Via Chemical Reduction of Exfoliated Graphite Oxide. *Carbon*, **2007,** *45* (7), 1558-1565.

18.   Niyogi, S.; Bekyarova, E.; Itkis, M. E.; McWilliams, J. L.; Hamon, M. A.; Haddon, R. C., Solution Properties of Graphite and Graphene. *Journal of the American Chemical Society*, **2006,** *128* (24), 7720-7721.

19.   Yang, W.; Wang, C., Graphene and the Related Conductive Inks for Flexible Electronics. *Journal of Materials Chemistry C*, **2016,** *4* (30), 7193-7207.

20.   Secor, E. B.; Prabhumirashi, P. L.; Puntambekar, K.; Geier, M. L.; Hersam, M. C., Inkjet Printing of High Conductivity, Flexible Graphene Patterns. *The Journal of Physical Chemistry Letters*, **2013,** *4* (8), 1347-1351.

21.   Li, J.; Ye, F.; Vaziri, S.; Muhammed, M.; Lemme, M. C.; Östling, M., Efficient Inkjet Printing of Graphene. *Advanced Materials*, **2013,** *25* (29), 3985-3992.

22.   Torrisi, F.; Hasan, T.; Wu, W.; Sun, Z.; Lombardo, A.; Kulmala, T. S.; Hsieh, G.-W.; Jung, S. M.; Bonaccorso, F.; Paul, P. J.; Chu, D. P.; Ferrari, A. C., Inkjet-Printed Graphene Electronics. *ACS Nano*, **2012,** *6* (4), 2992-3006.

23.   Xu, Y.; Hennig, I.; Freyberg, D.; Strudwick, A. J.; Schwab, M. G.; Weitz, T.; Cha, K. C.-P., Inkjet-Printed Energy Storage Device Using Graphene/Polyaniline Inks. *Journal of Power Sources*, **2014,** *248*, 483-488.

24.   Arapov, K.; Abbel, R.; de With, G.; Friedrich, H., Inkjet Printing of Graphene. *Faraday Discussions*, **2014,** *173* (0), 323-336.

25.   Capasso, A.; Del Rio Castillo, A. E.; Sun, H.; Ansaldo, A.; Pellegrini, V.; Bonaccorso, F., Ink-Jet Printing of Graphene for Flexible Electronics: An Environmentally-Friendly Approach. *Solid State Communications*, **2015,** *224*, 53-63.

26.   Li, X.; Magnuson, C. W.; Venugopal, A.; An, J.; Suk, J. W.; Han, B.; Borysiak, M.; Cai, W.; Velamakanni, A.; Zhu, Y.; Fu, L.; Vogel, E. M.; Voelkl, E.; Colombo, L.; Ruoff, R. S., Graphene Films with Large Domain Size by a Two-Step Chemical Vapor Deposition Process. *Nano Letters*, **2010,** *10* (11), 4328-4334.

27.   Kobayashi, T.; Bando, M.; Kimura, N.; Shimizu, K.; Kadono, K.; Umezu, N.; Miyahara, K.; Hayazaki, S.; Nagai, S.; Mizuguchi, Y.; Murakami, Y.; Hobara, D., Production of a 100-M-Long High-Quality Graphene Transparent Conductive Film by Roll-to-Roll Chemical Vapor Deposition and Transfer Process. *Applied Physics Letters*, **2013,** *102* (2), 023112.

28.   Obraztsov, A. N., Chemical Vapour Deposition: Making Graphene on a Large Scale. *Nature Nanotechnology*, **2009,** *4* (4), 212-213.

29.   Reina, A.; Jia, X.; Ho, J.; Nezich, D.; Son, H.; Bulovic, V.; Dresselhaus, M. S.; Kong, J., Large Area, Few-Layer Graphene Films on Arbitrary Substrates by Chemical Vapor Deposition. *Nano Letters*, **2008,** *9* (1), 30-35.

30.   Gomez De Arco, L.; Zhang, Y.; Schlenker, C. W.; Ryu, K.; Thompson, M. E.; Zhou, C., Continuous, Highly Flexible, and Transparent Graphene Films by Chemical Vapor Deposition for Organic Photovoltaics. *ACS Nano*, **2010,** *4* (5), 2865-2873.

31.   Li, X.; Magnuson, C. W.; Venugopal, A.; Tromp, R. M.; Hannon, J. B.; Vogel, E. M.; Colombo, L.; Ruoff, R. S., Large-Area Graphene Single Crystals Grown by Low-Pressure Chemical Vapor Deposition of Methane on Copper. *Journal of the American Chemical Society*, **2011,** *133* (9), 2816-2819.

32.   Feng, X., *Nanocarbons for Advanced Energy Storage*. Wiley: 2015.

33.   Chen, X.; Zhang, L.; Chen, S., Large Area Cvd Growth of Graphene. *Synthetic Metals*, **2015,** *210, Part A*, 95-108.

34.   Zhang, Y.; Zhang, L.; Zhou, C., Review of Chemical Vapor Deposition of Graphene and Related Applications. *Accounts of Chemical Research*, **2013,** *46* (10), 2329-2339.

35.   Nishi, Y.; Doering, R., *Handbook of Semiconductor Manufacturing Technology, Second Edition*. CRC Press: 2007.

36.   Kim, K. S.; Zhao, Y.; Jang, H.; Lee, S. Y.; Kim, J. M.; Kim, K. S.; Ahn, J. H.; Kim, P.; Choi, J. Y.; Hong, B. H., Large-Scale Pattern Growth of Graphene Films for Stretchable Transparent Electrodes. *Nature*, **2009,** *457* (7230), 706-710.

37.   Yuewen, S.; Youmin, R.; Zhengyu, H.; Ye, F.; Jamie, H. W., Uniformity of Large-Area Bilayer Graphene Grown by Chemical Vapor Deposition. *Nanotechnology*, **2015,** *26* (39), 395601.

38.   Jaeho, K.; Masatou, I.; Yoshinori, K.; Kazuo, T.; Masataka, H.; Sumio, I., Low-Temperature Synthesis of Large-Area Graphene-Based Transparent Conductive Films Using Surface Wave Plasma Chemical Vapor Deposition. *Applied Physics Letters*, **2011,** *98* (9), 091502.

39.   Li, X.; Cai, W.; Colombo, L.; Ruoff, R. S., Evolution of Graphene Growth on Ni and Cu by Carbon Isotope Labeling. *Nano Letters*, **2009,** *9* (12), 4268-4272.

40.   Li, X.; Cai, W.; An, J.; Kim, S.; Nah, J.; Yang, D.; Piner, R.; Velamakanni, A.; Jung, I.; Tutuc, E.; Banerjee, S. K.; Colombo, L.; Ruoff, R. S., Large-Area Synthesis of High-Quality and Uniform Graphene Films on Copper Foils. *Science,* **2009,** *324* (5932), 1312-1314.

41.   LEE, Y.; AHN, J.-H., Graphene-Based Transparent Conductive Films. *Nano,* **2013,** *08* (03), 1330001.

42.   Han, G. H.; Gunes, F.; Bae, J. J.; Kim, E. S.; Chae, S. J.; Shin, H.-J.; Choi, J.-Y.; Pribat, D.; Lee, Y. H., Influence of Copper Morphology in Forming Nucleation Seeds for Graphene Growth. *Nano Letters,* **2011,** *11* (10), 4144-4148.

43.   Lee, D.; Kwon, G. D.; Kim, J. H.; Moyen, E.; Lee, Y. H.; Baik, S.; Pribat, D., Significant Enhancement of the Electrical Transport Properties of Graphene Films by Controlling the Surface Roughness of Cu Foils before and During Chemical Vapor Deposition. *Nanoscale,* **2014,** *6* (21), 12943-12951.

44.   Kang, J.; Shin, D.; Bae, S.; Hong, B. H., Graphene Transfer: Key for Applications. *Nanoscale,* **2012,** *4* (18), 5527-5537.

45.   Suk, J. W.; Kitt, A.; Magnuson, C. W.; Hao, Y.; Ahmed, S. A.; An, J.; Swan, A. K.; Goldberg, B. B.; Ruoff, R. S., Transfer of Cvd-Grown Monolayer Graphene onto Arbitrary Substrates. *ACS Nano,* **2011,** *5* (9), 6916-6924.

46.   Hallam, T.; Wirtz, C.; Duesberg, G. S., Polymer-Assisted Transfer Printing of Graphene Composite Films. *Physica Status Solidi (b),* **2013,** *250* (12), 2668-2671.

47.   Borin Barin, G.; Song, Y.; de Fátima Gimenez, I.; Souza Filho, A. G.; Barreto, L. S.; Kong, J., Optimized Graphene Transfer: Influence of Polymethylmethacrylate (Pmma) Layer Concentration and Baking Time on Graphene Final Performance. *Carbon,* **2015,** *84*, 82-90.

48.   Jia, K.; Su, Y.; Zhan, J.; Shahzad, K.; Zhu, H.; Zhao, C.; Luo, J., Enhanced End-Contacts by Helium Ion Bombardment to Improve Graphene-Metal Contacts. *Nanomaterials,* **2016,** *6* (9), 158.

49.   Her, M.; Beams, R.; Novotny, L., Graphene Transfer with Reduced Residue. *Physics Letters A,* **2013,** *377* (21–22), 1455-1458.

50.   Kang, J.; Hwang, S.; Kim, J. H.; Kim, M. H.; Ryu, J.; Seo, S. J.; Hong, B. H.; Kim, M. K.; Choi, J.-B., Efficient Transfer of Large-Area Graphene Films onto Rigid Substrates by Hot Pressing. *ACS Nano,* **2012,** *6* (6), 5360-5365.

51.   Chen, T. L.; Ghosh, D. S.; Mkhitaryan, V.; Pruneri, V., Hybrid Transparent Conductive Film on Flexible Glass Formed by Hot-Pressing Graphene on a Silver Nanowire Mesh. *ACS Applied Materials & Interfaces,* **2013,** *5* (22), 11756-11761.

52.   Bae, S.; Kim, H.; Lee, Y.; Xu, X.; Park, J.-S.; Zheng, Y.; Balakrishnan, J.; Lei, T.; Ri Kim, H.; Song, Y. I.; Kim, Y.-J.; Kim, K. S.; Ozyilmaz, B.; Ahn, J.-H.; Hong, B. H.; Iijima, S., Roll-to-Roll Production of 30-Inch Graphene Films for Transparent Electrodes. *Nature Nano,* **2010,** *5* (8), 574-578.

53.   Chen, X.-D.; Liu, Z.-B.; Zheng, C.-Y.; Xing, F.; Yan, X.-Q.; Chen, Y.; Tian, J.-G., High-Quality and Efficient Transfer of Large-Area Graphene Films onto Different Substrates. *Carbon,* **2013,** *56*, 271-278.

54.   Wood, J. D.; Doidge, G. P.; Carrion, E. A.; Koepke, J. C.; Kaitz, J. A.; Datye, I.; Behnam, A.; Hewaparakrama, J.; Aruin, B.; Chen, Y., Annealing Free, Clean Graphene Transfer Using Alternative Polymer Scaffolds.

55.   Leclercq, J.; Sveshtarov, P., The Transfer of Graphene: A Review. *Bulgarian Journal of Physics,* **2016,** *43* (2).

56.   Li, C.; Cole, M. T.; Lei, W.; Qu, K.; Ying, K.; Zhang, Y.; Robertson, A. R.; Warner, J. H.; Ding, S.; Zhang, X.; Wang, B.; Milne, W. I., Highly Electron Transparent Graphene for Field Emission Triode Gates. *Advanced Functional Materials,* **2013**, 1228-1227.

57.   Kang, M. H.; Milne, W. I.; Cole, M. T., Doping Stability and Opto-Electronic Performance of Chemical Vapour Deposited Graphene on Transparent Flexible Substrates. *IET Circuits, Devices & Systems,* **2015,** *9* (1), 39-45.

58.   Ferrari, A. C.; Meyer, J. C.; Scardaci, V.; Casiraghi, C.; Lazzeri, M.; Mauri, F.; Piscanec, S.; Jiang, D.; Novoselov, K. S.; Roth, S.; Geim, A. K., Raman Spectrum of Graphene and Graphene Layers. *Physical Review Letters,* **2006,** *97* (18), 187401.

59.   Tang, B.; Guoxin, H.; Gao, H., Raman Spectroscopic Characterization of Graphene. *Applied Spectroscopy Reviews,* **2010,** *45* (5), 369-407.

60.   Torrisi, F.; Hasan, T.; Wu, W.; Sun, Z.; Lombardo, A.; Kulmala, T. S.; Hsieh, G.-W.; Jung, S.; Bonaccorso, F.; Paul, P. J.; Chu, D.; Ferrari, A. C., Inkjet-Printed Graphene Electronics. *ACS Nano,* **2012,** *6* (4), 2992-3006.

61.   Das, A.; Chakraborty, B.; Sood, A. K., Raman Spectroscopy of Graphene on Different Substrates and Influence of Defects. *Bulletin of Materials Science,* **2008,** *31* (3), 579-584.

62.   Martins, L. G.; Song, Y.; Zeng, T.; Dresselhaus, M. S.; Kong, J.; Araujo, P. T., Direct Transfer of Graphene onto Flexible Substrates. *Proc Natl Acad Sci U S A,* **2013,** *110* (44), 17762-7.

63.   Denis, P. A.; Faccio, R.; Mombru, A. W., Is It Possible to Dope Single-Walled Carbon Nanotubes and Graphene with Sulfur? *Chemphyschem,* **2009,** *10* (4), 715-722.

64.   Yang, Z.; Yao, Z.; Li, G.; Fang, G.; Nie, H., Sulfur-Doped Graphene as an Efficient Metal-Free Cathode Catalyst for Oxygen Reduction. *ACS nano,* **2012,** *6* (1), 205-211.

65.   Yang, Z.; Yao, Z.; Li, G.; Fang, G.; Nie, H.; Liu, Z.; Zhou, X.; Chen, X. a.; Huang, S., Sulfur-Doped Graphene as an Efficient Metal-Free Cathode Catalyst for Oxygen Reduction. *ACS Nano,* **2011,** *6* (1), 205-211.

66.   Park, J.-e.; Jang, Y. J.; Kim, Y. J.; Song, M.-s.; Yoon, S.; Kim, D. H.; Kim, S.-J., Sulfur-Doped Graphene as a Potential Alternative Metal-Free Electrocatalyst and Pt-Catalyst Supporting Material for Oxygen Reduction Reaction. *Physical Chemistry Chemical Physics,* **2014,** *16* (1), 103-109.

67.   Tsakmakidis, K., Coherent Absorption in Graphene. *Nature materials,* **2013,** *12* (8), 688-688.

68.   Lu, H.; Gan, X.; Jia, B.; Mao, D.; Zhao, J., Tunable High-Efficiency Light Absorption of Monolayer Graphene Via Tamm Plasmon Polaritons. *Optics Letters,* **2016,** *41* (20), 4743-4746.

69.   Zhu, J.; Liu, Q. H.; Lin, T., Manipulating Light Absorption of Graphene Using Plasmonic Nanoparticles. *Nanoscale,* **2013,** *5* (17), 7785-7789.

70.   Graphene. https://en.wikipedia.org/wiki/Graphene.

71.   Nair, R. R.; Blake, P.; Grigorenko, A. N.; Novoselov, K. S.; Booth, T. J.; Stauber, T.; Peres, N. M. R.; Geim, A. K., Fine Structure Constant Defines Visual Transparency of Graphene. *Science,* **2008,** *320* (5881), 1308-1308.

72.   *Norland   Optical   Adhesive.*   http://gentec-benelux.com/uv-cured-adhesives/acrylates/norland-adhesives/optical-adhesives/norland-optical-adhesive-74/ Gentec

Chapter 4   Mechanical Properties of UVA & HPL Transferred Graphene

4.1   Introduction

Graphene has attracted much attention for its use in transparent conducting electrodes in flexible electronics because the atomically thin layer allows for unique electrical properties upon flexing, coupled to a very high Young's modulus (~1 TPa).[1] Although graphene naturally has outstanding mechanical robustness,[2-3] it must still be transferred onto flexible substrates to be used in flexible electronics, as described above. The two transfer methods described in the previous chapter allow for robust adhesion via processes that are simple, fast, applicable to a wide range of substrates, have a high yield, and are large-area compatible at a low-cost per unit area. Perhaps most critically, the described transfer approaches provide strong adhesion between the graphene and the substrates thereby preserving many of the impressive opto-electro-mechanical properties of graphene. To prevent breakdown or performance degradation after repeated bending, the graphene must remain adhered to the substrate without delamination. Thus, the inspection of adhesion and bending fatigue stability are crucial for flexible applications of graphene.

Herein this thesis analyses the mechanical properties of the graphene attached to flexible substrates using both the UVA and HPL approaches. These properties are then compared to those of conventional PMMA-mediated transfer material. The mechanical and electrical stability of the UVA and HPL approaches are considered, as is the surface energy, adhesion potential, and bending stress stability. As illustrated in **Figure 4.1**, to confirm the functionality of the UVA and HPL transfer methods outlined above, three critical mechanical

properties of the transfer graphene on PET substrates were investigated; the interfacial adhesion between the graphene and the substrate (**Figure 4.1** (a)), the surface energy of the uppermost graphene surface (**Figure 4.1** (b)), and the bending fatigue stability (**Figure 4.1** (c)).
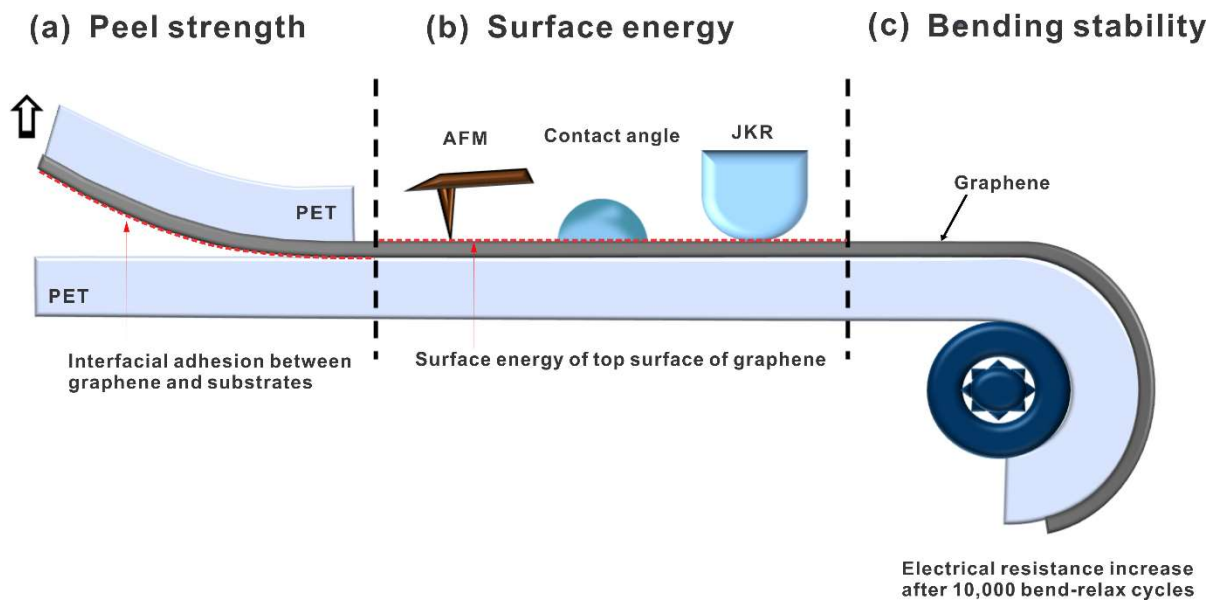
Figure 4.1 Analysis methods of mechanical properties of graphene on a PET substrate: (a) Interfacial adhesion between graphene and the substrate, (b) surface energy of top surface of graphene, and (c) bending stability of graphene after 10^4 bending cycles.

4.2 Surface Energy

The surface energy (γ) is a measure of the disruption of the intermolecular bonds that occurs when a surface is created.[4] It can be defined as the reversible work required to create a unit area of surface from a bulk material. In the case of a brittle material the work of cohesion, that is required to generate a unit area of separation, will be equal to 2γ.[4]

4.2.1 Pull-off Force

When a stress plane separates two disparate materials the theoretical work of adhesion can be thermodynamically defined as W_{12} [5], and is given by

$$W_{12} = \gamma_{S1} + \gamma_{S2} - \gamma_{12}$$ (4.1)

where subscripts S1 and S2 refer to the two materials and subscript 12 to the interface between them. If purely dispersive forces, as opposed to polar, are responsible for the interaction between materials 1 and 2 then[5]

$$W_{12} = 2\sqrt{\gamma_{S1}\gamma_{S2}}$$ (4.2)

The work of adhesion can then be estimated by measuring the pull-off force of a scanning AFM tip. Experimental values of the pull-off force account not only for interfacial bond rupture, i.e. W_{12} , but also any visco-elastic energy dissipation at the advancing crack tip. Thus, in many cases, the measured work of adhesion W_{ad} will be greater than W_{12}. The values of W_{12} thus places a lower bound on the work of adhesion W_{ad} .

In principle, direct measurements of adhesion can be carried out by loading a spherical indenter into contact with the surface and then measuring the tensile load required to break the adhesive contact. If both surfaces are rigid then the pull-off force (P_a) is given by the Bradley equation[6]

$$P_a = 2\pi R W_{ad}$$ (4.3)

and W_{ad} will be equal to W_{12}. When the surfaces show a linear elastic behaviour a finite circular contact spot will be generated during the compressive loading stage. In the absence of any energetic interactions, its radius is given by the Hertz relationship between the compressive load F and the systems elastic constant K .

$$a_H^3 = \frac{RF}{K} \quad \text{where} \quad \frac{1}{K} = \frac{3}{4}\left\{\frac{1-v_1^2}{E_1} + \frac{1-v_2^2}{E_2}\right\}$$

(4.4)

In the presence of adhesive effects the value of a will be enhanced and, provided both surfaces are of high moduli (as is the case in Atomic Force Microscopy) can be described by the relation, often attributed to DMT (the Derjaguin, Muller and Toporov technique), [7]

$$a_{DMT}^3 = \frac{R}{K}\left\{F + 2\pi RW_{12}\right\}$$

(4.5)

In this case the magnitude of the pull-off force, P_a is as given by equation (4.3). Under this theoretical framework the adhesion force in a 20 μm x 20 μm area was scanned via an AFM (Bruker's Dimension Icon).
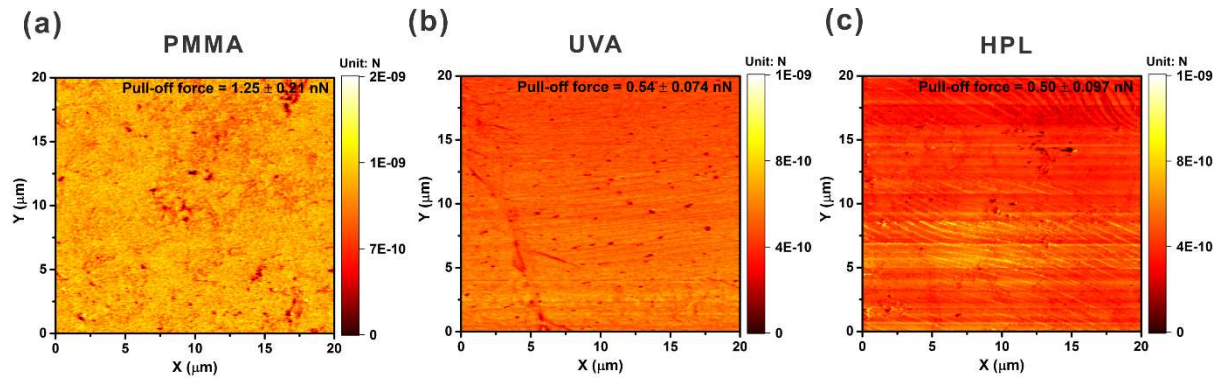
Figure 4.2 AFM pull-off forces for (a) PMMA-, (b) UVA-, (c) HPL-transferred graphene.

Figure 4.2 shows maps of the measured pull-off force from graphene transferred onto PET substrates by PMMA, UVA, and HPL. PMMA-transferred graphene has the highest adhesion (1.25 nN) with the largest standard deviation (±0.21 nN), highlighting its lack of spatial uniformity, whilst UVA (0.54±.074 nN) and HPL (0.502±.097 nN) showed similar values to one another, both some 58% lower than PMMA. The lower standard deviation associated

with these methods suggests improved spatial uniformity in the transfer process. Conversion of the pull-off force P_a to the work of adhesion W_{ad} assumes that the tip has a spherical profile of known radius R. If the value of the tip radius is taken to be 5 nm then W_{ad} can be evaluated from equation (4.3) and the graphene surface energy (γ_g) can in turn be estimated using equation (4.2),[8] as;

$$\gamma_g = W_{ad}^2 / 4\gamma_p \tag{4.6}$$

where γ_p is the surface energy of silicon probe, taken to be 55.6 mJm^{-2}.[9] The calculated surface energy in UVA graphene (17.3±2.4 mJm^{-2}) and HPL graphene (16.0±3.1 mJm^{-2}) were 56.6 % and 59.9 % lower than PMMA graphene (39.9±6.7 mJm^{-2}), respectively.

4.2.2 JKR Analysis

Information on the adhesion of soft macroscopic systems (0.1 - 5.0 mm) can be obtained from adhesion tests based on JKR (Johnson, Kendall and Roberts model) analysis.[10-14] Here, the degree of adhesion between a soft polymer sphere and the graphene surface is probed. Again, during compressive loading the radius of the contact spot will be larger than in a simple Hertz case. However, in this case the detailed value depends critically on the work of adhesion, the probe radius R, the surface stiffness K, and the applied compressive force F, as given by:

$$a_{JKR}^3 = \frac{R}{K}\left(F + 3\pi W_{12}R + \sqrt{6\pi W_{12}RF + \left(3\pi W_{12}R\right)^2} \right) \tag{4.7}$$

The indenter used in this study was a PDMS hemisphere of radius 3.51 mm with Young's Modulus, E = 2.6 MPa and Poisson's' Ratio, ν = 0.49. The loading program had a preload of 5 mN, a dwell period of 60 s and a loading/unloading speed of 0.1 µm/s. In a JKR test, the pull-off load is given by the relation:

$$P_a = \frac{3\pi}{2}RW_{ad} \tag{4.8}$$

Since the soft polymer surface is capable of absorbing significant mechanical energy through its visco-elastic behaviour, measured values of W_{ad} are inevitably much greater than W_{12} and are influenced by the speed of the detachment.[15] The custom-built rig used in the study enabled independent measurements to be made of both the contact force and, optically, the contact area.
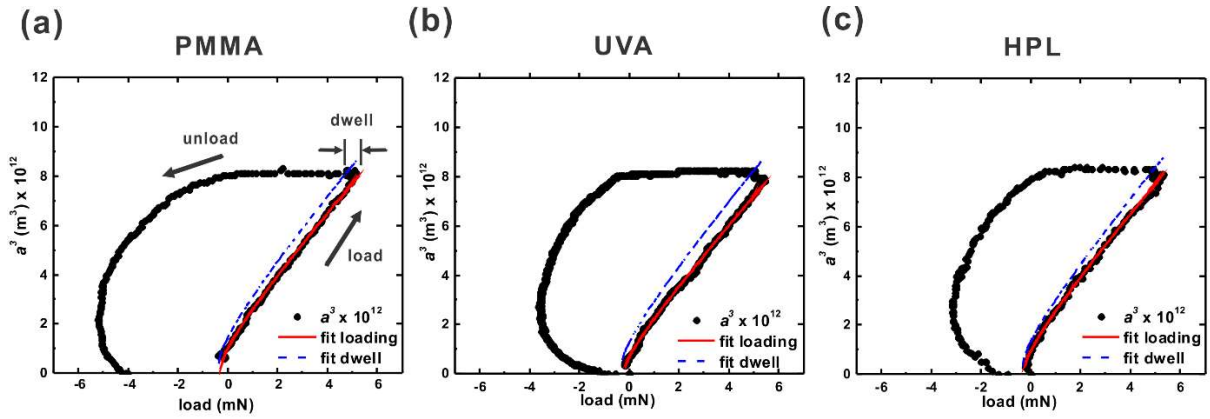
Figure 4.3 JKR load-contact area responses of (a) PMMA-, (b) UVA-, (c) HPL-transferred graphene using PDMS indenter.

Plots of force versus contact spot dimension, plotted as a^3 is shown in **Figure 4.3**. Rearrangement of equation (4.7) provides an expression for W_{ad} in terms of the load P and spot size a, viz

$$W_{ad} = \frac{1}{6\pi a^3}\left(\frac{a^3 K}{R} - P\right)^2 \tag{4.9}$$

By curve fitting equation (4.9) to the loading stage of the test it was possible to find an empirical value of the effective stiffness K and compare this with the value given from

68

independent measurements of the polymer properties E and v. In practice, the layer of adhesive immediately below the graphene introduces an element of compliance into the system so marginally reducing the combined surface stiffness K. Similarly, by fitting equation (4.9) to the observed value of the cube of the contact area radius at the end of the dwell period allowed an estimate to be made of W_{ad} under quasi-steady state conditions. Although the nominal speed of detachment speed was kept constant at 100 nms[-1] during the unloading process the rate at which the radius of the contact spot decreases as it recedes and this is reflected in a significant, and growing, increase in the effective value of W_{ad}. Typically, against the surface examined this grew from around 20 mJm[-2] under steady state conditions to more than 300 mJm[-2] at the point of detachment.[16-18] The estimated W_{ad} showed a higher value (22 mJm[-2]) in PMMA-transferred graphene than in UVA- (21 mJm[-2]) and HPL-transferred graphene (19 mJm[-2]), which is consistent with the surface energy calculation from AFM results.

4.2.3 Contact Angle

The most common technique to assess surface energy γ_S is via contact angle (θ) measurement with two or more standard liquid probes.[19-24] The relationship between the surface energy and θ is given by the Young-Dupré equation.[25]

$$\gamma_S = \gamma_{SL} + \gamma_L \cos\theta \tag{4.10}$$

Here γ_L and γ_S are the surface energies of the liquid and solid, respectively, and γ_{SL} is the surface energy of the solid-liquid interface. On the basis of the Owens-Wendt model,[26] γ_{SL} can be estimated from

$$\gamma_{SL} = \gamma_S + \gamma_L - 2\left(\gamma_S^d \gamma_L^d\right)^{1/2} - 2\left(\gamma_S^p \gamma_L^p\right)^{1/2} \tag{4.11}$$

in which the superscipts d and p refer to the dispersion and polar contributions to surface energy, such that

$$\gamma_S = \gamma_S^d + \gamma_S^p \qquad \text{and} \qquad \gamma_L = \gamma_L^d + \gamma_L^p \qquad\qquad (4.12)$$

Thus, using two liquid probes with known γ_L^d and γ_L^p and two experimental values of θ, we can solve for γ_S^d and γ_S^p, and hence evaluate γ_S. At room temperature and ambient pressure, the surface energies of water and ethylene glycol are 72.8 mJm^{-2} ($\gamma_L^d + \gamma_L^p = 24.7 + 48.1$) and 48.3 mJm^{-2} ($\gamma_L^d + \gamma_L^p = 30.9 + 17.4$), respectively.[27] Contact angles were measured using an optical contact system (CAM200, LOT-Oriel Ltd.), and are shown in **Figure 4.4** (a). The calculated surface energies are shown in **Figure 4.4** (b). The UVA and HPL transfers showed somewhat lower surface energies (26.7±1.2 mJm^{-2} and 32.4±4.2 mJm^{-2}, respectively) compared to the PMMA-transferred graphene (34.4±3.6 mJm^{-2}).
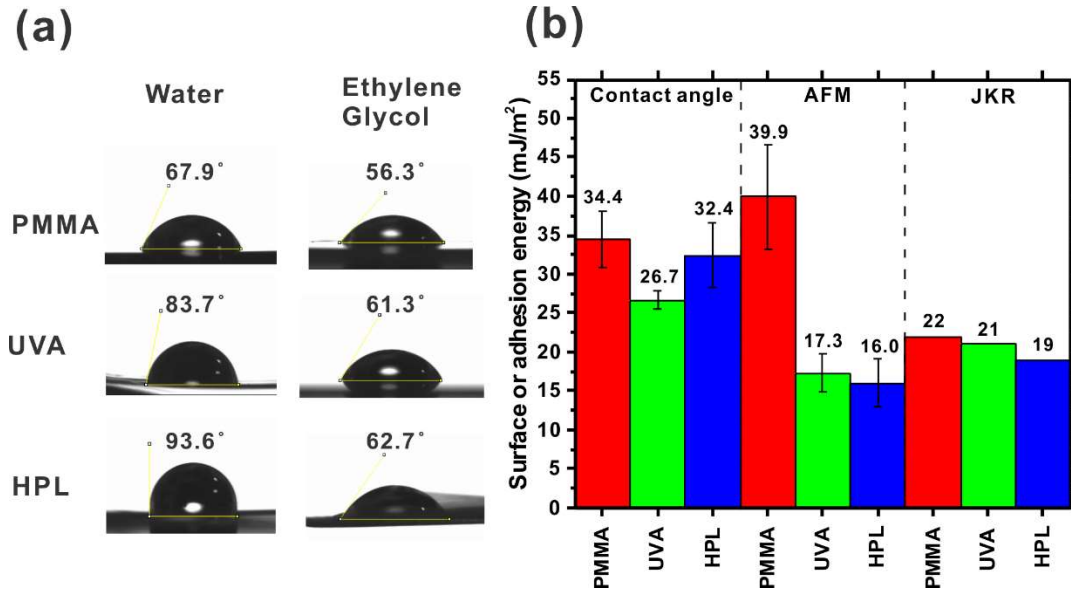
Figure 4.4 (a) Variation in contact angle of graphene as a function of transfer method, and (b) summary of the surface energies and work of adhesion from contact angle, AFM and JKR measurements.

The values of surface energy and work of adhesion of transferred graphene measured by the three methods (Contact angle, AFM, and JKR indentation) are summarised in **Figure 4.4** (b). The work of adhesion is strongly correlated to the morphology of graphene surface and the number of layers as well areal density of lattice defects.[28-32] Defective graphene is

manifestly stickier with a higher surface energy. Lattice vacancies increase the polarity of the surface resulting in an increase in the surface energy and thus a lower bound for the work of adhesion[29, 31-32]. If defect free graphene is perfectly transferred, with no induced defects, the resulting interface will have a very low work of adhesion. Similarly, the more graphene layers that are stacked, the lower the work of adhesion[28, 31]. However, graphene can be easily damaged during conventional transfer processes, which likely creates macroscopic defects[33]. If the substrate is not completely covered, and the transferred material has a significant number of vacancy defects during the selected transfer process, the work of adhesion increases. Though functionally beneficial for sensors and similar applications, should the transferred graphene have a coverage that is less than that defined by percolation theory, then the resulting flexible transparent conductor will be of little use due to its prohibitively high sheet resistance. Should a second and third layer of graphene be transferred, there is a higher probability of covering said lattice vacancies in the first transfer. The higher values of the surface energy and work of adhesion of PMMA-transferred graphene and lower values of UVA- and HPL-transferred graphene suggests, consistent with our Raman map findings, that the areal coverage of graphene is likely higher in the UVA and HPL transfers than for PMMA transfer.

4.3   Mechanical Robustness

To further investigate the degree of adhesion between the graphene and the substrate in each transfer case, T-peel tests were conducted. T-peel tests are a qualitative method primarily intended for determining the relative peel resistance of adhesive bonds between flexible adherents.[34-38] . The T-peel strength is the average load per unit width of a bond line required to separate, progressively, a flexible member from another flexible member. The T-peel test scheme is depicted in **Figure 4.5** (a). The adherents have such dimensions and physical properties so as to permit bending through any angle up to 90° without cracking. Failure follows a path of least resistance which may be cohesive through one element of the structure or interfacial and so along the interface between two elements in the specimen.
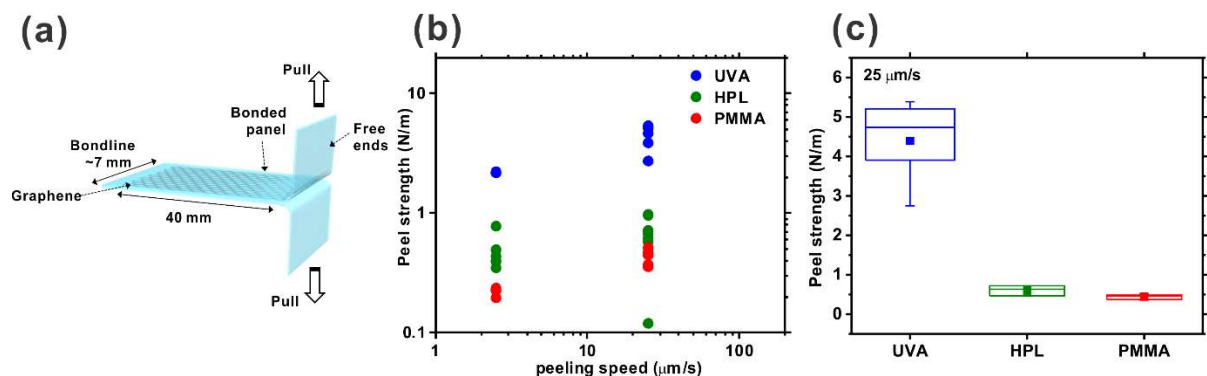
Figure 4.5 (a)T- peel test scheme, (b) Variation in peel strength as a function of peel speed, (c) Distribution in the peel-strength across the considered transfer methods (25 μm/s peeling speed).

In all the specimens, the graphene was sandwiched between two PET sheets and was attached to one of these using the UVA cured adhesive. The bond to the second sheet of PET was formed by either the UVA adhesive, the HPL melt or the natural adhesion between the PMMA transferred graphene. In this case the graphene-PET bond was established by floating the PMMA-graphene sample on water, before transferring this onto the PET and, after drying, removing the PMMA using acetone. Two peeling speeds were evaluated; 2.5 and 25 μm/s. Specimens were of the order of 7 mm wide. **Figure 4.5** (b) shows the variation in peeling strength. A low peel strength represents weak adhesion between the elements of the laminate and substrate, whilst a high peel strength suggests that the graphene is strongly adhered to its substrate. As summarised in **Figure 4.5** (c), the UVA-transferred graphene laminate showed the highest peel strength (4.39±1.09 N/m), followed by the HPL-transferred graphene structure (0.60±0.26 N/m), and the PMMA-transferred graphene structure in which the bond between graphene and PET relied solely on the van der Waals forces showing, as anticipated, the lowest (0.44±0.06 N/m). The substrate adhesion strength of the UVA and HPL graphene are some 880% and 29% higher, respectively, than that of mechanically exfoliated graphene on SiO_2 (0.45±0.02 N/m).[39]

The effective surface energy or work of adhesion provides a measure of the graphene coverage and the degree of defect-induction as a result of the transfer process.[28-32]. Conversely, the magnitude of the peel force per unit width in the T-peel test is a measure directly showing the strength of the bonds between the PET substrate, the adhesive, and the graphene layer. The high bonding strength of the UVA-graphene specimen further demonstrates conclusively that UVA-assistive transfer allows for significantly enhanced adhesion between PET substrates and CVD graphene over the more conventionally used PMMA-based techniques. The strong adhesion between graphene and a substrate plays a major roll in determining the degree of mechanical robustness during bending motion, which is now considered.

4.4   Bending Stability

A bending test is commonly used for evaluating the flexibility of thin films.[40-44] Long-term bending fatigue might induce micro-cracks in the film resulting in increased electrical resistance of the film. By measuring the resistance change during repeated bending, the mechanical robustness of the film can be evaluated.

4.4.1   Bending Angle Variation

To assess the mechanical robustness of the transferred graphene, cyclic bending fatigue tests were conducted using a custom-built, LabVIEW controlled bending stress system. As shown in **Figure 4.6** (a), the system consists of the control (PC / graphical user interface) and the physical rig (bend rig / source-measure unit). The current-voltage (I-V) characteristics of a graphene film loaded on the bend rig was measured and the differential resistance at zero bias, $(dV/dI)_{V=0}$ automatically extracted, following a controlled bend at a defined angle for a defined bend radius (R_b). As shown in **Figure 4.6** (b), the system mechanically clamps both ends of the specimen, where these clamps also serve as electrical probes connected to a Keithley 2600 source-measure unit. The central backside section of the samples was

supported by a changeable cylinder of well-defined bend radius. Ten different bend radii were used.

The robustness of graphene/PET transferred with our three transfer approaches (PMMA, UVA, and HPL) and ITO/PET were assessed with two types of bending tests; bend angle variation and bending fatigue. For the bend angle experiments, a fixed R_b of 2.5 mm was used and the bend angle increased from 0º to 100º, at 10º increments. The measured resistance as a function of bend angle is shown in **Figure 4.7**. The three graphene transfer approaches showed negligible variation in resistance as a function of bend angle (**Figure 4.7 (b)**), whereas the resistance of the ITO increased sharply at bend angles > 40º (**Figure 4.7 (a)**). All graphene samples demonstrated a low normalised resistance even at 100º (1.05 - PMMA, 0.94 – UVA, and 1.04 - HPL), which is around 80 times less than the ITO/PET (79.8). Certainly, the mechanical robustness of transferred graphene is, regardless of the transfer method employed, far superior to that of ITO.
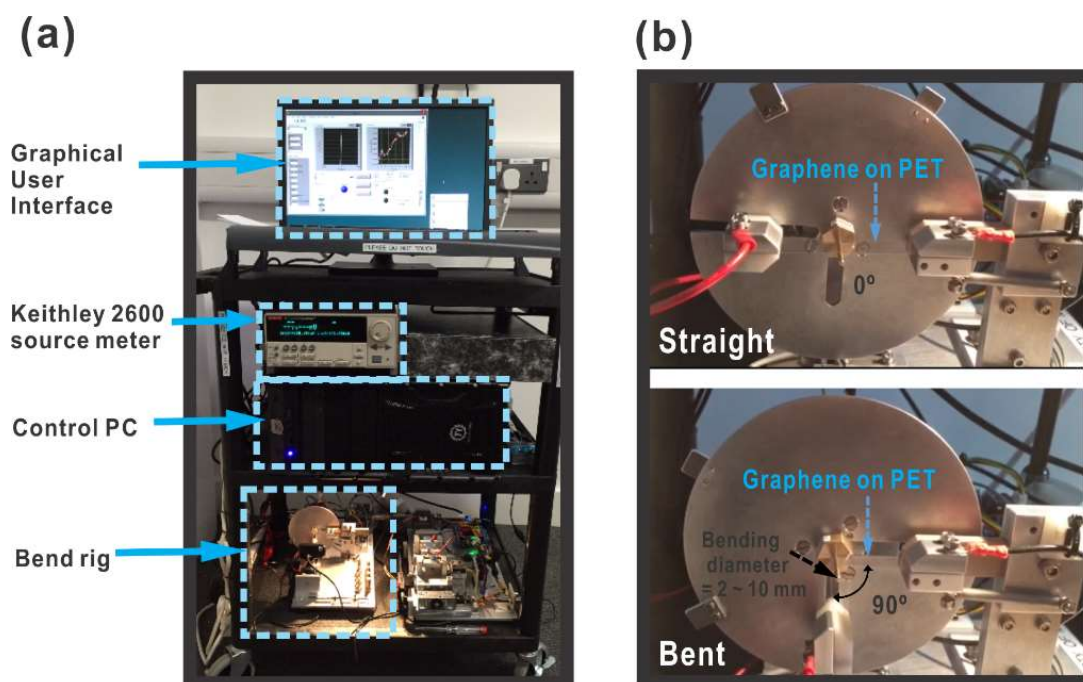
Figure 4.6 (a) A custom-built cyclic bending test system, and (b) photographs of bend rig captured in a bent (90˚) and relaxed state (0˚).
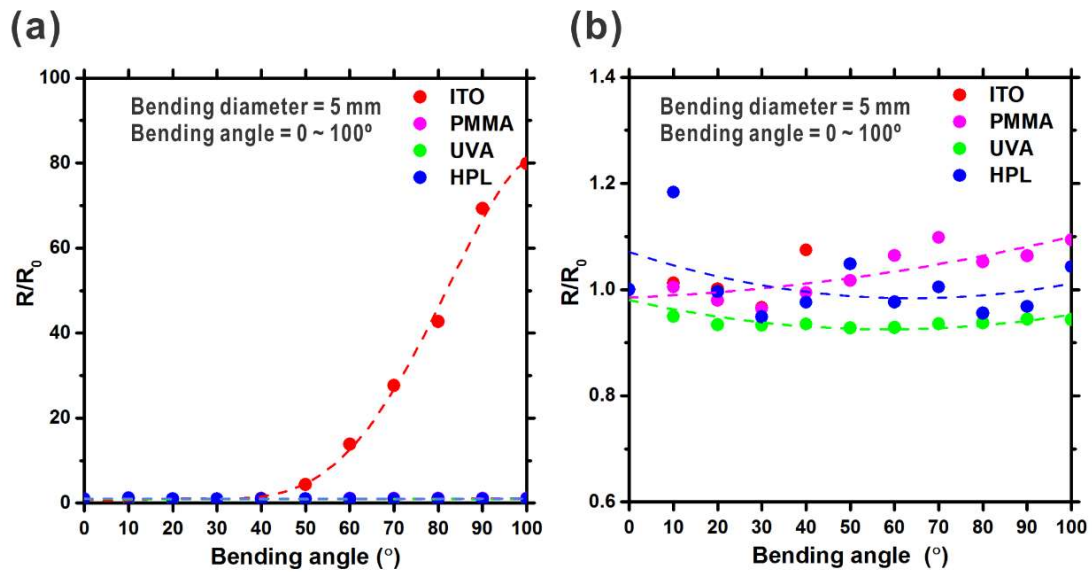
Figure 4.7 Variation in normalised resistance (R/R₀) as a function of bend angle with (a) large Y axis scale and (b) small Y axis scale.

Of the three graphene transfer approaches used we find that, compared to conventional PMMA graphene, UVA graphene exhibits lower resistance throughout all bending angles, with HPL graphene showing a lower resistance at bend angles > 40°. For both the UVA and HPL, the normalised resistance did not tend to increase with bend angle, whilst it did for PMMA graphene. UVA and HPL graphene appear more robust than PMMA graphene for high bend angle applications, such as e-paper and wearable sensors. Bending strain is a known precursor for thin film delamination. If the degree of adhesion is lowered, as a result of the transfer process employed, in many cases this naturally manifests as a limited degree of motion that such devices can accommodate. Indeed, bending readily encourages further delamination of already weakly adhered zones, thereby rapidly degrading, over time and cycle number, the samples mechanical robustness.[33]

4.4.2 Cyclic Bending Fatigue

To assess the bending fatigue of the graphene transfers, graphene and ITO specimens were bent (90°) and relaxed (0°) over 10^4 cycles, and the resistance measured at each bent and

relaxed cycle. **Figure 4.8** (a) shows the measured resistance of ITO and UVA-graphene at 1 mm, R_b, as a function of bending cycles. The resistance of ITO showed a 95-times increase from 2 kΩ to 190 kΩ with a significant difference in resistance between the bent and straight states. However, the graphene showed only a slight increase from 46 kΩ to 74 kΩ across the study with the resistance values in the bent state being compatible ($< \pm 0.5$ kΩ) to the straight state for all cycles.
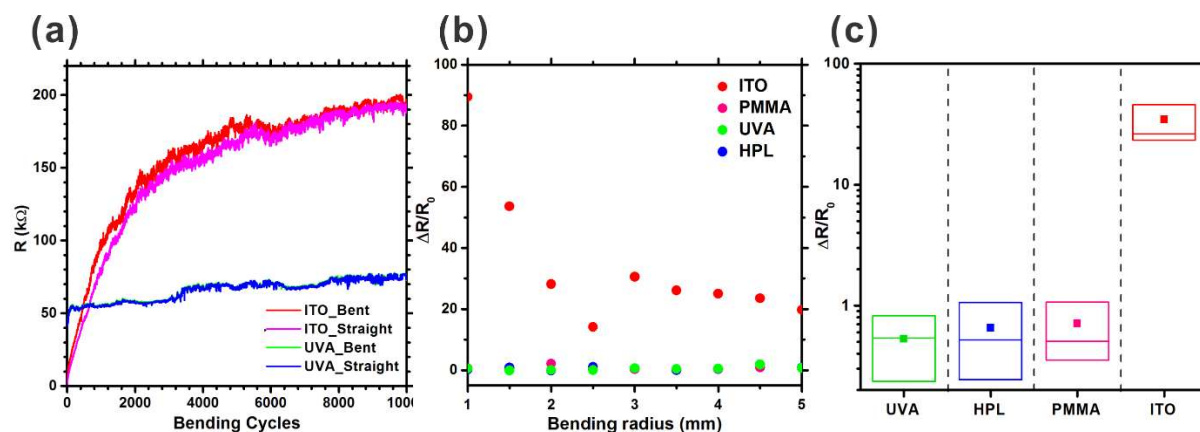
Figure 4.8 (a) Resistance variation of ITO and UVA-graphene as a function of bend cycle, (b) variation of resistance change ($\Delta R/R_0$) as a function of bend radius for ITO and graphene, and (c) mean $\Delta R/R0$ for all bending diameters for graphene transferred by UVA, HPL, and PMMA as well as ITO.

Various bending radii (1 - 5 mm) were considered and the resulting normalised resistance changes ($\Delta R/R_0$) are as shown in **Figure 4.8** (b). The resistance of the ITO increased dramatically after 10^4 cycles ($\Delta R/R_0 \sim 20$ at 5 mm R_b). The resistance of ITO showed a considerable increase at $R_b < 2.5$ mm ($\Delta R/R_0 \sim 14$ at $R_b = 2.5$ mm, $\Delta R/R0 \sim 90$ at $R_b = 1$ mm). Conversely, the $\Delta R/R_0$ values for the graphene specimens were not only much smaller (PMMA: 0.5 - 0.9, UVA: 0.5 - 0.8, and HPL: 0.2 - 1.2) than the ITO, but also showed no visible increasing trend with R_b. The average $\Delta R/R_0$ values of graphene were calculated as; PMMA: 0.80 ± 0.71, UVA: 0.53 ± 0.58, HPL: 0.65 ± 0.82, and ITO: 34.5 ± 22.6, as shown in **Figure 4.8** (c). These results suggest that graphene has superior mechanical robustness compared to ITO and that the transfer method further affects this degree of improvement.

Unlike their bulk counterparts, two-dimensional materials, and particularly those with micro-corrugations, have an extra degree of freedom in the Z-direction allowing for effective lateral stress dissipation. Another possible explanation for the superior robustness of graphene in the present mechanical studies is that the strong covalent bonds within the graphitic lattice accommodate significant strain prior to failure.[45] The average $\Delta R/R_0$ for the UVA and HPL graphene for all bending radii were lower (0.53 and 0.65, respectively) than for the PMMA graphene case (0.80), which is consistent with our earlier bend-angle tests. UVA and HPL graphene do indeed exhibit more robust mechanical properties than the more commonly adopted PMMA transfer, principally attributed to the higher degree of adhesion between the graphene and substrate.

The underpinning mechanisms behind the observed increase in R/R_0 following our fatigue tests was investigated by measuring the surface topology of the bent regions at the specimen centres (for R_b = 4 mm) (Agilent AFM 5500). **Figure 4.9** (a) highlights micro-crack formation, induced by repeated tensile stress, in the ITO/PET. The distance between the cracks was around 18 μm and the crack width was ~40 nm. No such micro-cracks were note in any of the graphene samples (**Figure 4.9** (b)-(d)), with the observed change in R/R_0 in these samples likely attributed to grain movement and to weakened substrate adhesion during repeated bending.
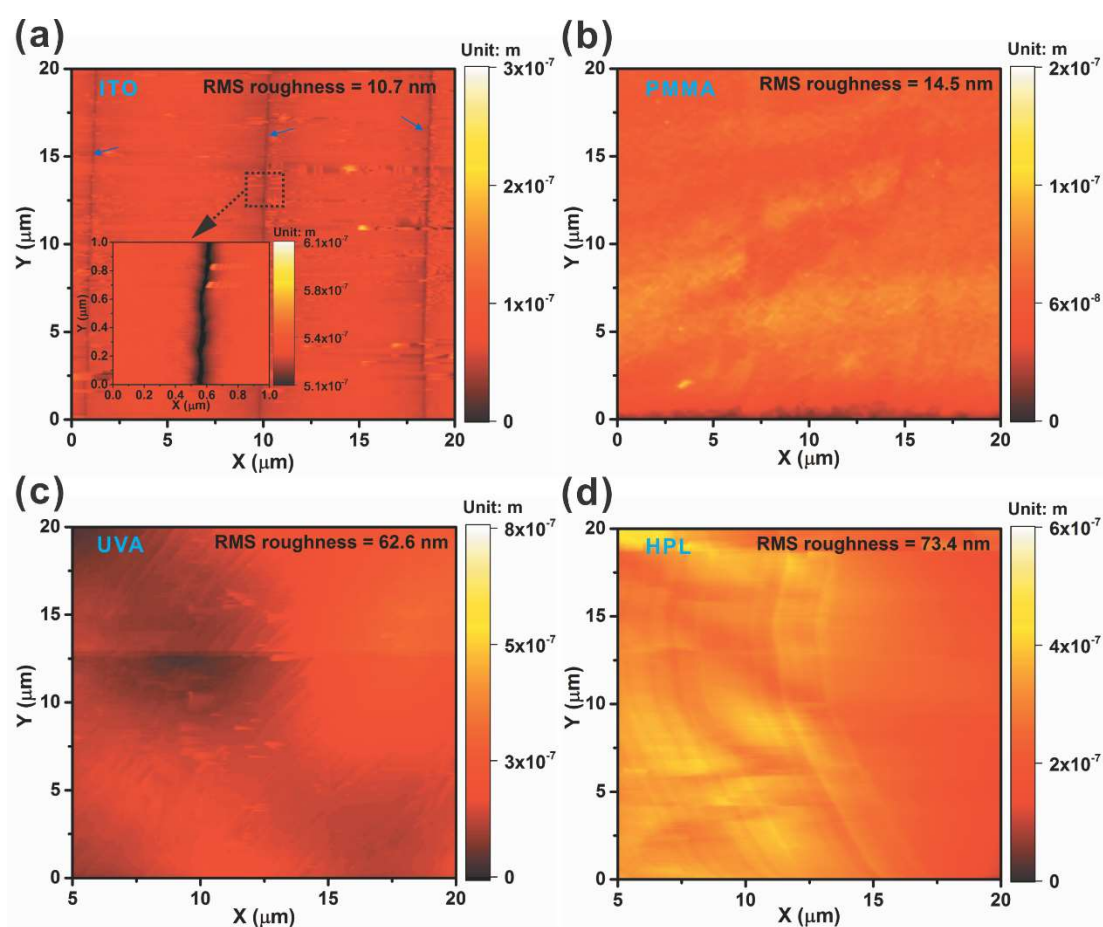
Figure 4.9 AFM maps of (a) ITO, (b) PMMA-transferred graphene, (c) UVA-transferred graphene, and (d) HPL-transferred graphene on PET after 10^4 bending cycles.

Mechanically flexed graphene likely experiences significant defect propagation in the guise of interstitials or vacancy migration which underpin, to a certain extent, microscale intergranular movement, especially if there is compromised or otherwise weakened adhesion to the substrate. In the present geometry and associated stress-concentration mediated therein, such defects likely nucleate further microcracks whose formation and growth are further increased in the presence of reduced interfacial adhesion. Even though repeated bending did not substantially decrease the adhesion between the graphene and its substrate, it nonetheless interacted in the first few mechanical fatiguing cycles resulting in a small and irreversible increase in the resistance due to a defect nucleation phase. Such defect growth was clearly passivated in the strain window considered following these few initial cycles. This is

attributed to the formation of an equilibrated strain distribution following the initial seasoning strain cycles. The transferred graphene is, in this respect, rather different from ITO, which fails to establish such an equilibrium and continues to electrically degrade with further strain cycling. It is probable that percolative networking effects and associated transport play a central role in the graphene systems ability to resist repeated strain cycles compared to ITO.

4.5 Summary

In this chapter, adhesion strategies have been shown to provide strong and long-lasting adhesion between the as-synthesised graphene and the flexible transparent substrates It has been shown that UVA- and HPL-transferred graphene on PET are more stable than PMMA-transferred graphene under bending stress and are more resistant to micro-crack formation than ITO with little variation in normalized resistance for more than 10^4 bend−relax cycles. The superior mechanical robustness will make large-area graphene a compelling platform for the realization of next generation flexible electronics, e-paper, and wearable sensors.

References

1.   Graphene. https://en.wikipedia.org/wiki/Graphene.

2.   Lee, C.; Wei, X.; Kysar, J. W.; Hone, J., Measurement of the Elastic Properties and Intrinsic Strength of Monolayer Graphene. *Science*, **2008,** *321* (5887), 385-388.

3.   Wei, N.; Xu, L.; Wang, H.-Q.; Zheng, J.-C., Strain Engineering of Thermal Conductivity in Graphene Sheets and Nanoribbons: A Demonstration of Magic Flexibility. *Nanotechnology*, **2011,** *22* (10).

4.   Wikipedia, Surface Energy. https://en.wikipedia.org/w/index.php?title=Surface_energy&oldid=708734493.

5.   Packham, D. E., Work of Adhesion: Contact Angles and Contact Mechanics. *INT. J. Adhesion and adhesives*, **1996,** *16*, 121-128.

6.   Bradley, R. S., The Cohesive Force between Solid Surfaces and the Surface Energy of Solids. *Philosophical Magazine*, **1932,** *13* (86), 853-862.

7.   Derjaguin, B. V.; Muller, V. M.; Toporov, Y. P., Effect of Contact Deformations on the Adhesion of Particles. *Journal of Colloid and Interface Science*, **1975,** *53* (2), 314-326.

8.   Medendrop, C. A. Antomic Force Microscopy Method Development for Surface Energy Analysis. Doctoral dissertation, University of Kentucky, 2011.

9.   F. Hejda, P. S., J. Kousal In *Surface Free Energy Determination by Contact Angle Measurements*, WDS 2010, 2010; pp 25-30.

10.   Barthel, E., Adhesive Elastic Contacts: Jkr and More. *Journal of Physics D-Applied Physics*, **2008,** *41* (16).

11.   Lin, Y. Y.; Hui, C. Y.; Baney, J. M., Viscoelastic Contract, Work of Adhesion and the Jkr Technique. *Journal of Physics D: Applied Physics*, **1999,** *32* (17), 2250.

12.   Pocius, A. V.; Dillard, D.; Chaudhury, M., *Adhesion Science and Engineering: Surfaces, Chemistry and Applications*. Elsevier Science: 2002.

13.   Subramanian, K. K. K.; Engineering, I. S. U. M., *Effect of Conformational Change on Nanoscale Friction Behavior of Organic Thin Films*. Iowa State University: 2008.

14.   Cho, J. H.; Lee, D. H.; Lim, J. A.; Cho, K.; Je, J. H.; Yi, J. M., Evaluation of the Adhesion Properties of Inorganic Materials with High Surface Energies. *Langmuir*, **2004,** *20* (23), 10174-10178.

15.   Prieto-López, L. O.; Williams, J. A., Using Microfluidics to Control Soft Adhesion. *Journal of Adhesion Science and Technology*, **2016,** *30* (14), 1555-1573.

16.   de Gennes, P. G.; Brochard-Wyart, F.; Quere, D., *Capillarity and Wetting Phenomena: Drops, Bubbles, Pearls, Waves*. Springer New York: 2003.

17.   Lin, Y.-Y.; Chang, C.-F.; Lee, W.-T., Effects of Thickness on the Largely-Deformed Jkr (Johnson–Kendall–Roberts) Test of Soft Elastic Layers. *International Journal of Solids and Structures*, **2008,** *45* (7–8), 2220-2232.

18.   Charrault, E.; Gauthier, C.; Marie, P.; Schirrer, R., Experimental and Theoretical Analysis of a Dynamic Jkr Contact. *Langmuir,* **2009,** *25* (10), 5847-5854.

19.   Johnson, K. L.; Kendall, K.; Roberts, A. D., Surface Energy and the Contact of Elastic Solids. *Proceedings of the Royal Society of London. A. Mathematical and Physical Sciences*, **1971,** *324* (1558), 301-313.

20.   Owens, D. K.; Wendt, R. C., Estimation of the Surface Free Energy of Polymers. *Journal of Applied Polymer Science*, **1969,** *13* (8), 1741-1747.

21.   Rotenberg, Y.; Boruvka, L.; Neumann, A. W., Determination of Surface Tension and Contact Angle from the Shapes of Axisymmetric Fluid Interfaces. *Journal of Colloid and Interface Science*, **1983,** *93* (1), 169-183.

22.   Cassie, A. B. D.; Baxter, S., Wettability of Porous Surfaces. *Transactions of the Faraday Society*, **1944,** *40* (0), 546-551.

23.   Janssen, D.; De Palma, R.; Verlaak, S.; Heremans, P.; Dehaen, W., Static Solvent Contact Angle Measurements, Surface Free Energy and Wettability Determination of Various Self-Assembled Monolayers on Silicon Dioxide. *Thin Solid Films,* **2006,** *515* (4), 1433-1438.

24.   Wang, S.; Zhang, Y.; Abidi, N.; Cabrales, L., Wettability and Surface Free Energy of Graphene Films. *Langmuir,* **2009,** *25* (18), 11078-11081.

25.   Nakamura, Y.; Kamada, K.; Katoh, Y.; Watanabe, A., Studies on Secondary Electrocapillary Effects: 1. Confirmation of Young-Dupre Equation. *Journal of Colloid and Interface Science*, **1973,** *44* (3), 517-524.

26.   Owens, D. K.; Wendt, R. C., Estimation of Surface Free Eenergy of Polymers. *Journal of Applied Polymer Science*, **1969,** *13* (8), 1741-&.

27.   Moutinho, I.; Figueiredo, M.; Ferreira, P., Evaluating the Surface Energy of Laboratory-Made Paper Sheets by Contact Angle Measurements. *Tappi Journal*, **2007,** *6* (6), 26-32.

28.   Pourzand, H.; Tabib-Azar, M., Graphene Thickness Dependent Adhesion Force and Its Correlation to Surface Roughness. *Applied Physics Letters*, **2014,** *104* (17), 171603.

29.   Shin, Y. J.; Wang, Y.; Huang, H.; Kalon, G.; Wee, A. T.; Shen, Z.; Bhatia, C. S.; Yang, H., Surface-Energy Engineering of Graphene. *Langmuir,* **2010,** *26* (6), 3798-802.

30.   Gao, W.; Huang, R., Effect of Surface Roughness on Adhesion of Graphene Membranes. *Journal of Physics D: Applied Physics*, **2011,** *44* (45), 452001.

31.   Rafiee, J.; Mi, X.; Gullapalli, H.; Thomas, A. V.; Yavari, F.; Shi, Y.; Ajayan, P. M.; Koratkar, N. A., Wetting Transparency of Graphene. *Nature Materials*, **2012,** *11* (3), 217-22.

32.   Raj, R.; Maroo, S. C.; Wang, E. N., Wettability of Graphene. *Nano Letters*, **2013,** *13* (4), 1509-15.

33.   Lee, S.-M.; Kim, J.-H.; Ahn, J.-H., Graphene as a Flexible Electronic Material: Mechanical Limitations by Defect Formation and Efforts to Overcome. *Materials Today,* **2015,** *18* (6), 336-344.

34.   Lin, T. K.; Wu, S. J.; Lai, J. G.; Shyu, S. S., The Effect of Chemical Treatment on Reinforcement/Matrix Interaction in Kevlar-Fiber/Bismaleimide Composites. *Composites Science and Technology,* **2000,** *60* (9), 1873-1878.

35.   Kurzweg, H.; Heimann, R. B.; Troczynski, T., Adhesion of Thermally Sprayed Hydroxyapatite–Bond-Coat Systems Measured by a Novel Peel Test. *Journal of Materials Science: Materials in Medicine,* **1998,** *9* (1), 9-16.

36.   Hadavinia, H.; Kawashita, L.; Kinloch, A. J.; Moore, D. R.; Williams, J. G., A Numerical Analysis of the Elastic-Plastic Peel Test. *Engineering Fracture Mechanics,* **2006,** *73* (16), 2324-2335.

37.   Song, J. Y.; Yu, J., Analysis of the T-Peel Strength in a Cu/Cr/Polyimide System. *Acta Materialia,* **2002,** *50* (16), 3985-3994.

38.   Lacombe, R., Applied Adhesion Testing. In *Adhesion Measurement Methods*, CRC Press: 2005; pp 187-248.

39.   Koenig, S. P.; Boddeti, N. G.; Dunn, M. L.; Bunch, J. S., Ultrastrong Adhesion of Graphene Membranes. *Nature Nanotechnology,* **2011,** *6* (9), 543-546.

40.   Cocurullo, A.; Airey, G. D.; Collop, A. C.; Sangiorgi, C., Indirect Tensile Versus Two-Point Bending Fatigue Testing. *Proceedings of the Institution of Civil Engineers - Transport,* **2008,** *161* (4), 207-220.

41.   Zhou, Z. R.; Goudreau, S.; Fiset, M.; Cardou, A., Single Wire Fretting Fatigue Tests for Electrical Conductor Bending Fatigue Evaluation. *Wear,* **1995,** *181*, 537-543.

42.   Liu, Q.; Schlangen, E.; van de Ven, M.; van Bochove, G.; van Montfort, J., Evaluation of the Induction Healing Effect of Porous Asphalt Concrete through Four Point Bending Fatigue Test. *Construction and Building Materials,* **2012,** *29*, 403-409.

43.   Auch, M. D. J.; Soo, O. K.; Ewald, G.; Soo-Jin, C., Ultrathin Glass for Flexible Oled Application. *Thin Solid Films,* **2002,** *417* (1–2), 47-50.

44.   Na, S.-I.; Kim, S.-S.; Jo, J.; Kim, D.-Y., Efficient and Flexible Ito-Free Organic Solar Cells Using Highly Conductive Polymer Anodes. *Advanced Materials,* **2008,** *20* (21), 4061-4067.

45.   C. Galiotis, G. T., O. Frank, J. Parthenios, K. Papagelis, K. S. Novoselov Mechanical Properties of Graphenes and Graphene Polymer Nanocomposites. In *Eur. Conf. Com. Mater.*, Venice, Italy, 2012.

Chapter 5 Chemical Doping

5.1 Introduction

Graphene has been considered as an alternative for ITO or FTO on account of its high charge mobility, high optical transmittance,[1-3] alongside its impressive mechanical robustness, as confirmed through the authors' experimental results presented earlier in this thesis. The flexibility of graphene makes it well-suited for a number of emerging optoelectronics applications, such as e-paper, flexible displays and user-conformal wearables [1, 4-6]. To date there have been many attempts to utilize graphene as a transparent flexible conductor in organic light emitting diodes (OLED)[5, 7-12], touch screens[13-15] and photovoltaic cells[16-19]. Common to all such opto-electronic applications is the need for a reduction in the graphene's R_S whilst maintaining its high optical transparency. As discussed in Chapter 2, the E_F of pristine graphene lies at the Dirac point, where there is a significantly reduced, and theoretically null density of states. Due to this low density of states, the R_S of monolayer pristine graphene is fundamentally limited to ~1 kΩ/sq.[20-22] which is too high for it to function as a suitable replacement for metal and transparent conducting oxide electrodes in the majority of applications[1, 23]; touch screens require R_S <500 Ω/sq., whilst graphical displays require R_S <100 Ω/sq, both with transparencies of > 90%.[24]

One approach to reduce R_S is to make hybrid layer structures coupling graphene and nanowires,[25-30] as discussed earlier. To test this I have investigated the optical luminance of an OLED cell through the use of a hybrid anode consisting of silver nanowires and UVA-transferred graphene on PET substrates. Another approach to decrease the R_S of graphene is by selective doping. In several early reports, chemical doping has been shown to decrease R_S of graphene from ~1 k Ω/sq. to ~90 Ω/sq. without significantly compromising the optical

transparency (~80%).[31-37]   In this thesis, to decrease the R_S of CVD graphene, chemical doping has been adopted using various metal chlorides (gold chloride ($AuCl_3$), ferric chloride ($FeCl_3$), tin chloride ($SnCl_2$), iridium chloride ($IrCl_3$) and rhodium chloride ($RhCl_3$)). The optical and electrical properties of doped graphene will be presented and the temporal stability of the properties in ambient condition analysed.

5.1   A PET-supported Graphene / Silver Nanowire based OLED

To decrease the R_S of CVD graphene for use in OLEDs, commercial silver nanowire (AgNW) (0.5 wt.% in isopropyl alcohol, Sigma Aldrich, Co. Ltd) were spin coated on our previously discussed graphene. The AgNWs were 40 - 60 nm diameter and 5 - 20 µm long.
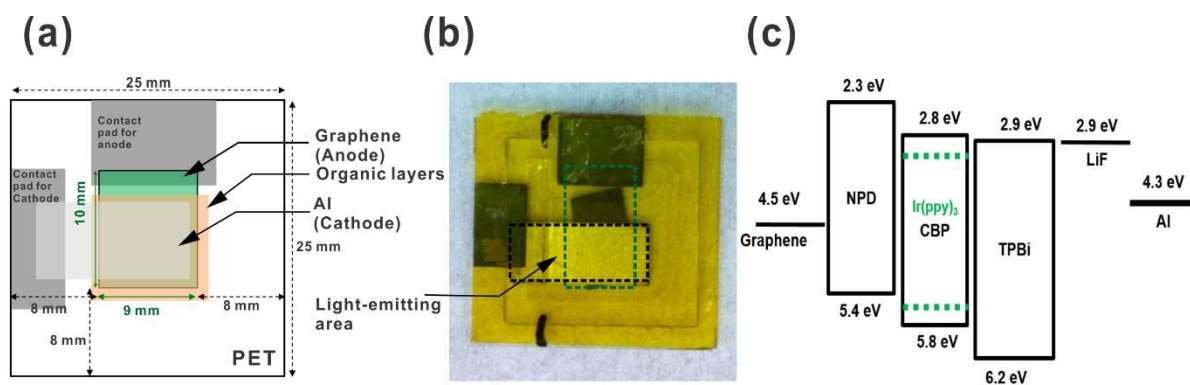
Figure 5.1 (a) Schematic OLED cell. (b) Photograph of a typical fabricated OLED test cell using the reported hybrid graphene anode. (c) Energy level diagram of all layers used in the OLED.

To fabricate the OLED, monolayer graphene was synthesised by CVD using the same growth conditions as described in Chapter 3 and transferred onto PET substrates using the as-above-reported UVA-transfer process. **Figure 5.1** (a) and (b) illustrate a schematic of the OLED structure and a photograph of one of the OLED test cells fabricated using the UVA-transferred CVD graphene, respectively. The graphene area covering the PET substrate (25

mm x 25 mm) was 90 mm^2. After graphene transfer, AgNWs were spin-coated onto the graphene at 700 rpm for 25 s followed by a hot plate anneal at 100 °C for 5 min. The AgNW coated on the cathode contact pad was removed using isopropyl alcohol to prevent unintentional short circuiting between the anode and cathode. The organic layers; NPD (hole transport layer), CBP-Ir(ppy)$_3$ (emission layer),TPBi (electron transport layer), LiF (electron injection layer), and aluminium cathode were then sequentially deposited using a standard thermal evaporator by Hyomin Kim at Kyung Hee University. The energy levels of the stacked organic layers are gradually aligned to ensure rapid carrier diffusion though the OLED cell, as shown in **Figure 5.1** (c).
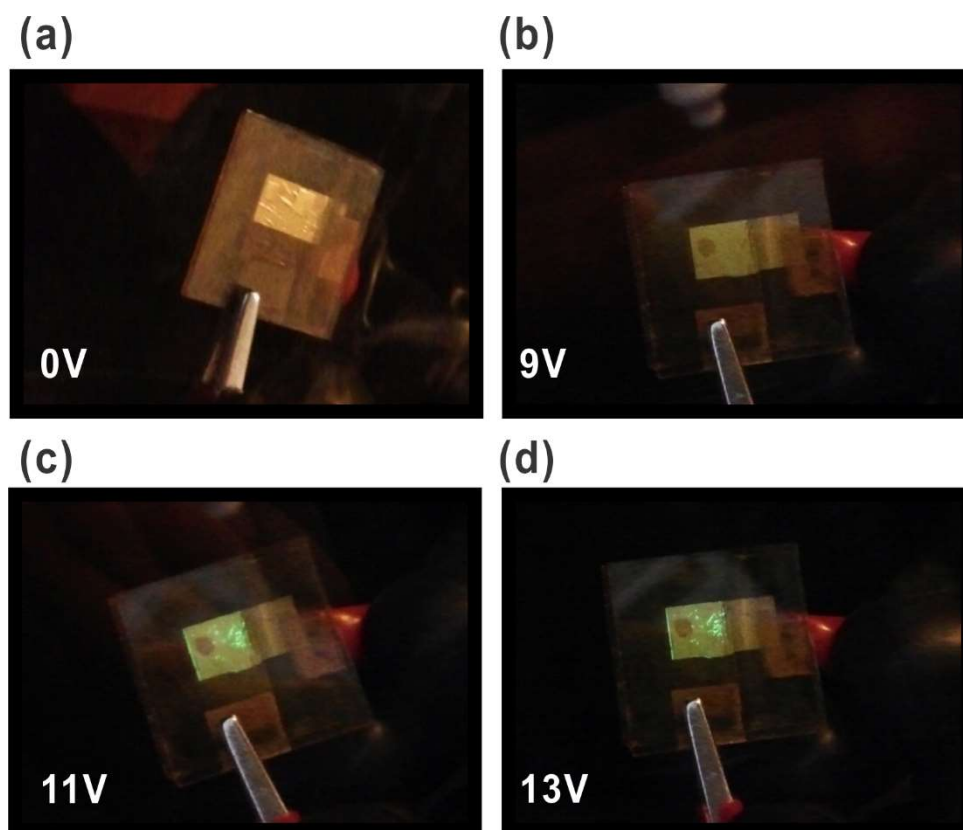
Figure 5.2 Photos of a fabricated OLED test cell using hybrid anode of graphene and AgNW captured at four different voltages; (a)0V, (b) 9V, (c) 11V, and (d) 13V).

The R_S of the AgNW-coated graphene measured by four-point probe (Jandel Co. Ltd) varied from 41 Ω/sq. to 81 Ω/sq. with a mean value 57 Ω/sq. and standard deviation 14 Ω/sq. It is presumed that AgNW assists in charge transport across the graphene grains and defects so that the macroscale R_S decreases. The captured photographs show the resulting light emission from the fabricated OLED using an AgNW-coated graphene anode on PET (**Figure 5.2**). The OLED turned on at around 9 V, with the light becoming brighter as the voltage increased. However, devices had notably poor uniformity. It is assumed that the bright spots were caused by the non-uniformly aggregated AgNWs or from areas where the AgNWs were not sufficiently planarized. There were also large dark zones, likely created by short-circuits due to NW protrusions when applying voltages > 9V, which we attribute to the sharp apex of the AgNWs. Applying 13 V, the OLED did not show any change in light brightness and a few seconds later it broke down (**Figure 5.2** (d)). The failure is considered to be caused by an electrical short associated with the AgNWs.
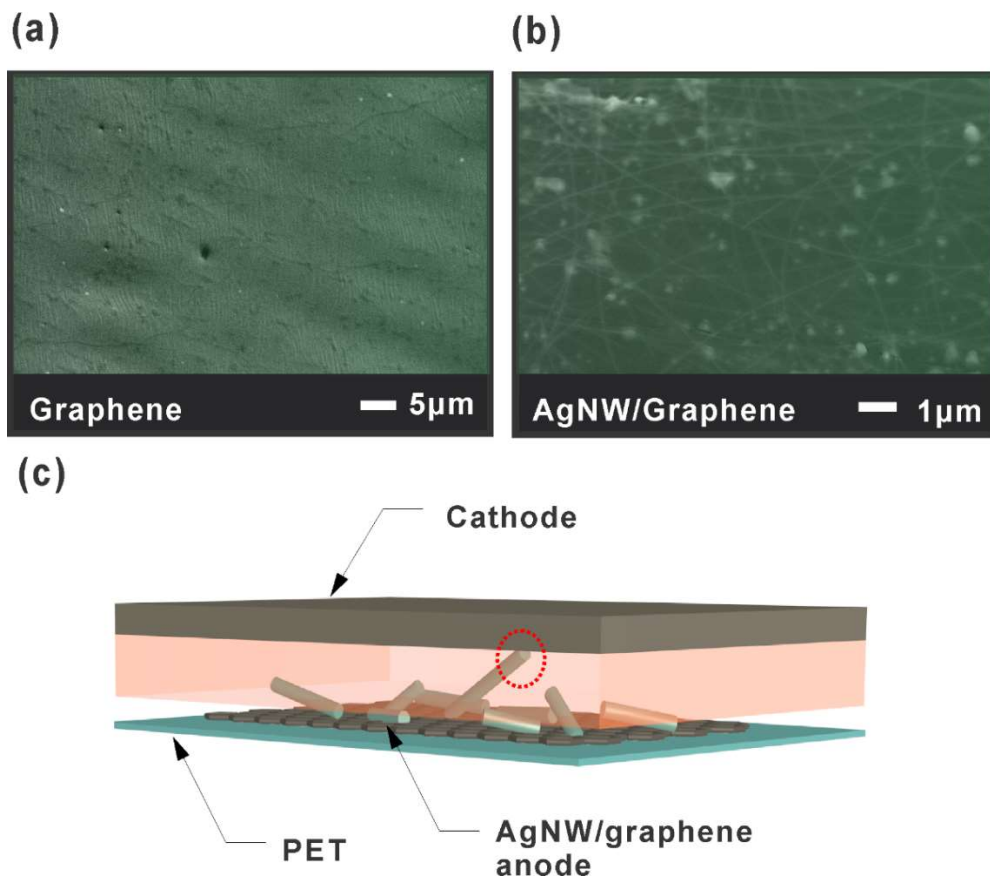
Figure 5.3 (False coloured) SEM micrographs of: (a) Graphene and (b) AgNW-coated graphene on PET. (c) Schematic of cross-sectional OLED structure.

As shown in the SEM image in **Figure 5.3** (b), the AgNWs coverage was non-uniform which may well have resulted in equally non-uniform light emission. Some of the non-planarized NWs are likely occasionally tilted upwards therein deriving links between the anode and the electron injection layer, or directly to the cathode, as illustrated in the schematic (**Figure 5.3** (c)), compromising OLED performance. Such issues remain outstanding.

Though the electrical conductivity was successfully enhanced using the developed hybrid graphene/NW electrode, significant areal non-uniformities occurred. As a result, other approaches were deemed more suitable to decrease R_S. One such approach was to modify the work function or carrier concentration in graphene via chemical doping.

5.2 Chemical Doping with Metal Chlorides

Chemical doping strategies allow for the tuning of the work function and carrier concentration of thin films without compromising their as-synthesised optical transparency. As a result such methodologies have been considered one of the most viable means of decreasing R_S[31-37]. In the present study chemical doping was adopted based on established chlorine compounds that have been investigated elsewhere in other nanocarbon systems[33, 36, 38-40].

Following CVD synthesis (**Figure 5.4** (b)) and UVA-transfer (**Figure 5.4** (c)) on a 20 mm x 20 mm PET substrate, graphene was chemically doped with one of five chloride compounds ($AuCl_3$, $FeCl_3$, $SnCl_2$, $IrCl_3$, or $RhCl_3$) to enhance its conductivity as depicted in **Figure 5.4** (a). Each compound is soluble in specific solvents and thus was dissolved in different solvents employed from previous reports[38, 41] ($AuCl_3$ and $IrCl_3$ / acetonitrile, $FeCl_3$ and $SnCl_2$ / DI water, and $RhCl_3$ / methanol) each at 20 mM concentration. The dopant solutions were spin-coated onto the transferred graphene samples at 2000 rpm for 1 min. Typical photographs of the chemically doped graphene sheets are shown in **Figure 5.4** (d) – (h).
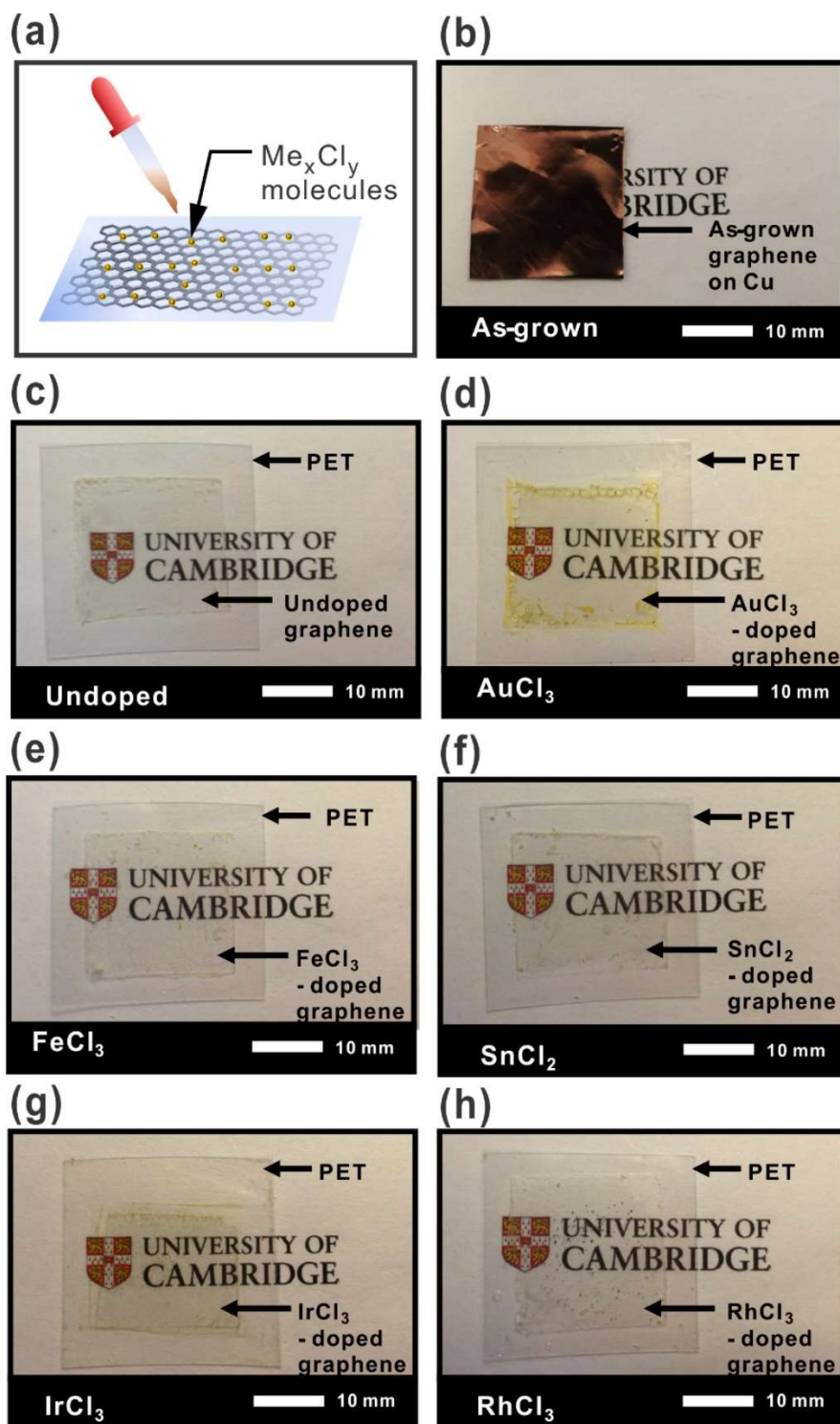
Figure 5.4 (a) The metal chloride chemical doping process. Photographs of (b) CVD-grown graphene on Cu foil, (c) UVA-transferred graphene onto PET (undoped), (d) AuCl3-, (e) FeCl3-, (f) SnCl2-, (g) IrCl3-, and (h) RhCl3-doped graphene on PET.

89

To assess the implications of the metal chloride (Me_xCl_y)doping, it is necessary to decouple any shifts in R_S and %T due to the solvent from those of the Me_xCl_y solute. **Figure 5.5** summarises the solvent and concentration controls. In the solvent controls three high-purity solvents (DI water, methanol, and acetonitrile), commensurate with those used in the doping studies, were spin-coated onto the graphene using the same casting recipe as those used for the Me_xCl_y doping and optical transmittance (%T) and sheet resistance (R_S) measured, reported later.

As shown in **Figure 5.5** (a) and (b), there was no significant change in %T at 550 nm wavelength ($\Delta\%T_{550nm}$ = +0.75%, +0.7%, and +0.11%) for samples treated with DI water, methanol and acetonitrile, respectively. Similarly, there was no significant change in R_S (ΔR_S = +0.01 kΩ/sq., -0.03 kΩ/sq.) for samples treated with DI water, and methanol, respectively.

However, samples treated with acetonitrile showed a non-negligible increase in R_S (+0.25 kΩ/sq.). Acetonitrile seemed to marginally degrade R_S. In the present study $AuCl_3$ was dissolved in acetonitrile but interestingly, $AuCl_3$ samples showed the largest decrease in R_S, even though the doping effects of acetonitrile evidently tended to increase R_S. One strategy to further improve the doping effects of $AuCl_3$ would be to use alternative solvents.

Nevertheless, **Figure 5.5** (a) and (b) broadly revealed that the impact of the solvent is largely negligible and suggest that the observed variations in R_S and %T, upon Me_xCl_y doping, are not attributed to the solvent but rather the solute. **Figure 5.5** (c) and (d) show the %T and R_S of the doped graphene as a function of various concentrations of $AuCl_3$. As the dopant concentration increased, the doped graphene showed lower %T and lower R_S. The %T decreases ($\Delta\%T$) were marginal from doped graphene at 20 mM (1.49%) and 30 mM (6.78%). However, the %T was substantially decreased ($\Delta\%T$ = 10.39%) at 40 mM. Unlike the considerable change in %T, R_S was not greatly affected by concentration (2.18 kΩ/sq., 1.94 kΩ/sq., and 2.13 kΩ/sq. at 20mM, 30 mM and 40 mM, respectively).
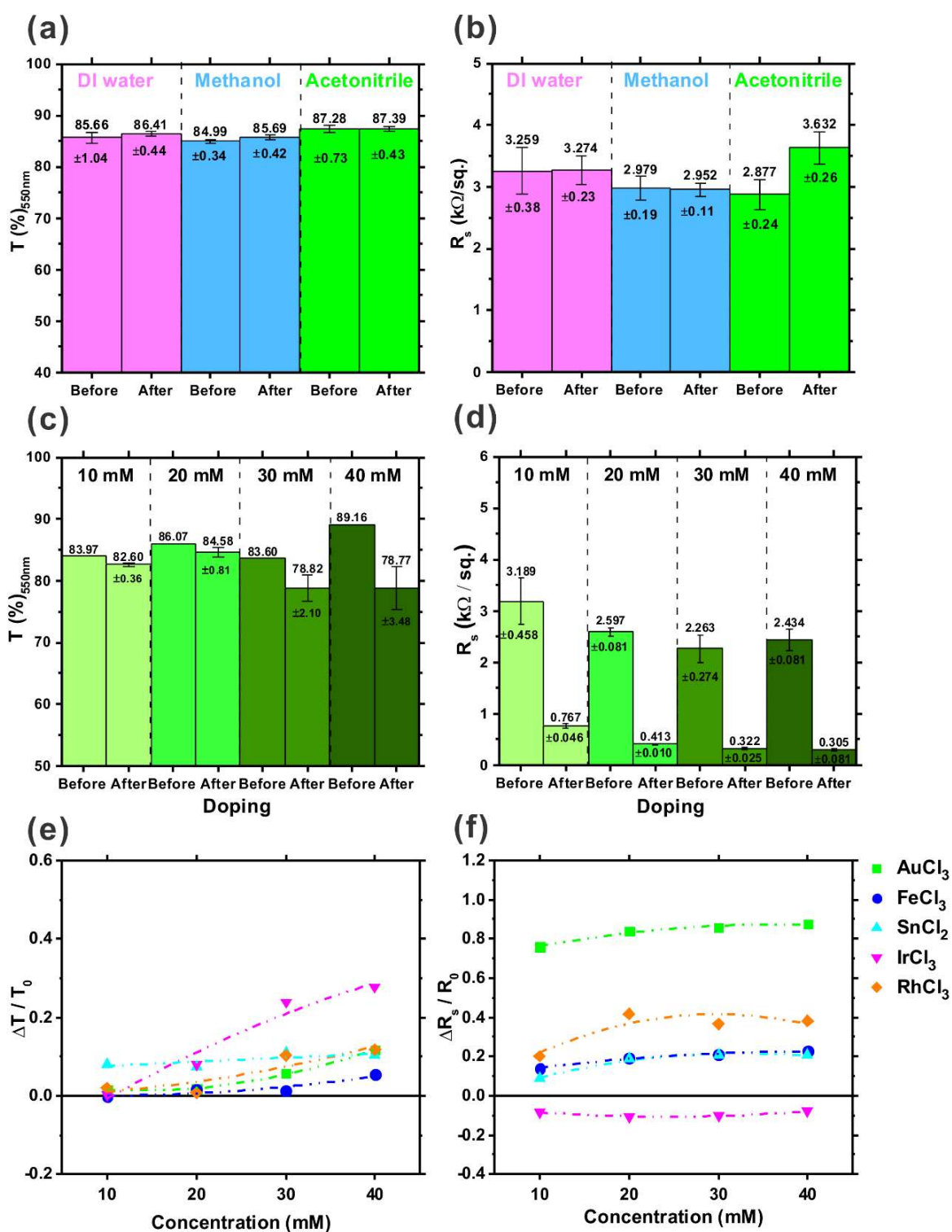
Figure 5.5 Solvent controls: (a %T$_{550\,nm}$ and (b) R$_S$ of graphene on PET following solvent treatment (without dopant). (c) %T$_{550\,nm}$ and (d) R$_S$ of AuCl$_3$-doped graphene for various molar concentrations. (e)

Normalised %T change and (f) R_S change of graphene doped for all Me_xCl_y as a function of molar concentrations.

The normalised Δ%T and ΔR_S of doped graphene on PET with the various dopant solutions, as shown in **Figure 5.5** (e) and (f), suggest that R_S is not directly proportional to dopant concentration, whilst the %T decreases consistently with increasing concentration. This indicates that dopant molecules may be adsorbed on the graphene surface resulting in a %T decrease, but charge transfer from the dopant molecules evidently saturates at concentrations > 20 mM. The reduction in R_S depends on the electronegativity of the metal ions in the dopants[42-43]. As shown in **Figure 5.5** (f), the largest reduction in R_S ($\Delta R_S/R_0 = 0.84$) was observed from the $AuCl_3$-doped which has the highest electronegativity (2.54) among the dopants ($FeCl_3$: 1.83, $SnCl_2$: 1.96, $IrCl_3$: 2.2, and $RhCl_3$: 2.28).[44]

Figure 5.6 (a) shows the %T spectra of undoped and doped graphenes over a range of wavelengths (350 - 950 nm, ATI, Unicam UV2) using various Me_xCl_y dopants. **Figure 5.6** (b) - (g) show the spatial variation in the %T of undoped and doped graphene at 550 nm. Full spectra were acquired at each measured position. The %T_{550} of the undoped graphene was 84.1%, some 5.2% lower than that of the bare PET (89.3%), suggesting that the graphene is largely monolayer with the 5 μm-thick UV-adhesive layer likely to have contributed to the extra optical absorption. The standard deviation in the spatially resolved %T of the undoped graphene on PET suggests that transfer method led to an areal uniformity of approximately 2.9 % resulting in an optical absorption ranging from 2.3 % to 8.1 % across the sample (20 mm x 20 mm). After chemical doping the areal mean %T_{550} decreased by 7.0 % ($RhCl_3$-doped), 19.2% ($IrCl_3$-doped) 7.1 % ($AuCl_3$), 7.5%, ($FeCl_3$) and 10.3% ($SnCl_2$). **Figure 5.8** (a) summarises the average values of %T for all the doped graphenes.

Figure 5.7 (a) - (f) show the spatially resolved R_S (Jandel Four -Point Probe) of the undoped and doped graphene. The UVA-transferred graphene showed a R_S of 3.5 ± 0.2 kΩ/sq before chemical doping. By way of a control, to compare the R_S of the UVA-transferred graphene to that of conventional PMMA-transfer we assessed the conductivity of as-grown graphene

independently by transferring it to quartz substrates. The transferred graphene showed a sheet resistance of 5.5 ± 1.2 kΩ/sq., which is some 64% higher than that of UVA transferred graphene. Clearly the transfer method plays a critical role in optimising R_S.
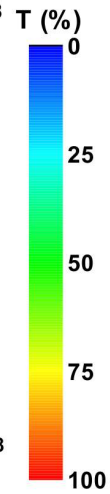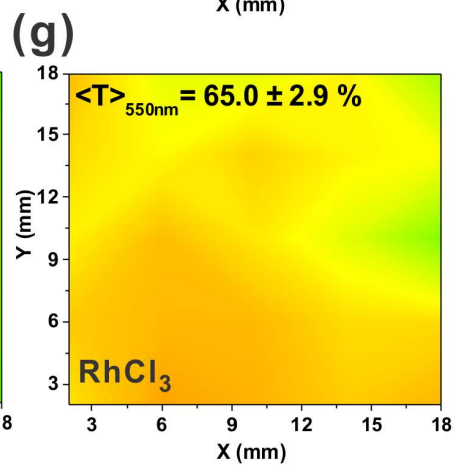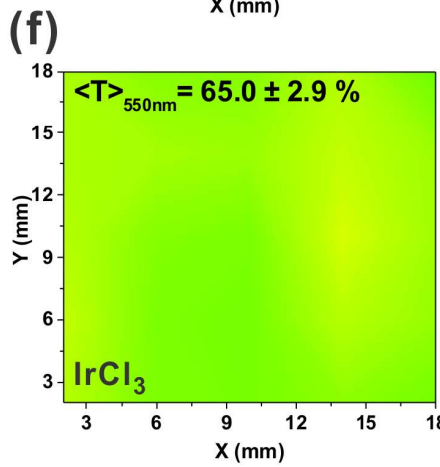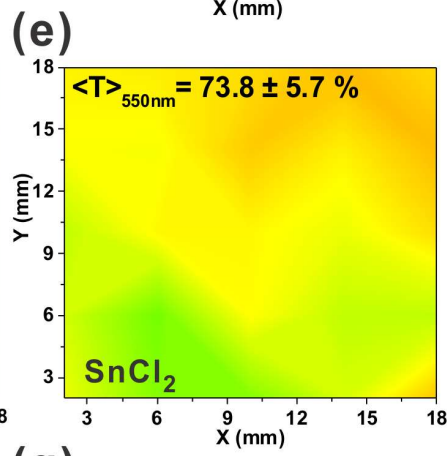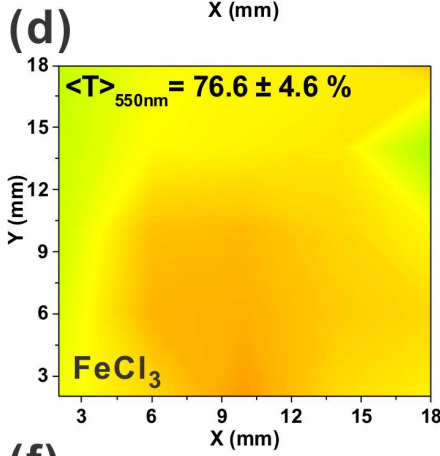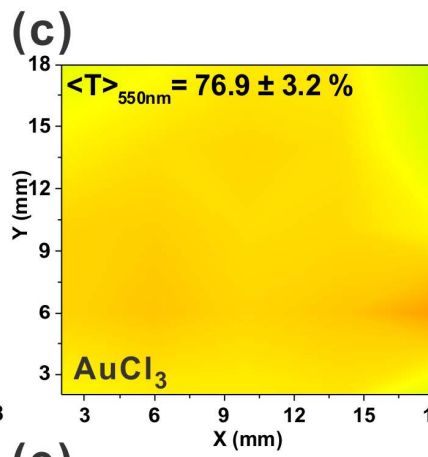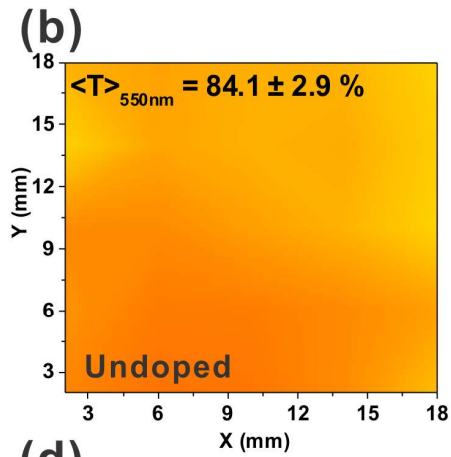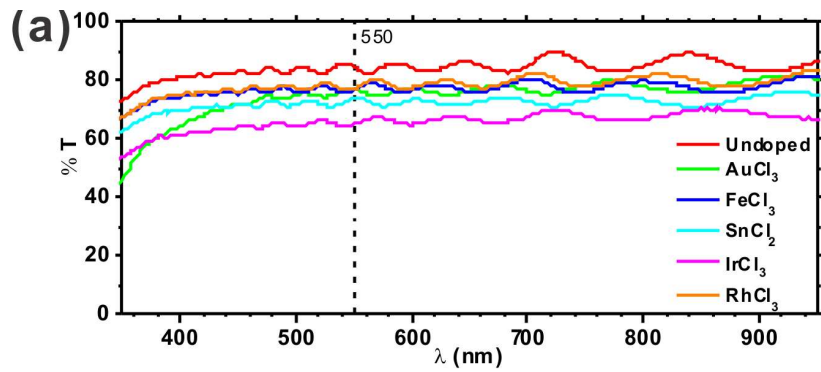
Figure 5.6 (a) Typical optical transmittance spectra of undoped and doped graphenes and optical transmittance maps (550 nm) of (b) undoped, (c) AuCl₃-, (d) FeCl₃-, (e) SnCl₂-, (f) IrCl₃-, (g) RhCl₃-doped graphene.
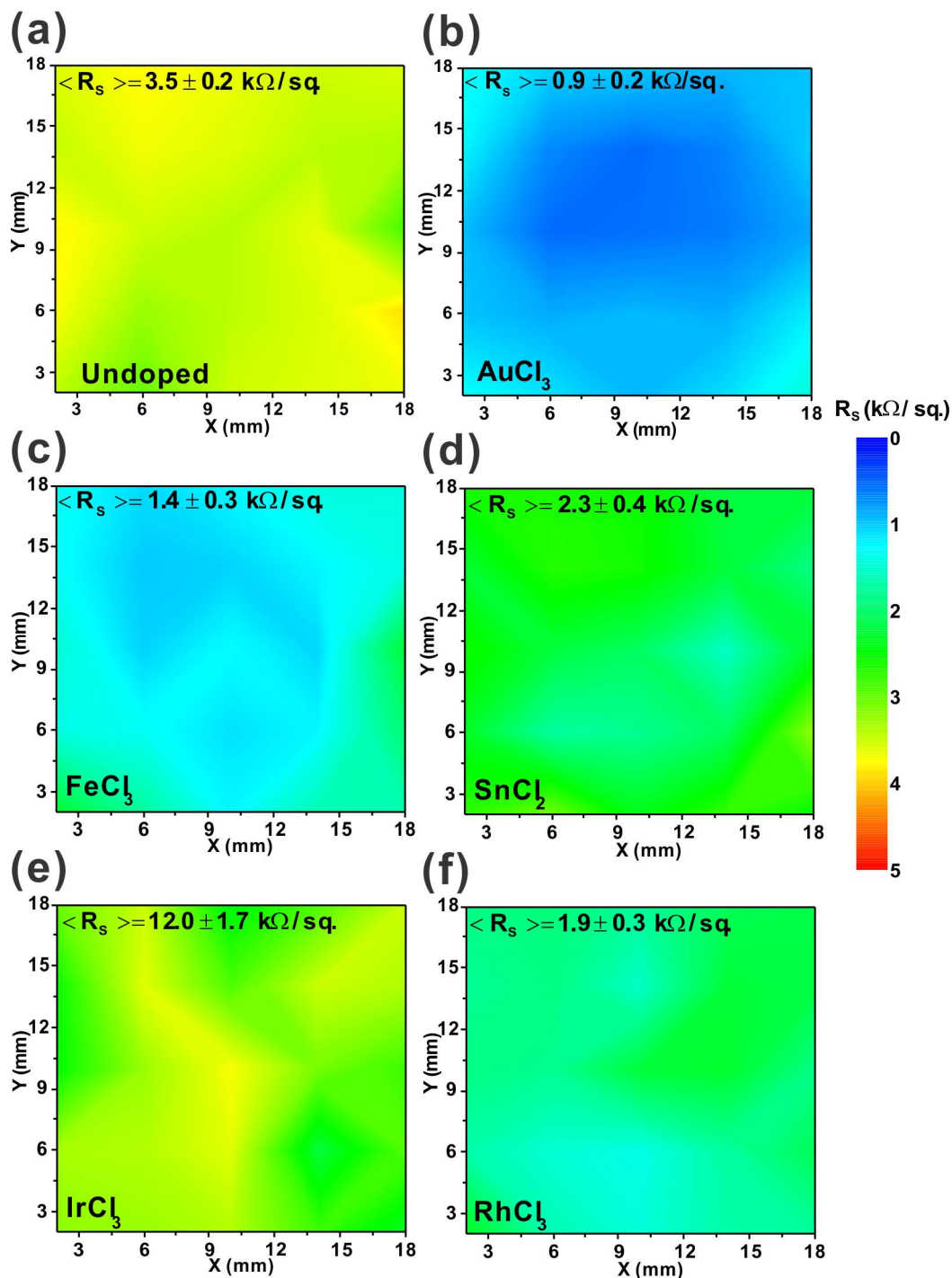
Figure 5.7 Sheet resistance maps of (a) undoped graphene and (b) AuCl₃-, (c) FeCl₃-, (d) SnCl₂-, (e) IrCl₃-, and (f) RhCl₃-doped graphene.
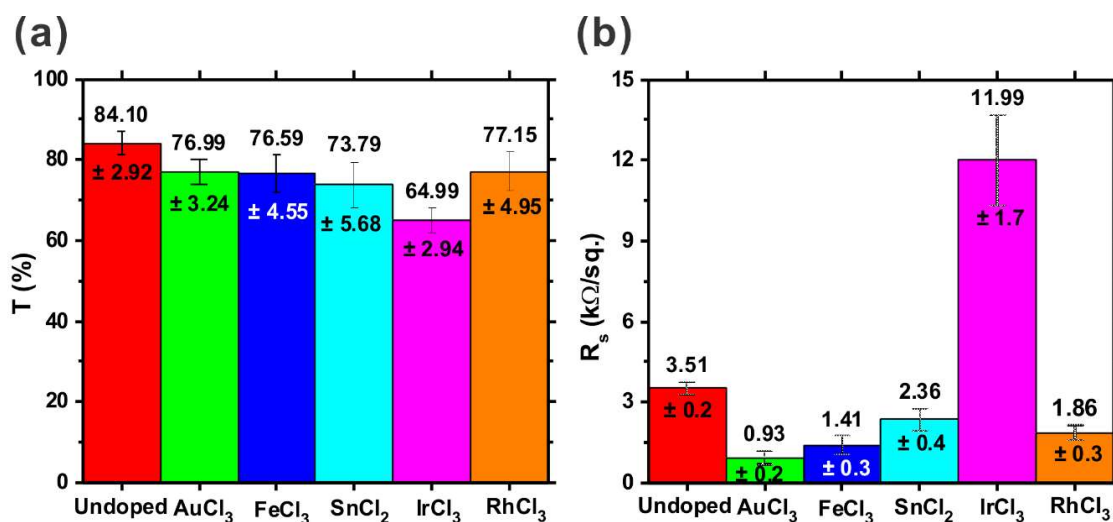
Figure 5.8 Bar charts of mean values of (a) optical transmittance and (b) sheet resistance of undoped and Me$_x$Cl$_y$-doped graphene.

Figure 5.8 (b) summarises the mean R$_S$ for all the dopants considered. AuCl$_3$-doping afforded the lowest R$_S$ (0.9 ± 0.2 kΩ/sq.), showing a rather dramatic decrease (△R$_S$ = 2.6 k Ω/sq.). The highest R$_S$ was for the IrCl$_3$-doped graphene (12.0 ± 1.7 kΩ/sq.). Graphene electrodes are attractive for the flexible display industry; however spatial uniformity in R$_S$ is key if such materials are to be adopted widely in display panels. The R$_S$ and its spatial uniformity intimately dictate light emission uniformity, as discussed previously. Following UVA transfer, the R$_S$ spatial distribution (measured over 4 cm^2) for the undoped graphene was found to be very uniform (±0.2 kΩ/sq.), which was maintained even after chemical doping with AuCl$_3$ (±0.2 kΩ/sq.), FeCl$_3$ (±0.3 kΩ/sq.), SnCl$_2$ (±0.4 kΩ/sq.), and RhCl$_3$ (±0.3 kΩ/sq.). The transfer, rather than the growth or doping procedure, appears to dominate the R$_S$ spatial uniformity. However, the distribution of the R$_S$ standard deviation in the IrCl$_3$-doped (±1.7 kΩ/sq.) was significantly higher than in the undoped case (±0.2 kΩ/sq.) suggesting that, in such systems, the doping procedure dominates the final uniformity. More detailed analysis on this non-uniformity will be presented in the next chapter. Amongst the considered

dopants, $AuCl_3$ is the most effective showing a markedly lower R_S (0.9 ± 0.2 $k\Omega$/sq.) with only a 7.1% decrease in optical transmittance (**Figure 5.8** (a) and (b)).

5.3   Temporal Stability of Metal Chloride-Doping

To assess the time evolution of the doping, the $\%T_{550}$ and R_S were measured immediately after doping and at fixed time points thereafter, as illustrated in **Figure 5.9** (a) and (b).
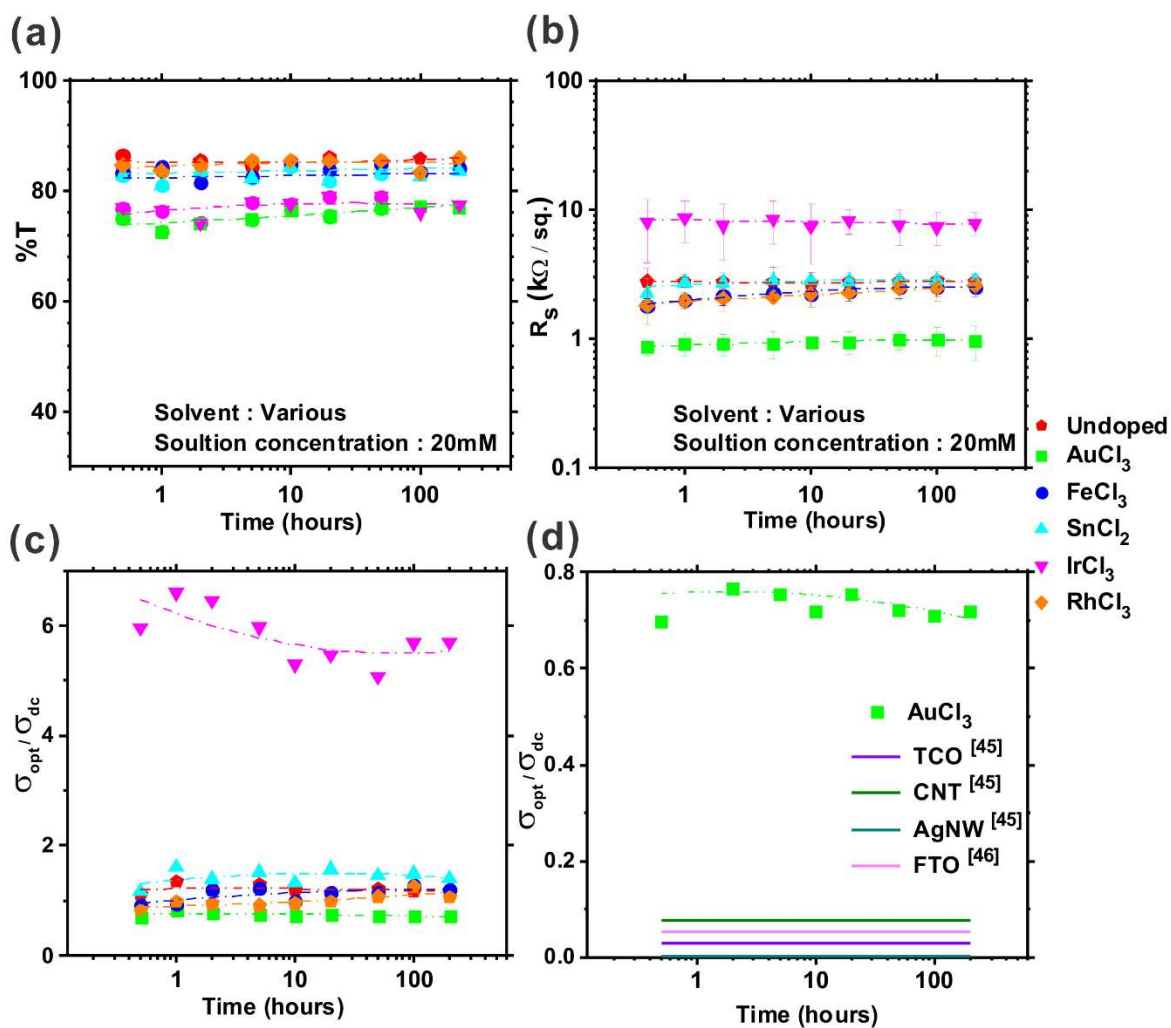
Figure 5.9 Time-dependent properties of chemically doped graphene on PET under ambient conditions: (a) Optical transmittance, (b) sheet resistance of doped graphene, (c) radio of optical conductivity to dc electrical conductivity, and (d) the comparison of the ratio to other conductive transparent media. [45-46]

An ideal transparent conductor necessitates time invariant $\%T_{550}$ and R_S. For all samples, the transmittance decreased following doping, as shown in **Figure 5.9** (a). After exposure to air at STP for 200 hours, undoped graphene maintained its initial $\%T$ and R_S with only a small reduction ($\Delta\%T = -0.8\%$ and $\Delta R_S = -4.53$ Ω/sq.). For the $\%T$ of the doped samples, a recovery process was observed, with the $\%T$ tending to increase, though only marginally so,

with time. The most substantial increase was observed for AuCl$_3$-doped graphene (Δ%T = 1.9%). This increase is presumed to be associated with time-dependent desorption of physisorbed dopants, activated by ambient thermal excitation.[40, 47-49] Desorption also underpins the variation in R$_S$, however, it seems, to a much lesser extent. The increase in R$_S$, for AuCl$_3$-doped graphene, was largely negligible (0.85 kΩ/sq. $\rightarrow$ 0.93 kΩ/sq.). The largest time-dependent change in R$_S$ was observed for RhCl$_3$-doped graphene (1.79 kΩ/sq. $\rightarrow$ 2.56 kΩ/sq.). All doped samples showed an increase in R$_S$ though often by comparatively small shifts.

The ratio of the optical conductance, σ_{opt}, to the DC electronic conductance, σ_{dc}, defines a figure of merit of the opto-electronic performance of transparent conductors, and is commonly estimated from;[45, 50]

$$T = \left[1 + \left(\frac{tZ_0}{2}\right)\sigma_{opt}\right]^{-2} = \left[1 + 188.5\frac{1}{R_S}\left(\frac{\sigma_{opt}}{\sigma_{dc}}\right)\right]^{-2} \qquad (5.1)$$

Here Z_0 is the impedance of free space (377 Ω) and t is the film thickness. For an ideal transparent conductive electrode $\sigma_{opt}/\sigma_{dc} \rightarrow 0$; this necessitates a low R$_S$ and concurrently high %T. The approximate σ_{opt}/σ_{dc} values of our doped transferred graphene, alongside competing transparent flexible conductors, are plotted in **Figure 5.9** (c) and (d), respectively. For all doped samples, $\sigma_{opt}/\sigma_{dc} < 1.40$ and $<\sigma_{opt}/\sigma_{dc}> = 0.74$ for the AuCl$_3$ during the entire measurement period. Though still someway off the industry standard (0.03), these unoptimised devices show promise. It is assumed that some of the dopant molecules adsorbed at defects or grain edges heal the strictly non-contiguous graphene domains desorbed under ambient condition. As shown in the temporal variations, AuCl$_3$ doping seems the most efficient of the Me$_x$Cl$_y$ considered.
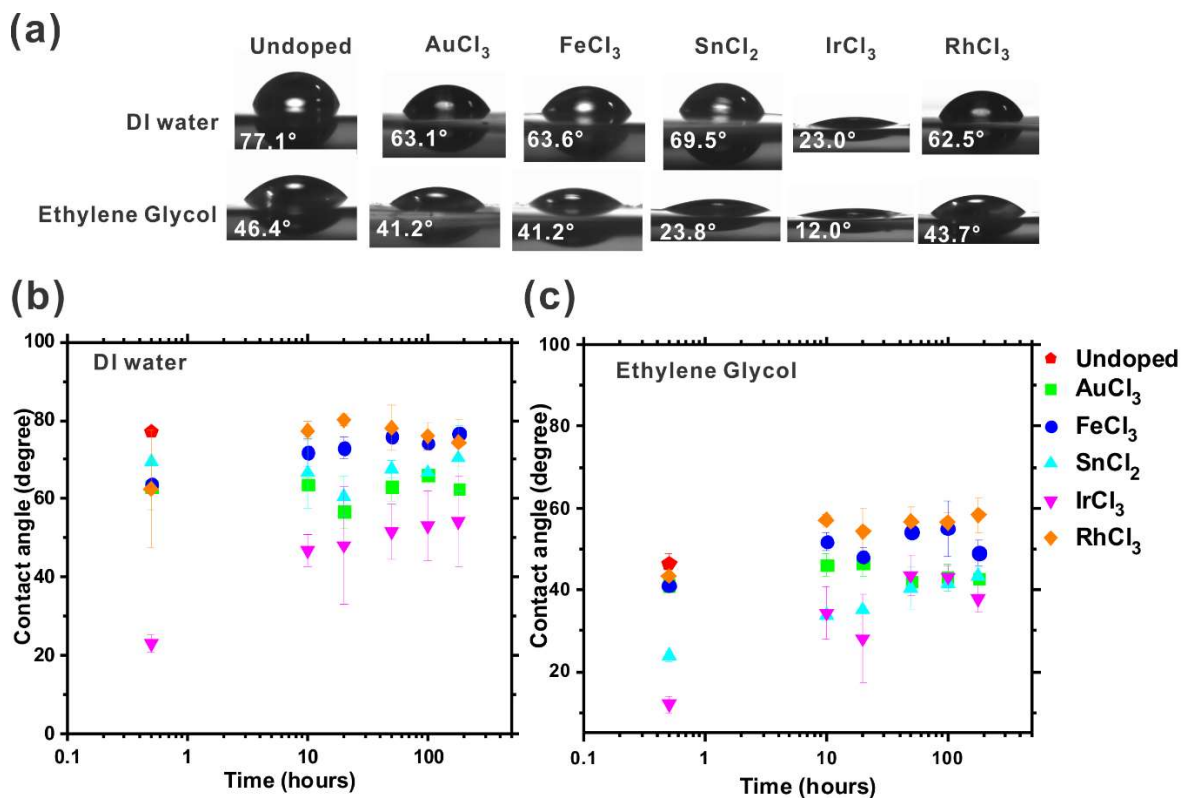
Figure 5.10 (a) DI water and ethylene glycol droplets on chemically doped graphene during the contact angle measurements. Time dependent contact angle of (b) DI water, and (c) ethylene glycol.

Molecular adsorption and desorption on surfaces change the surface potential. Much effort has been made elsewhere to estimate the number of (de)sorbed species in such systems.[51-56] During casting, dopant molecules are physically adsorbed onto the graphene. The contact angle of undoped and doped graphene samples were measured using water and ethylene glycol probes (CAM200, LOT-Oriel Ltd.). The time-dependent contact angle measurements with the DI probe are shown in **Figure 5.10** (b). Initially, after doping the contact angle decreased from 76.4° (undoped) to 63.1° (AuCl$_3$), 62.6° (FeCl$_3$), 69.5° (SnCl$_2$), 23.2° (IrCl$_3$), and 62.5° (RhCl$_3$). After exposure to air for 200 hours, the contact angle increased in FeCl$_3$ (76.7°), RhCl$_3$ (74.3°) and IrCl$_3$ (54.2°), whereas there was no substantial change in the AuCl$_3$ (62.5°) or SnCl$_2$ (70.3°) cases. The surface energy can be calculated by substituting the Young's equation, $\gamma_S = \gamma_{LV} \cos\theta + \gamma_{SL}$ into the Owens-Wendt model[57], to give;

$$\gamma_{LV}(\cos\theta + 1) = 2\left(\gamma_S^d \gamma_{LV}^d\right)^{1/2} + 2\left(\gamma_S^p \gamma_{LV}^p\right)^{1/2} \qquad (5.2)$$

Here γ_{SL} is the surface energy of the interface between the solid surface and liquid probe, γ_{LV} is the surface energy of the liquid probe, γ_S is the surface energy of the solid ($=\gamma_S^d + \gamma_S^p$), γ_S^d is the dispersion term of the surface energy of the solid, γ_S^p is the polar term of surface energy of the solid, γ_{LV}^d is the dispersion term of surface energy of the liquid, and γ_{LV}^p is the polar term of the liquids surface energy. At room temperature and ambient pressure, the surface energy of water is 72.8 mN/m ($=\gamma_{LV}^d + \gamma_{LV}^p = 24.7 + 48.1$) and ethylene glycol is 48.3 mN/m ($=\gamma_{LV}^d + \gamma_{LV}^p = 30.9 + 17.4$)[58].

As plotted in **Figure 5.11** (a), the surface energy of the undoped graphene was 29.4 mJ/m². After doping this increased to 38.8 mJ/m² (AuCl₃), 39.0 mJ/m² (FeCl₃), 44.7 mJ/m² (SnCl₂), 76.9 mJ/m² (IrCl₃) and 38.9 mJ/m² (RhCl₃). After 200 hours, the surface energy decreased for; FeCl₃ (to 33.7 mJ/m²), SnCl₃ (36.0 mJ/m²), IrCl₃ (46.3 mJ/m²) and RhCl₃ (28.8mJ/m²). This change in surface energy is consistent with our earlier %T and R_S findings. When graphene is metal chloride doped there is a measurable increase in the surface energy due to the deposition of local agglomerates and precipitates, empirically verified by our surface energy measurements and corroborated by our measured decreases in %T and R_S. After 200 hours, some of the adsorbed molecular agglomerates of FeCl₃, SnCl₂, IrCl₃ and RhCl₃ are desorbed upon air exposure with samples subsequently exhibiting a decrease in surface energy and increase in R_S. Conversely, AuCl₃ showed a slight increase in surface energy, even after 200 hours air exposure ($\Delta\gamma = 0.18$ mJ/m²). This increase seems to arise from not only a much smaller amount of the dopant molecule desorption than other doped samples, but also possible atmospheric oxygen adsorption. Attachment of oxygen tends to increase the surface energy. To evaluate the amount of desorbed molecules, the change in surface concentration was calculated from the Gibb's isotherm equation;[59-61]

$$d\gamma = -\sum_i \Gamma_i d\mu_i \qquad (5.3)$$

where, γ and $d\mu$ are the surface energy and the change in chemical potential, respectively. Γ is the concentration of adsorbed molecules on the surface, and is termed the surface excess. At constant temperature Γ is given by;[59]

$$\Gamma = -\frac{1}{RT}(\frac{d\gamma}{dlnC})_T \qquad (5.4)$$

Using equation (5.4) the temporal variation of the surface concentration, $\Delta\Gamma$ in the doped graphene was calculated, and is shown in **Figure 5.11** (b). Γ_0 is the surface concentration at t = 0 s, immediately upon its doping, and C is the concentration of dopant solution.
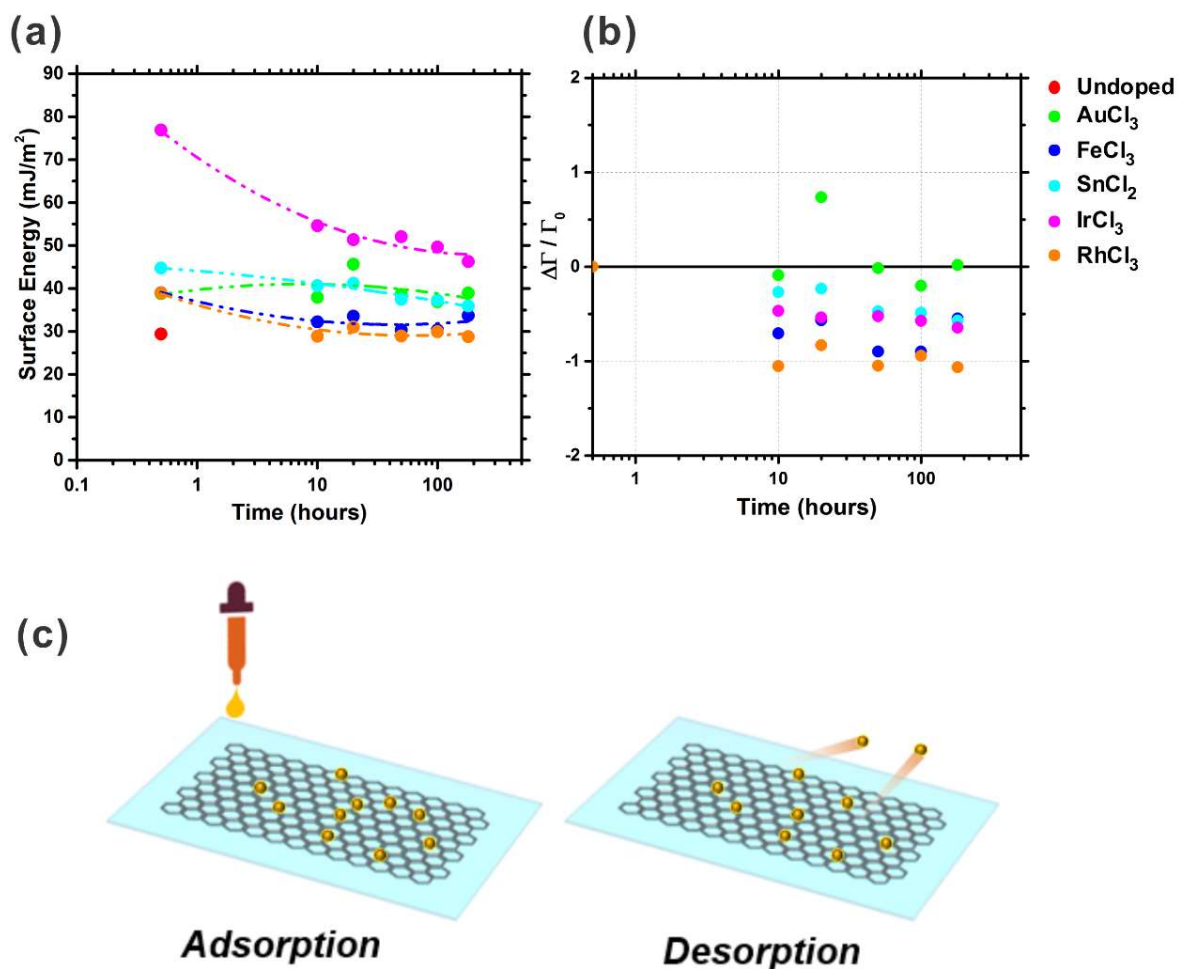
Figure 5.11 Time-dependent variation of (a) surface energy and (b) surface concentration of chemically-doped graphene with metal chlorides, and (c) Schematic illustrating the adsorption and desorption of dopant molecules on graphene.

Figure 5.11 (b) highlights the marked migration of dopant molecules away from, and attached to, the graphene surface. A negative $\Delta\Gamma/\Gamma_0$ with decreasing Γ indicates that the molecules are desorbed from the surface, whilst positive $\Delta\Gamma/\Gamma_0$ suggests the adsorption of molecules. The desorption case is trivial, with the net migration of local absorbents, deposited during the doping process, away from the surface. For AuCl₃-doped graphene, $\Delta\Gamma/\Gamma_0 = 0.019$ (after 200 hours). As indicated above a positive $\Delta\Gamma/\Gamma_0$ implies that additional species, likely ambient oxygen, are being adsorbed onto the graphene surface with absorption rates within the time-frame of study. The absorption of ambient oxygen on nanocarbons is well

103

established.[62-68] On the other hand, the negative values of $\Delta\Gamma/\Gamma_0$ for FeCl$_3$-doped graphene (-0.549), SnCl$_3$-doped graphene (-0.572), IrCl$_3$-doped graphene (-0.644) and RhCl$_3$-doped graphene (-1.064) shows that there was increased desorption. These results are consistent with the temporal variation of resistance, as shown previously in **Figure 5.9** (a). The resistance increase was the lowest in AuCl$_3$-doped graphene (0.08 kΩ/sq.). Therefore, it is apparent that the resistance increase can be attributed to the desorption of dopant molecules which provide charge carriers. Polymer passivation or hermetic capping layers can be utilised to help prevent degradation in ambient conditions. Table 1 summarises the R$_S$ and %T of doped graphene, the temporal variation of the values (ΔR$_S$ and Δ%T), and surface concentration $\Delta\Gamma/\Gamma_0$ after 200 h.

Table 1 Summary of doping results and temporal variations

	Undoped	**AuCl$_3$**	**FeCl$_3$**	**SnCl$_2$**	**IrCl$_3$**	**RhCl$_3$**
R$_S$ (kΩ/sq.)	3.5	0.9	1.4	2.4	12.0	1.9
%T	84.1	77.0	76.6	73.4	65.0	77.2
ΔR$_S$ (kΩ/sq.)	-0.0045	0.1	0.7	0.6	-1.4	0.8
Δ%T	-0.8	1.9	0.9	0.7	0.5	1.4
$\Delta\Gamma/\Gamma_0$	-	0.02	-0.55	-0.57	-0.64	-1.06

5.4 Summary

The hybrid structure of AgNW / graphene exhibited low R$_S$ (57 ± 14 Ω/sq.), but the spatial non-uniformity (R$_S$ deviation = 26 %), voids and incompletely planarized wires found under SEM inspection are presumed to cause light non-uniformity and short circuit issues in an OLED device. Chemical doping has been adopted to concurrently improve the electrical conduction without compromising the optical transparency of our PET-supported graphene. Metal chloride-doped graphene is a promising transparent conductor for flexible electronics

demonstrating better spatial uniformity (R_S deviation < 22 %) than the AgNW / graphene hybrid without the highly perturbed morphology.

As the most effective dopant, 20mM-concentrated $AuCl_3$ decreases the R_S from 2.6 kΩ/sq. to 0.4 kΩ/sq. with a slight decrease of %T from 86.0% to 84.6%. $AuCl_3$–doped graphene exhibited a conductance ratio (σ_{opt}/σ_{dc}) of 0.70 with only a 0.01 increase after 200 hours. This result suggests that the improved characteristics by doping are not significantly degraded in air over time. Using two liquid probes, the surface energy and the concentration change of adsorbed dopant molecules ($\Delta\Gamma/\Gamma_0$) were analysed via contact angle measurements. The largest $\Delta\Gamma/\Gamma_0$ was in $RhCl_3$-doped graphene (-1.06) which demonstrated the largest desorption resulting in the largest increase in resistance (0.8 kΩ/sq.). The experimental results indicate that the molecule desorption is intimately related to the degradation of the electrical resistance of chemically doped graphene. Having studied such time dependent trends there is now a clear need to better understand the enhanced transport occurring upon doping, which is the focus of the following chapter.

References

1.   Geim, A. K., Graphene: Status and Prospects. *Science*, **2009,** *324* (5934), 1530-1534.

2.   Wang, Y.; Tong, S. W.; Xu, X. F.; Özyilmaz, B.; Loh, K. P., Graphene: Interface Engineering of Layer-by-Layer Stacked Graphene Anodes for High-Performance Organic Solar Cells (Adv. Mater. 13/2011). *Advanced Material*, **2011,** *23* (13), 1475-1475.

3.   Novoselov, K. S.; Fal, V.; Colombo, L.; Gellert, P.; Schwab, M.; Kim, K., A Roadmap for Graphene. *Nature*, **2012,** *490* (7419), 192-200.

4.   Novoselov, K. S.; Geim, A. K.; Morozov, S. V.; Jiang, D.; Zhang, Y.; Dubonos, S. V.; Grigorieva, I. V.; Firsov, A. A., Electric Field Effect in Atomically Thin Carbon Films. *Science*, **2004,** *306* (5696), 666-669.

5.   Bae, S.; Kim, H.; Lee, Y.; Xu, X. F.; Park, J.-S.; Zheng, Y.; Balakrishnan, J.; Lei, T.; Ri Kim, H.; Song, Y. I.; Kim, Y.-J.; Kim, K. S.; Ozyilmaz, B.; Ahn, J.-H.; Hong, B. H.; Iijima, S., Roll-to-Roll Production of 30-Inch Graphene Films for Transparent Electrodes. *Nature Nanotechnology*, **2010,** *5* (8), 574-578.

6.   Li, X.; Zhu, Y.; Cai, W.; Borysiak, M.; Han, B.; Chen, D.; Piner, R. D.; Colombo, L.; Ruoff, R. S., Transfer of Large-Area Graphene Films for High-Performance Transparent Conductive Electrodes. *Nano Lett*, **2009,** *9* (12), 4359-4363.

7.   Han, T.-H.; Lee, Y.; Choi, M.-R.; Woo, S.-H.; Bae, S.-H., Extremely Efficient Flexible Organic Light-Emitting Diodes with Modified Graphene Anode. *Nature photonics*, **2012,** *6* (2), 105-110.

8.   Kim, S.-Y.; Kim, J.-J., Outcoupling Efficiency of Organic Light Emitting Diodes Employing Graphene as the Anode. *Organic Electronics*, **2012,** *13* (6), 1081-1085.

9.   Wu, J.; Agrawal, M.; Becerril, H. A.; Bao, Z.; Liu, Z., Organic Light-Emitting Diodes on Solution-Processed Graphene Transparent Electrodes. *ACS Nano*, **2010,** *4* (1), 43-48.

10.   Han, T.-H.; Lee, Y.; Choi, M.-R.; Woo, S.-H.; Bae, S.-H., Extremely Efficient Flexible Organic Light-Emitting Diodes with Modified Graphene Anode. *Nat photonics*, **2012,** *6* (2), 105-110.

11.   Wu, J.; Agrawal, M.; Becerril, H. A.; Bao, Z.; Liu, Z.; Chen, Y.; Peumans, P., Organic Light-Emitting Diodes on Solution-Processed Graphene Transparent Electrodes. *ACS Nano*, **2009,** *4* (1), 43-48.

12.   Sun, T.; Wang, Z.; Shi, Z.; Ran, G.; Xu, W.; Wang, Z.; Li, Y.; Dai, L.; Qin, G., Multilayered Graphene Used as Anode of Organic Light Emitting Devices. *Applied Physics Letters*, **2010,** *96* (13), 133301.

13.   Lee, J.; Cole, M. T.; Lai, J. C. S.; Nathan, A., An Analysis of Electrode Patterns in Capacitive Touch Screen Panels. *Journal of Display Technology*, **2014,** *10* (5), 362-366.

14.   Jaeho, K.; Masatou, I.; Yoshinori, K.; Kazuo, T.; Masataka, H.; Sumio, I., Low-Temperature Synthesis of Large-Area Graphene-Based Transparent Conductive Films Using Surface Wave Plasma Chemical Vapor Deposition. *Applied Physics Letters*, **2011,** *98* (9), 091502.

15.   Lee, X.; Yang, T.; Li, X.; Zhang, R.; Zhu, M.; Zhang, H.; Xie, D.; Wei, J.; Zhong, M.; Wang, K., Flexible Graphene Woven Fabrics for Touch Sensing. *Applied Physics Letters*, **2013,** *102* (16), 163117.

16.   Lin, P.; Choy, W. C. H.; Zhang, D.; Xie, F.; Xin, J.; Leung, C. W., Semitransparent Organic Solar Cells with Hybrid Monolayer Graphene/Metal Grid as Top Electrodes. *Applied Physics Letters*, **2013,** *102* (11), 113303.

17.   Park, H.; Brown, P. R.; Bulovic, V.; Kong, J., Graphene as Transparent Conducting Electrodes in Organic Photovoltaics: Studies in Graphene Morphology, Hole Transporting Layers, and Counter Electrodes. *Nano Letters*, **2012,** *12* (1), 133-140.

18.   Un Jung, Y.; Na, S.-I.; Kim, H.-K.; Jun Kang, S., Organic Photovoltaic Devices with Low Resistance Multilayer Graphene Transparent Electrodes. *Journal of Vacuum Science & Technology A*, **2012,** *30* (5), 050604.

19.   Sun, S.; Gao, L.; Liu, Y., Enhanced Dye-Sensitized Solar Cell Using Graphene-Tio2 Photoanode Prepared by Heterogeneous Coagulation. *Applied Physics Letters*, **2010,** *96* (8), 3113.

20.   Hwang, E.; Adam, S.; Sarma, S. D., Carrier Transport in Two-Dimensional Graphene Layers. *Physical Review Letters*, **2007,** *98* (18), 186806.

21.   Du, X.; Skachko, I.; Barker, A.; Andrei, E. Y., Approaching Ballistic Transport in Suspended Graphene. *Nature Nanotechnology*, **2008,** *3* (8), 491-495.

22.   Bolotin, K. I.; Sikes, K. J.; Jiang, Z.; Klima, M.; Fudenberg, G.; Hone, J.; Kim, P.; Stormer, H. L., Ultrahigh Electron Mobility in Suspended Graphene. *Solid State Communications*, **2008,** *146* (9–10), 351-355.

23.   Novoselov, K. S.; Geim, A. K.; Morozov, S. V.; Jiang, D.; Katsnelson, M. I.; Grigorieva, I. V.; Dubonos, S. V.; Firsov, A. A., Two-Dimensional Gas of Massless Dirac Fermions in Graphene. *Nature*, **2005,** *438* (7065), 197-200.

24.   Ray, S., *Applications of Graphene and Graphene-Oxide Based Nanomaterials*. Elsevier Science: 2015.

25.   Chen, J.; Bi, H.; Sun, S.; Tang, Y.; Zhao, W.; Lin, T.; Wan, D.; Huang, F.; Zhou, X.; Xie, X.; Jiang, M., Highly Conductive and Flexible Paper of 1d Silver-Nanowire-Doped Graphene. *ACS Applied Materials & Interfaces*, **2013,** *5* (4), 1408-1413.

26.   Lee, D.; Lee, H.; Ahn, Y.; Jeong, Y.; Lee, D.-Y.; Lee, Y., Highly Stable and Flexible Silver Nanowire-Graphene Hybrid Transparent Conducting Electrodes for Emerging Optoelectronic Devices. *Nanoscale*, **2013**, *5* (17), 7750-7755.

27.   Tien, H.-W.; Hsiao, S.-T.; Liao, W.-H.; Yu, Y.-H.; Lin, F.-C.; Wang, Y.-S.; Li, S.-M.; Ma, C.-C. M., Using Self-Assembly to Prepare a Graphene-Silver Nanowire Hybrid Film That Is Transparent and Electrically Conductive. *Carbon*, **2013**, *58*, 198-207.

28.   Choi, H. O.; Yang, S. B.; Min, B. H.; Kim, D. W.; Cho, K. M.; Jung, H.-T., Solution-Processable Graphene-Silver Nanowire Hybrids as Transparent Conducting Films. *Science of Advanced Materials*, **2014**, *6* (11), 2304-2311.

29.   Xu, S.; Man, B.; Jiang, S.; Liu, M.; Yang, C.; Chen, C.; Zhang, C., Graphene-Silver Nanowire Hybrid Films as Electrodes for Transparent and Flexible Loudspeakers. *CrystEngComm*, **2014**, *16* (17), 3532-3539.

30.   Dong, H.; Wu, Z.; Jiang, Y.; Liu, W.; Li, X.; Jiao, B.; Abbas, W.; Hou, X., A Flexible and Thin Graphene/Silver Nanowires/Polymer Hybrid Transparent Electrode for Optoelectronic Devices. *ACS Applied Materials & Interfaces*, **2016**, *8* (45), 31212-31221.

31.   Dettlaff-Weglikowska, U.; Skakalova, V.; Graupner, R.; Jhang, S. H.; Kim, B. H.; Lee, H. J.; Ley, L.; Park, Y. W.; Berber, S.; Tomanek, D.; Roth, S., Effect of Socl2 Treatment on Electrical and Mechanical Properties of Single-Wall Carbon Nanotube Networks. *Journal of the American Chemical Society*, **2005**, *127* (14), 5125-5131.

32.   Gunes, F.; Shin, H. J.; Biswas, C.; Han, G. H.; Kim, E. S.; Chae, S. J.; Choi, J. Y.; Lee, Y. H., Layer-by-Layer Doping of Few-Layer Graphene Film. *ACS Nano*, **2010**, *4* (8), 4595-4600.

33.   Kasry, A.; Kuroda, M. A.; Martyna, G. J.; Tulevski, G. S.; Bol, A. A., Chemical Doping of Large-Area Stacked Graphene Films for Use as Transparent, Conducting Electrodes. *ACS Nano*, **2010**, *4* (7), 3839-3844.

34.   Shin, H. J.; Choi, W. M.; Choi, D.; Han, G. H.; Yoon, S. M.; Park, H. K.; Kim, S. W.; Jin, Y. W.; Lee, S. Y.; Kim, J. M.; Choi, J. Y.; Lee, Y. H., Control of Electronic Structure of Graphene by Various Dopants and Their Effects on a Nanogenerator. *Journal of the American Chemical Society*, **2010**, *132* (44), 15603-15609.

35.   Li, X.; Xie, D.; Park, H.; Zhu, M.; Zeng, T. H.; Wang, K.; Wei, J.; Wu, D.; Kong, J.; Zhu, H., Ion Doping of Graphene for High-Efficiency Heterojunction Solar Cells. *Nanoscale*, **2013**, *5* (5), 1945-1948.

36.   Geng, H.-Z.; Kim, K. K.; Song, C.; Xuyen, N. T.; Kim, S. M.; Park, K. A.; Lee, D. S.; An, K. H.; Lee, Y. S.; Chang, Y.; Lee, Y. J.; Choi, J. Y.; Benayad, A.; Lee, Y. H., Doping and De-Doping of Carbon Nanotube Transparent Conducting Films by Dispersant and Chemical Treatment. *Journal of Materials Chemistry*, **2008**, *18* (11), 1261-1266.

37.   Hee Shin, D.; Min Kim, J.; Wook Jang, C.; Hwan Kim, J.; Kim, S.; Choi, S.-H., Annealing Effects on the Characteristics of Aucl3-Doped Graphene. *Journal of Applied Physics*, **2013**, *113* (6), 064305.

38.   Abdou, M. S. A.; Holdcroft, S., Gold-Decorated Poly(3-Alkylthiophenes). *Chemistry of Materials*, **1996**, *8* (1), 26-31.

39.   Ishikawa, R.; Bando, M.; Morimoto, Y.; Sandhu, A., Doping Graphene Films Via Chemically Mediated Charge Transfer. *Nanoscale Research Letters*, **2011,** *6* (1), 111.

40.   Kwon, K. C.; Kim, B. J.; Lee, J.-L.; Kim, S. Y., Effect of Anions in Au Complexes on Doping and Degradation of Graphene. *Journal of Materials Chemistry C*, **2013,** *1* (13), 2463-2469.

41.   Kwon, K. C.; Choi, K. S.; Kim, S. Y., Increased Work Function in Few-Layer Graphene Sheets Via Metal Chloride Doping. *Advanced Functional Materials*, **2012,** *22* (22), 4724-4731.

42.   Kim, K. K.; Kim, S. M.; Lee, Y. H., Chemically Conjugated Carbon Nanotubes and Graphene for Carrier Modulation. *Accounts of Chemical Research*, **2016,** *49* (3), 390-9.

43.   *Compendium of Chemical Terminology*. 2nd ed. ed.; IUPAC: 1997.

44.   Pauling, L., The Chemical Bond. Cornell University Press, Ithaca, New York: 1967.

45.   De, S.; Higgins, T. M.; Lyons, P. E.; Doherty, E. M.; Nirmalraj, P. N.; Blau, W. J.; Boland, J. J.; Coleman, J. N., Silver Nanowire Networks as Flexible, Transparent, Conducting Films: Extremely High Dc to Optical Conductivity Ratios. *ACS Nano*, **2009,** *3* (7), 1767-1774.

46.   Rakhshani, A. E.; Makdisi, Y.; Ramazaniyan, H. A., Electronic and Optical Properties of Fluorine-Doped Tin Oxide Films. *Journal of Applied Physics*, **1998,** *83* (2), 1049-1057.

47.   Tongay, S.; Berke, K.; Lemaitre, M.; Nasrollahi, Z.; Tanner, D. B.; Hebard, A. F.; Appleton, B. R., Stable Hole Doping of Graphene for Low Electrical Resistance and High Optical Transparency. *Nanotechnology*, **2011,** *22* (42), 425701.

48.   Liu, H.; Liu, Y.; Zhu, D., Chemical Doping of Graphene. *Journal of Materials Chemistry*, **2011,** *21* (10), 3335-3345.

49.   Kwon, K. C.; Kim, B. J.; Lee, J.-L.; Kim, S. Y., Role of Ionic Chlorine in the Thermal Degradation of Metal Chloride-Doped Graphene Sheets. *Journal of Materials Chemistry*, **2013,** *1* (2), 253-259.

50.   De, S.; King, P. J.; Lotya, M.; O'Neill, A.; Doherty, E. M.; Hernandez, Y.; Duesberg, G. S.; Coleman, J. N., Flexible, Transparent, Conducting Films of Randomly Stacked Graphene from Surfactant-Stabilized, Oxide-Free Graphene Dispersions. *Small*, **2010,** *6* (3), 458-464.

51.   Eastoe, J.; Dalton, J. S., Dynamic Surface Tension and Adsorption Mechanisms of Surfactants at the Air–Water Interface. *Advances in Colloid and Interface Science*, **2000,** *85* (2–3), 103-144.

52.   Tabrizy, V. A.; Hamouda, A. A.; Denoyel, R., Influence of Magnesium and Sulfate Ions on Wettability Alteration of Calcite, Quartz, and Kaolinite: Surface Energy Analysis. *Energy & Fuels*, **2011,** *25* (4), 1667-1680.

53.   de Lange, M. F.; Lin, L.-C.; Gascon, J.; Vlugt, T. J. H.; Kapteijn, F., Assessing the Surface Area of Porous Solids: Limitations, Probe Molecules, and Methods. *Langmuir*, **2016,** *32* (48), 12664-12675.

54.   Mazeina, L.; Deore, S.; Navrotsky, A., Energetics of Bulk and Nano-Akaganeite, B-Feooh: Enthalpy of Formation, Surface Enthalpy, and Enthalpy of Water Adsorption. *Chemistry of Materials*, **2006,** *18* (7), 1830-1838.

55.   Drazin, J. W.; Castro, R. H. R., Water Adsorption Microcalorimetry Model: Deciphering Surface Energies and Water Chemical Potentials of Nanocrystalline Oxides. *The Journal of Physical Chemistry C*, **2014,** *118* (19), 10131-10142.

56.   Brunauer, S.; Emmett, P. H.; Teller, E., Adsorption of Gases in Multimolecular Layers. *Journal of the American Chemical Society*, **1938,** *60* (2), 309-319.

57.   Owens, D. K.; Wendt, R. C., Estimation of Surface Free Energy of Polymers. *Journal of Applied Polymer Science*, **1969,** *13* (8), 1741-&.

58.   Moutinho, I.; Figueiredo, M.; Ferreira, P., Evaluating the Surface Energy of Laboratory-Made Paper Sheets by Contact Angle Measurements. *Tappi Journal*, **2007,** *6* (6), 26-32.

59.   Chattoraj, D. K., *Adsorption and Thee Gibbs Surface Excess*. Plenum Publishing Corporation: New York 1984; p 451.

60.   Bangham, D. H., The Gibbs Adsorption Equation and Adsorption on Solids. *Transactions of the Faraday Society*, **1937,** *33* (0), 805-811.

61.   Bailey, G. W.; White, J. L., Factors Influencing the Adsorption, Desorption, and Movement of Pesticides in Soil. In *Single Pesticide Volume: The Triazine Herbicides*, Gunther, F. A.; Gunther, J. D., Eds. Springer New York: New York, NY, 1970; pp 29-92.

62.   Mathieu, C.; Lalmi, B.; Mentes, T. O.; Pallecchi, E.; Locatelli, A.; Latil, S.; Belkhou, R.; Ouerghi, A., Effect of Oxygen Adsorption on the Local Properties of Epitaxial Graphene on Sic (0001). *Physical Review B*, **2012,** *86* (3).

63.   Nasehnia, F.; Seifi, M., Adsorption of Molecular Oxygen on Viiib Transition Metal-Doped Graphene: A Dft Study. *Modern Physics Letters B*, **2014,** *28* (30).

64.   Giannozzi, P.; Car, R.; Scoles, G., Oxygen Adsorption on Graphite and Nanotubes. *The Journal of Chemical Physics*, **2003,** *118* (3), 1003-1006.

65.   Valentini, L.; Armentano, I.; Lozzi, L.; Santucci, S.; Kenny, J. M., Interaction of Methane with Carbon Nanotube Thin Films: Role of Defects and Oxygen Adsorption. *Materials Science and Engineering: C*, **2004,** *24* (4), 527-533.

66.   Park, N.; Han, S.; Ihm, J., Effects of Oxygen Adsorption on Carbon Nanotube Field Emitters. *Physical Review B*, **2001,** *64* (12), 125401.

67.   Collins, P. G.; Bradley, K.; Ishigami, M.; Zettl, A., Extreme Oxygen Sensitivity of Electronic Properties of Carbon Nanotubes. *Science*, **2000,** *287* (5459), 1801-1804.

68.   Sorescu, D. C.; Jordan, K. D.; Avouris, P., Theoretical Study of Oxygen Adsorption on Graphite and the (8,0) Single-Walled Carbon Nanotube. *The Journal of Physical Chemistry B*, **2001,** *105* (45), 11227-11232.

Chapter 6   Conduction in Me$_x$Cl$_y$ doped Graphene

6.1   Introduction

Though promising and industrially attractive, the high sheet resistance of CVD graphene necessitates the development of improved methodologies to allow integration into the various large area flexible electronics technologies. To realise the potential of CVD graphene, novel transfer approaches and Me$_x$Cl$_y$ chemical doping have been herein suggested and the mechanical, optical, and electrical performances of the doped graphene have been demonstrated in previous chapters. The optimally chemically doped graphene exhibited reduced R$_S$ (2.6 kΩ/sq. $\rightarrow$ 0.4 kΩ/sq.) without any significant decrease in %T (86.1% $\rightarrow$ 84.6%) increasing the viability of CVD graphene as a transparent conducting material in flexible electronics. This chapter extends these efforts by investigating the detailed temperature dependent electron transport within the doped graphene materials, focussing on the shift in work function and the associated impacts of dopant agglomerate formation.

An analysis on how the developed doping strategy can decrease the R$_S$ of graphene will be described based on the electrical and optical measurements of pristine and doped graphene. Then, the modification of work function and carrier transport of doped graphene will be discussed alongside the temperature-dependent resistance variation results.

6.2   Doping Mechanism and Spatial Analysis

6.2.1   Charge Transfer Doping

Chemical doping was adopted because it does not induce significant mechanical modification of the graphene backbone, unlike substitutional doping which is often achieved through aggressive plasma-based processing. The in-solution metal chloride molecules mediate effective charge transfer to the graphene basal plane. As described in **Figure 6.1** (a), the molecules are physically adsorbed mediating spontaneous charge transfer across well-defined energy levels at the graphene-metal ion interface. In the present system the anticipated reactions between the metal chloride and graphene are; [1]

$$\text{Graphene} + 3\text{MeCl}_3 \rightarrow \text{Graphene} + \text{MeCl}_2^- + \text{Me(I)} + \text{MeCl}_4^- \tag{6.1}$$

$$\text{MeCl}_2^- \rightarrow \text{Me}^0 + 2\text{MeCl}_4^- + 2\text{Cl}^- \tag{6.2}$$

$$\text{MeCl}_4^- + \text{Graphene} \rightarrow \text{Grahpene}^+ + \text{Me}^0 + 4\text{Cl}^- \tag{6.3}$$
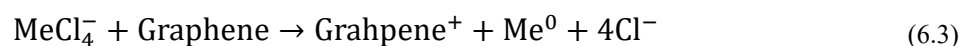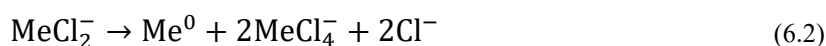
The positive Me^{3+} ions in MeCl^{4-} tend to be neutralised following charge donation to the graphene. Depending on the metal type, the positive reduction potentials of the metal ions result in the removal of a given proportion of the local electrons population from the graphene substrate. E_F is shifted to lower energy mediating *p*-type doping, as described in **Figure 6.1** (b).

The dispersed SnCl_2 interaction differs from the other considered metal chlorides. Since SnCl_2 reacts in H_2O, producing Sn(OH)Cl and HCl,[2] we note that;

$$\text{Sn(OH)Cl} + \text{HCl} + \text{Graphene} + \text{O} \rightarrow \text{SnO}_2 + 2\text{HCl} + \text{Graphene}^- \tag{6.4}$$
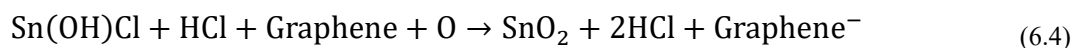
The aqueous SnCl_2 behaves as a reducing agent. The Sn^{2+} ions react with bound oxygen species, deposited during ambient exposure, on the graphene. When the oxygen constituent is removed, the graphene becomes negatively charged, leading to *n*-type doping. In this case, E_F is moved to a higher energy level, as depicted in **Figure 6.1** (c).
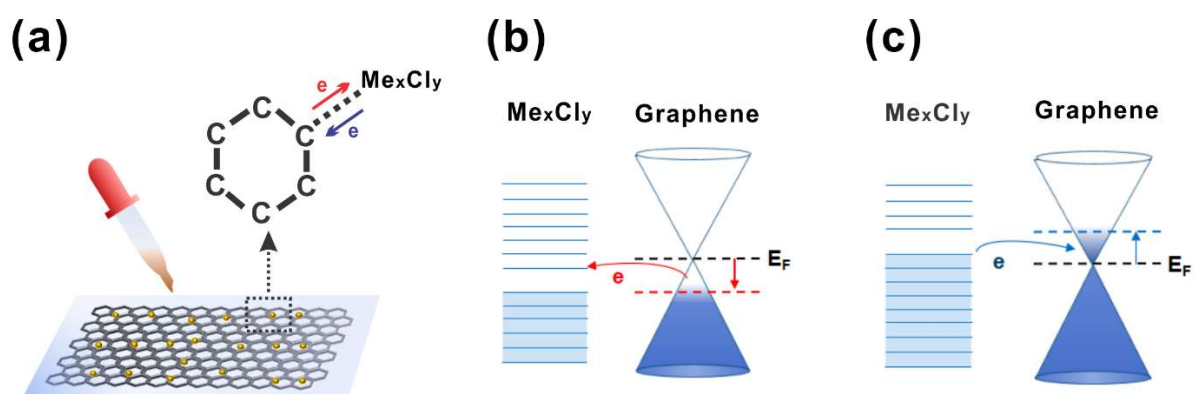
Figure 6.1 Schemes illustrating (a) charge transfer mediated by chemical doping resulting in E_F shift from Dirac point to (b) lower level (*p*-type) and (c) higher level (*n*-type).

6.2.2   Spatial Analysis of Doped graphene
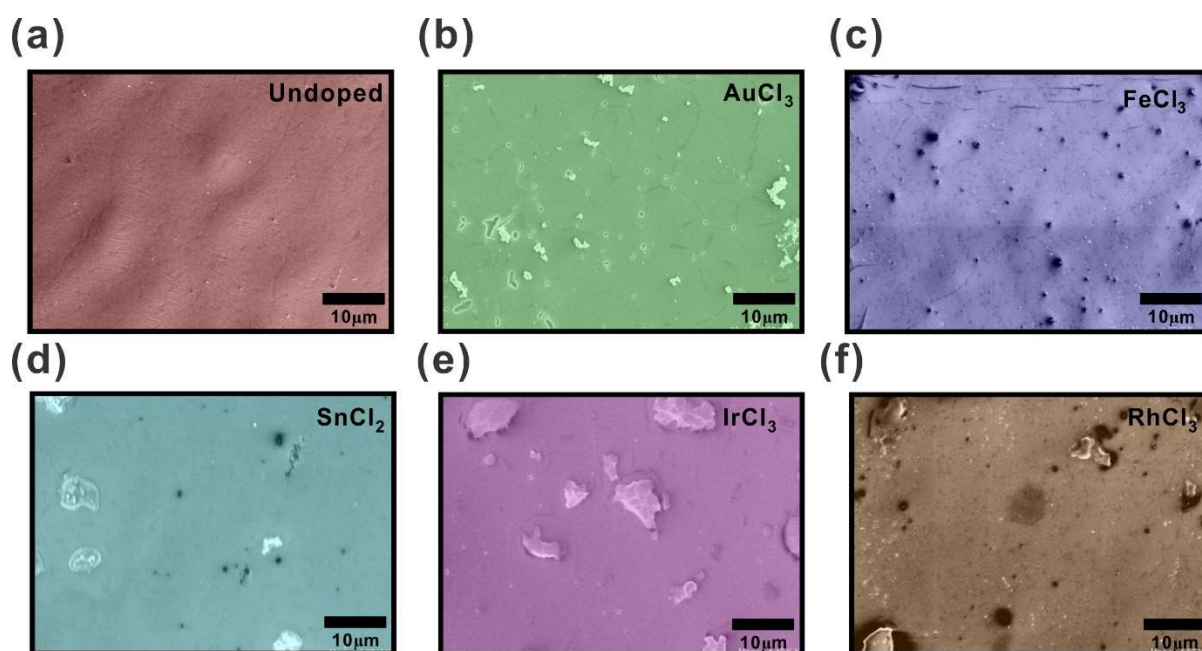
Figure 6.2 SEM micrographs of (a) undoped, (b) AuCl₃-, (c) FeCl₃-, (d) SnCl₂-, (e) IrCl₃-, and (f) RhCl₃-doped graphene.

As seen in the SEM image (**Figure 6.2** (b) – (f)), particles some 5 μm - 15 μm in diameter appear on the surface of all the doped samples. No particles were noted on the graphene prior

113

to doping (**Figure 6.2** (a)). EDX spectroscopy (**Figure 6.3** (a)) suggests that such particles are likely metallic dopant agglomerates which were formed from incomplete dissolution of the powdered dopant, or from charge transfer induced agglomeration. As described above, the metal chlorides transfer surplus charge to the graphene basal plane leaving charge-neutral metal atoms (Me^0) or SnO_2. Such neutral metallic constituents tend to aggregate under aqueous conditions and are subsequently fixed upon drying, with their formation dictated by the magnitude of their cohesive energy. The total areal coverage and number of agglomerate particles are illustrated in **Figure 6.3** (b). $AuCl_3$-doped graphene shows the largest number of agglomerates, however the size of these agglomerates are somewhat smaller (~0.1 μm), compared to $SnCl_2$ (~2 μm) and $IrCl_3$ (~14 μm). The largest total area occupied by the agglomerates was upon $IrCl_3$-doping. Although the number of agglomerates was smaller than that of the $AuCl_3$-doped, the average diameter of agglomerates was significantly larger (14.4 μm) than that of the $AuCl_3$ (0.1 μm), and the total agglomerate area was the largest upon $IrCl_3$-doping (9.91 %). The diameters of the Ir agglomerates had a large standard deviation of 3.7 μm, which is likely the source of the reduced spatial uniformity, whilst the size deviation of agglomerates from other Me_xCl_y-doped was some 10 times smaller on average. The agglomerate distribution is consistent with the non-uniform R_S area distribution of $IrCl_3$-doped graphene in Chapter 5 (**Figure 5.7** (e)).
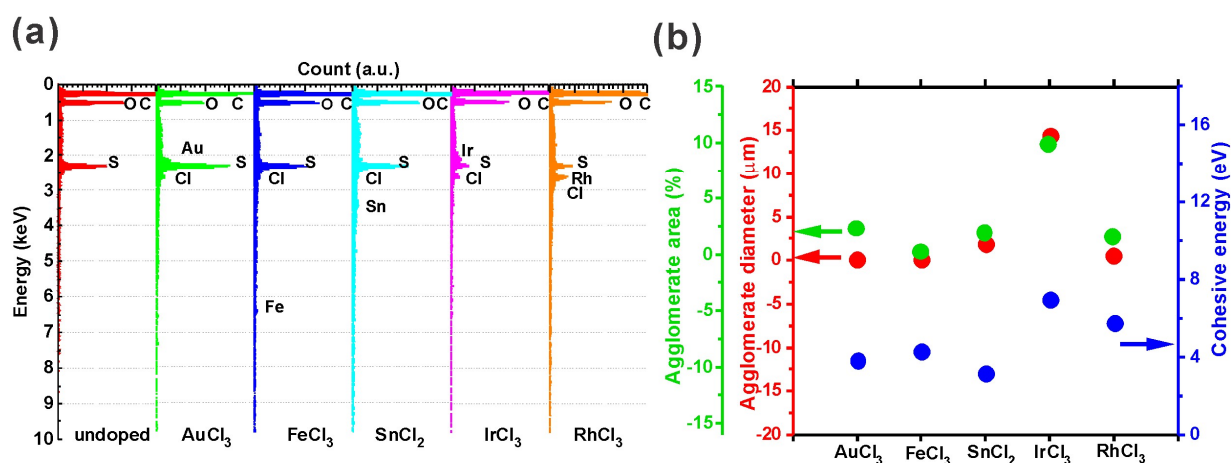
Figure 6.3 (a) Energy-Dispersive Xray (EDX) spectroscopy of undoped and Me$_x$Cl$_y$ doped graphene and (b) comparison of metal cohesive energy and agglomerate diameters and agglomerate area.

Cohesive energy is defined as the energy needed to subdivide a metal into isolated atoms by destroying all metallic bonds.[3-6] Thus, low cohesive energy metals are readily separated by chemical reactions, whilst the high cohesive energy metals stay as comparably large particles. The calculated cohesive energy of the metallic constituents within the metal chlorides has been reported elsewhere, as shown in **Figure 6.3** (b).[7] There appears a strong correlation between the cohesive energy and the degree of agglomeration of the neutral metallic species. The cohesive energy seems to play a contributing role in agglomerate formation following charge transfer. The large cohesive energy of Ir (6.94 eV) indicates that Ir has perhaps the greatest likelihood of inducing significant agglomeration, consistent with our experimental findings (**Figure 6.3** (b)). SnCl$_2$ was somewhat anomalous. The cohesive energy of Sn (3.14 eV) was larger than that of Au (3.81 eV) and Fe (4.28 eV), however the average diameter of agglomerates (1.95 μm) was larger than Au (0.11 μm) and Fe (0.12 μm). The agglomerate-covered area for Sn (1.96 %) was smaller than Au (2.39 %), but larger than Fe (0.31 %), which is largely inconsistent with the presented cohesion-driven agglomeration. This likely relates to the disparate doping mechanism associated with SnCl$_2$ compared with the other considered Me$_x$Cl$_y$. SnO$_2$ remains after SnCl$_2$ doping. No Sn neutral species are formed and thus there is little correlation between the generation of SnO$_2$ and the Sn cohesive energy.
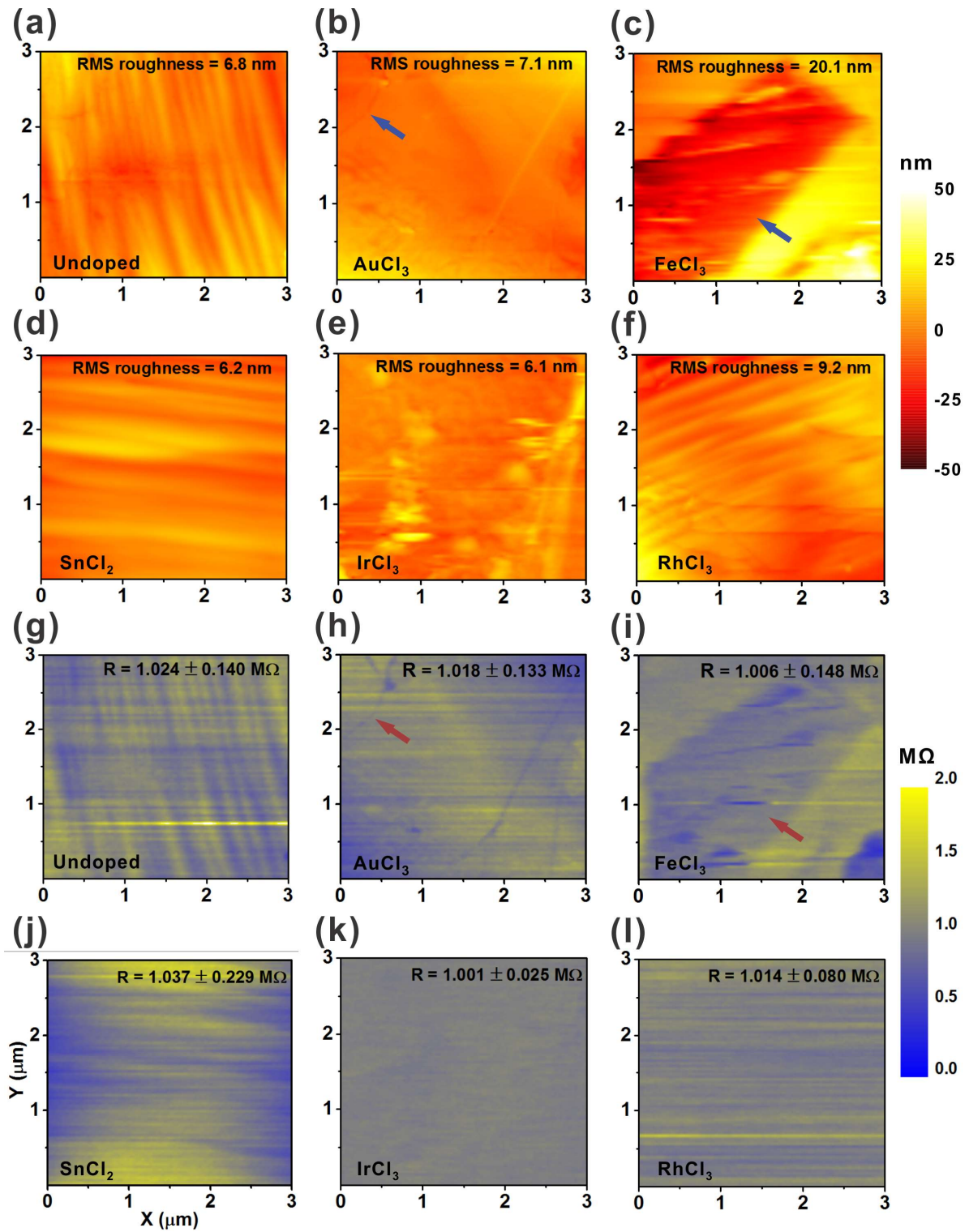
Figure 6.4 Atomic Force Microscopic (AFM) maps: (a) undoped, (b) AuCl₃-, (b)FeCl₃-, (d) SnCl₂-, (e) IrCl₃-, (f) RhCl₃-doped graphene and Scanning Spreading Resistance Microscopic maps: (g) undoped, (h) AuCl₃-, (i) FeCl₃-, (j) SnCl₂-, (k) IrCl₃-, (l) RhCl₃-doped graphene. Blue and red arrows indicate valley areas and low resistance areas, respectively.

To further investigate the areal uniformity of the chemical doping, sub-micro-scale scanning spreading resistance mircoscopry (SSRM)[8-9] was performed using a conductive cantilever (Applied NanoStructures, Inc., SICONA) mounted in an atomic force microscope (AFM, Veeco Instruments Inc., Dimension icons). 3 µm x 3 µm maps were produced with the samples edge electrically grounded. In the present study, SSRM has a spatial resolution of Δx,y ~ 11.7 nm, allowing us to probe the relationship between surface roughness and spreading resistance upon doping, whilst also allowing comparison of the nanoscale and macroscale conductance distributions, the latter of which was measured via macroscale contact four-point probe mapping. For the undoped graphene, SSRM and surface morphology are near coincident (**Figure 6.4** (a) and (g)); surface protrusions tend to have lower resistance than valleys of comparable vertical dimensions. In some areas of the AuCl$_3$ doped graphene (blue arrows in AFM - **Figure 6.4** (b), and for which the red arrow indicates in **Figure 6.4** (h)), areas of narrow and lower-height seem to be a line defect in graphene which can be expected to have higher resistance than nominally flat areas. However, the low-height line showed lower resistance, which differs from the earlier trend noted for the undoped graphene. We find that dopant molecules adhered to defects, grain boundaries, cracks and non-idealities in the graphene. Grain healing is notable upon Me$_x$Cl$_y$ doping. Chang *et. al.* argued that adatoms on graphene tend to dwell on atomic steps or boundaries therein breaking the lattice periodicity.[10] Dopant molecules are readily adsorbed on defects and subsequently heal them. Such molecules are too small to be detected via AFM, but nonetheless contributed to a measurable change in the conduction. The dopant distribution seems somewhat inhomogeneous, with a tendency for them to accrue at edges, steps, grain boundaries, or line defects. The conductive edge and grain boundaries may possibly contribute to the charge transport by functioning as a percolation network of sub-nanometer, pseudo-metallic wires.
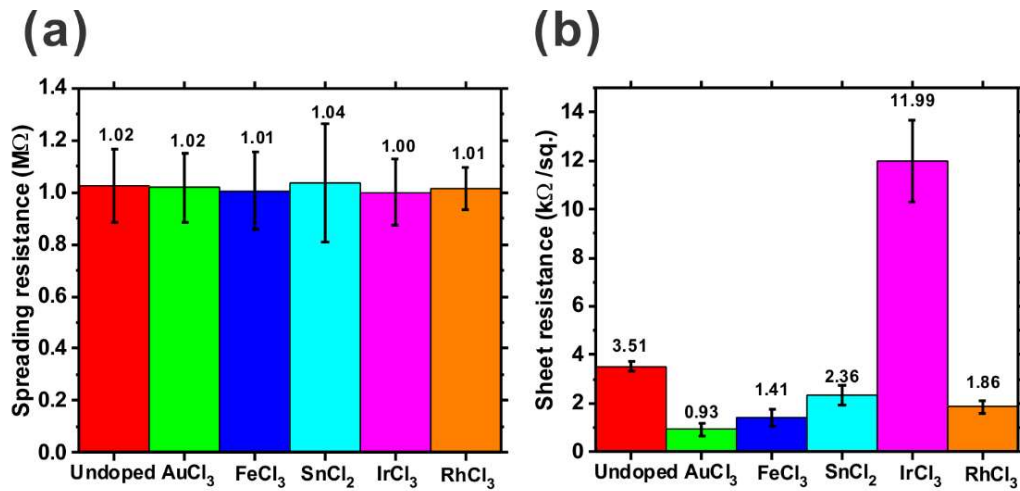
Figure 6.5 Comparison of (a) spreading resistance and sheet resistance (R_S) measured by SSRM and four-point probe, respectively.

As shown in **Figure 6.5** (a) and (b), the resistance measured by SSRM is around 1 MΩ, which is some three orders of magnitude higher than the sheet resistance measured using a macroscale four-point probe (Jandel Four-Point probe). The measured resistance contains subsidiary resistance terms from the measurement setup, including probe and contact resistances, both of which are significant in the present measurements. The average spreading resistance across the measured areas showed similar values for all the dopants (1.00 MΩ ($IrCl_3$) - 1.04 MΩ ($SnCl_2$)). The lowest SSRM was for $IrCl_3$-doped (**Figure 6.5** (a)), whilst the large area macroscale sheet resistance (400 mm^2) of the $IrCl_3$ was the highest (**Figure 6.5** (b)). The difference in resistance between the SSRM and four-point probe measurement suggests the possibility that $IrCl_3$ doped graphene likely has disparate, scale-dependent conduction mechanisms.

Surface metrology suggests that dopant agglomeration at defects and grain edges are critical in healing the otherwise imperfect, non-contiguous transferred graphene, with the efficient Me_xCl_y doping.

6.3   Charge Transfer and Work Function

The presented chemical doping methodology has proven capable of lowering the electrical resistance of CVD graphene facilitating its use as an electrode in various applications. An additional benefit from this approach is the work function tuning of graphene making it an ideal material for applications where work function optimisation is needed such as in various nano field electron emission applications,[11-13] carrier injection layers in OLEDs[14-15] and solar cells.[16-18] Charge transfer from dopants induce E_F shifts and as a result the work function can be accurately modified.[19-20]In this chapter the charge transfer and work function modification are presented alongside optical measurement (Raman/ Xray photoemission spectroscopy (XPS)) and electrical measurements (KPFM / Hall).

6.3.1   Work Function Tuning of Graphene

Raman spectroscopy is the long-used standard in investigating the electronic structures of materials.[21-26] In this study, the position of the graphene Raman peaks were investigated before and after chemical doping. The strong PET Raman cross-section, whose many peaks overlap with established graphene peaks, made it challenging to obtain meaningful spectra from the doped polymer supported samples. Thus, graphene on SiO_2 was used herein. As shown in **Figure 6.6** (a),the I_D/I_G ratio of the graphene was 0.13 ± 0.01 and the I_{2D}/I_G ratio was 1.69 ± 0.31, collectively indicating a well-graphitised material.[27-28] The measured 2D peak shift ($\Delta\omega_{2D}$) for each dopant is plotted in **Figure 6.6** (b). The 2D peak of the $AuCl_3$, $FeCl_3$, $IrCl_3$, and $RhCl_3$ were blue shifted by 24.4 cm^{-1}, 6.9 cm^{-1}, 4.3 cm^{-1}, and 7.9 cm^{-1}, respectively from that of the undoped graphene (2726 cm^{-1}), suggesting *p*-type doping to varied degrees. $SnCl_2$-doping showed no notable shifts, contrary to the red shift (*n*-doping) suggestion outlined in literature and our earlier findings.[29-32] The reason for this absence of shift remains unclear. The largest blue-shift was observed in $AuCl_3$-doped graphene (24.4 cm^{-1}) whilst $FeCl_3$, $IrCl_3$, and $RhCl_3$ showed similar shifts of < 8 cm^{-1}. When dopant molecules are adsorbed on graphene, electrons transfer from metal chloride molecules to graphene (*n*-type doping) or from graphene to the molecules (*p*-type doping).[33-35]   The Raman analysis supports the notion that charge transfer occurs from the molecular forms of metal chloride

(MeCl$_4^-$) to graphene, which is consistent with previous reports.[1, 33] The Raman findings also corroborate the earlier sheet resistance findings (**Figure 6.5** (b)); with the lowest R$_S$ occurring for AuCl$_3$-doped which showed the largest 2D-peak blue shift.

(a)

(b)
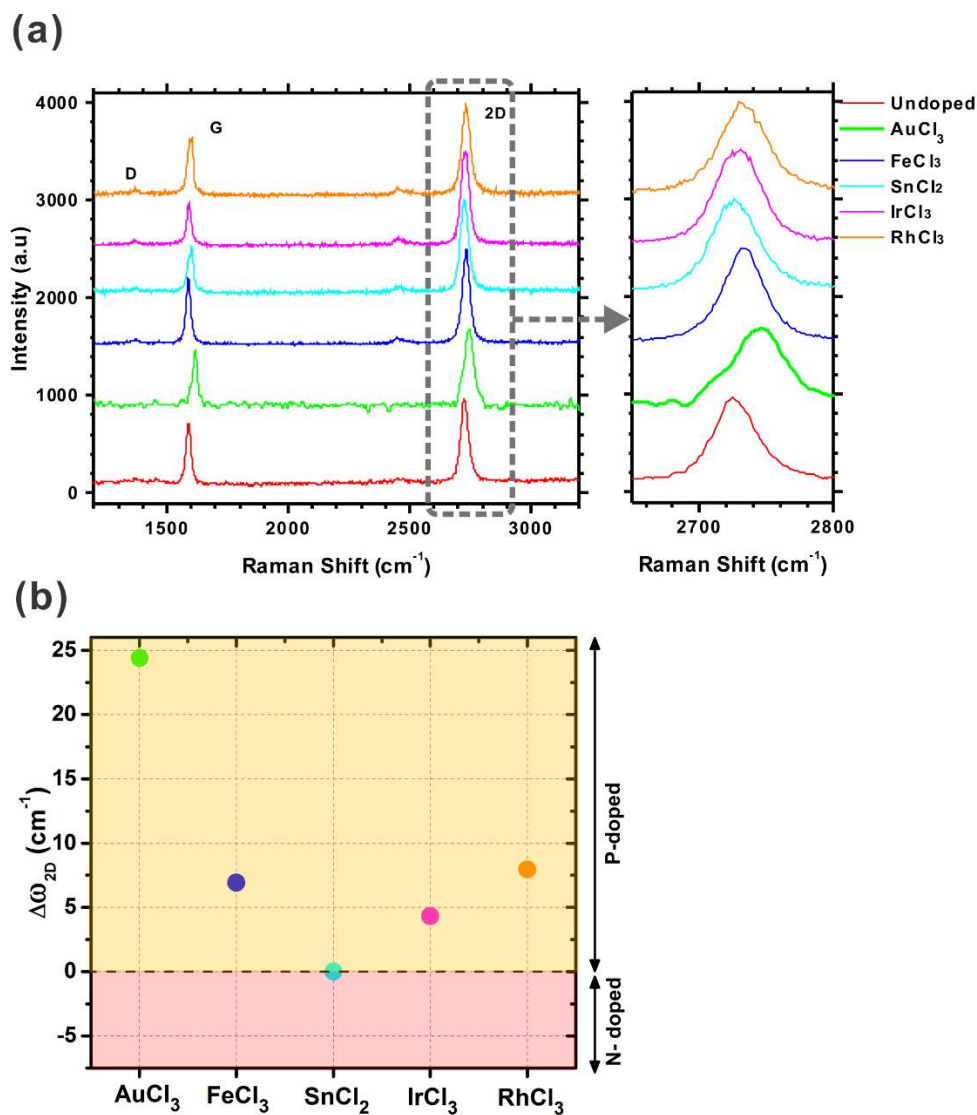
Figure 6.6 (a) Raman spectra (457 nm) of undoped and Me$_x$Cl$_y$ doped graphene (transferred to Si/SiO$_2$) and (b) the associated 2D peak shift ($\Delta\omega_{2D}$).

X-ray Photoemission Spectra (XPS) were acquired using an Mg source (1253 eV) with an energy resolution of 0.092 eV. To measure the change in work function following chemical

doping, Ultraviolet Photoemission Spectra (UPS) were measured using a He I lamp (21.2 eV) with an energy resolution of 0.061 eV. For XPS and UPS measurement, the as-grown graphene was transferred to polished Mo substrates as our earlier efforts showed that the polymer and thermally oxidised silicon substrates used previously induced serious charging effects.

By collecting electrons which have various kinetic energies, the work function and binding energy can be determined. With the secondary electron cut-off ($E_{cut-off}$) from UPS spectra, as shown in **Figure 6.7** (a), the work function (Φ) can then be calculated.[36-37]

$$\phi = h\nu - (E_{cut-off} - E_F) \tag{6.5}$$

where hv is the photon energy of incident X-ray. The work function of the doped graphene shifted by +0.23 eV (AuCl$_3$), +0.32 eV (FeCl$_3$), +0.11 eV (IrCl$_3$), and +0.13 eV (RhCl$_3$) from pristine graphene, indicating *p*-doping in these cases, whilst SnCl$_2$-doped graphene exhibited nearly the same work function as the undoped graphene with only +0.06 eV shift which is consistent with Raman results.
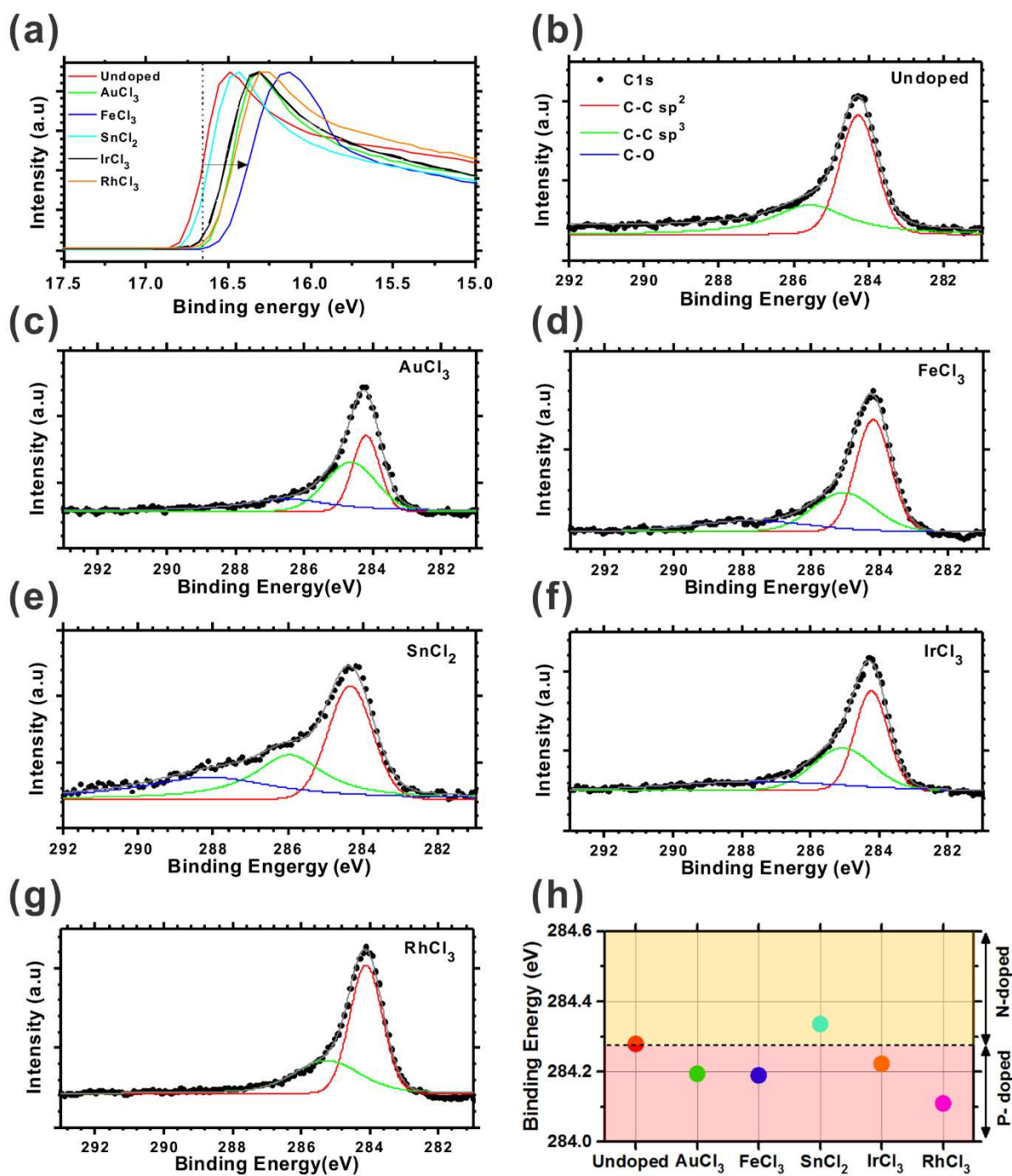
Figure 6.7 Secondary UPS cut-off, XPS C1s peak for (b) undoped, (c) AuCl₃-, (d) FeCl₃-, (e)SnCl₂-, (f) IrCl₃-, and (g) RhCl₃-doped graphene, and (h) C-C sp² peak position of the pristine graphene and upon metal chloride doping.

The Voigt-convolution-fitted [38] XPS C1s peak of the undoped and the Me_xCl_y doped graphene are shown in **Figure 6.7** (b) to (g). Two principle carbon bonding components; C-C sp^2 at 284.6 eV and and C-C sp^3 at 285.8 eV, alongside the oxygen containing functional groups (C-O (hydroxyl) and C=O (Carboxyl) at 286.0 eV and 287 eV, respectively) are noted. In all doped cases, the sp^3 peak does not seriously increase upon doping, indicating that there are few sites of severe defect generation induced by the doping procedure. Conversely, however; the C-O bond does increase when doped with $AuCl_3$ (286.4 eV), $FeCl_3$ (287.2 eV), $SnCl_2$ (287.6 eV), and $IrCl_3$ (287.5 eV), even though there is no observable C-O peak (286 - 287 eV) in the undoped graphene and $RhCl_3$-doped graphene. The highest C-O peak occurred in the $SnCl_2$-doped graphene. It is possible that residual SnO_2 products deleteriously bond to the graphene basal plane. Charge transfer can be examined via the C1s sp^2 peak shift, attributable to E_F modification. As described in **Figure 6.7** (h), following chemical doping, the undoped graphene peak (284.28 eV) shifted to lower values for $AuCl_3$ (284.19 eV), $FeCl_3$ (284.19 eV), $IrCl_3$ (284.22 eV), and $RhCl_3$ (284.11eV) indicating p-doping, whilst it moved to higher binding energy in $SnCl_2$-doped graphene (284.34 eV) indicating n-doping. There was no additional peak generated from metal chloride-carbon bonding which is a significant benefit compared to substitutional[39] or thin film deposition doping.[40] Chemical doping of polymer supported graphene under the present framework seems like a promising approach to increase the conductivity and offer control over E_F without severely affecting the atomic structure of graphene.

Raman spectroscopy, UPS and XPS collectively suggested, indirectly that charge transfer underpins the present observed chemical doping. However, direct evidence on the amount of charge transfer can be gleaned by Hall measurements. Van der Pauw geometries (12 mm x 12 mm) were fabricated and measured at room temperature under a 2 kG field (**Figure 6.8**).
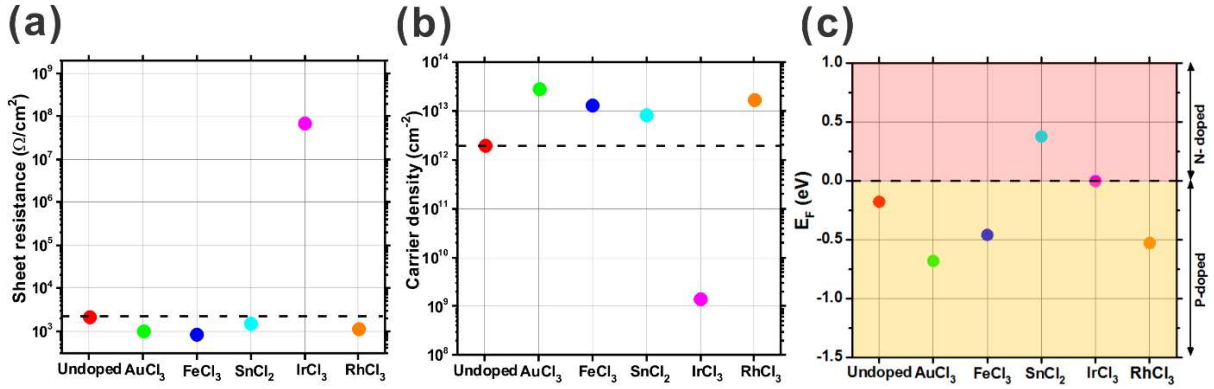
Figure 6.8 Hall measurement of undoped and Me$_x$Cl$_y$-doped graphene: (a) sheet resistance (R$_S$), (b) carrier density, and (c) E$_F$ calculated with the carrier density values.

The R$_S$ decreased from 2148 Ω/cm^2 (undoped graphene) to 1026 Ω/cm^2 (AuCl$_3$), 853 Ω/cm^2 (FeCl$_3$), 1521 Ω/cm^2 (SnCl$_2$), and 1109 Ω/cm^2 (RhCl$_3$). The R$_S$ reduction is consistent with our earlier macro-scale four-point probe measurements. Only IrCl$_3$-doped graphene exhibits a higher R$_S$ (68 MΩ/cm^2) than the undoped sample. The carrier density of undoped graphene was 2.0x10^{12} cm^{-2} which is comparable to published values (9.3x10^{11} – 3.4x10^{12} cm^{-2}),[40-44] whereas the carrier density of the doped graphene increased by roughly an order of magnitude (8.5x10^{12} cm^{-2} (SnCl$_2$) - 2.8x10^{13} cm^{-2} (AuCl$_3$)). Only IrCl$_3$ doped graphene showed a lower carrier density (1.4x10^9 cm^{-2}). The majority carrier in the SnCl$_2$-doped case were electrons, whilst for all the other dopants holes were the majority carrier, in agreement with our XPS results.

The E$_F$ position can be defined by the Fermi velocity (v$_F$=1x10^6 m/s) of graphene and carrier density (n) via :[45]

$$E_F(n) = \hbar \, | \, v_F \, | \, \sqrt{\pi n} \qquad\qquad (6.6)$$

where $\hbar$ is Plank constant. The E$_F$ of undoped graphene was negatively shifted by 0.18 eV from the Dirac point indicating slight *p*-doping, compatible with the fact that the majority carrier type of undoped graphene are holes. The slight *p*-doping might be due to doping from ambient oxygen[46], as previously discussed, or from aqueous ammonium persulfate residues

124

from the etching of the metal catalyst during the transfer process.[46-48] Chemically doped graphene clearly showed large E_F shifts (-0.5 eV (AuCl$_3$) to +0.55 eV(SnCl$_2$)), as shown in **Figure 6.8** (c). The measured mean work function depends on the net charge carrier density.[49] The charge transfer from dopants breaks the net charge equilibrium. Charge dipoles are generated which rearrange the electrostatic potential resulting in a work function shift.[49] The Hall measurements directly demonstrate that chemical doping can successfully tune the work function of graphene. Successful *p*-type tuning will enhance the luminous efficiency for advanced OLED applications or solar cells, whilst *n*-type tuning increases the electron field emission performance.

Kelvin probe force microscopy (KPFM) is an AFM based technique that can map the variation in surface potential relative to that of conductive tip.[50-54] In this study a KPFM (Bruker Co., Peak Force KPFM) was employed to independently corroborate and map the measured work function shifts upon chemical doping. As a standard reference sample, a HOPG surface was scanned for calibration of the tip. Then, the surface potential of graphene was scanned over 20 μm x 20 μm with a conductive KPFM tip and the graphene work function ($\varphi_{Graphene}$) was extracted (**Figure 6.9).** The measured work function of undoped graphene was 4.72 eV, which was slightly higher than the previously reported (4.66 eV).[55-56] This is likely due to unintentional doping of the graphene following interaction with water and oxygen in the ambient atmosphere and during the catalyst etching in aqueous $(NH_4)_2S_2O_8$, which collectively stimulates slight sample-to-sample variations.[46-48] The work function of the SnCl$_2$-doped graphene was -0.13 eV shifted from the undoped graphene, whilst the rest of the doped graphene showed positive shifts in their work functions (0.07 - 0.31 eV). As seen, the areal distribution of the work function is uniform with the standard deviation per unit area of 0.04 eV (RhCl$_3$) to 0.21 eV (FeCl$_3$) across 20 μm x 20 μm scan areas. No particular inhomogeneous patterns in the maps for undoped graphene and other doped graphenes were observed, apart from in the IrCl$_3$-doped graphene.
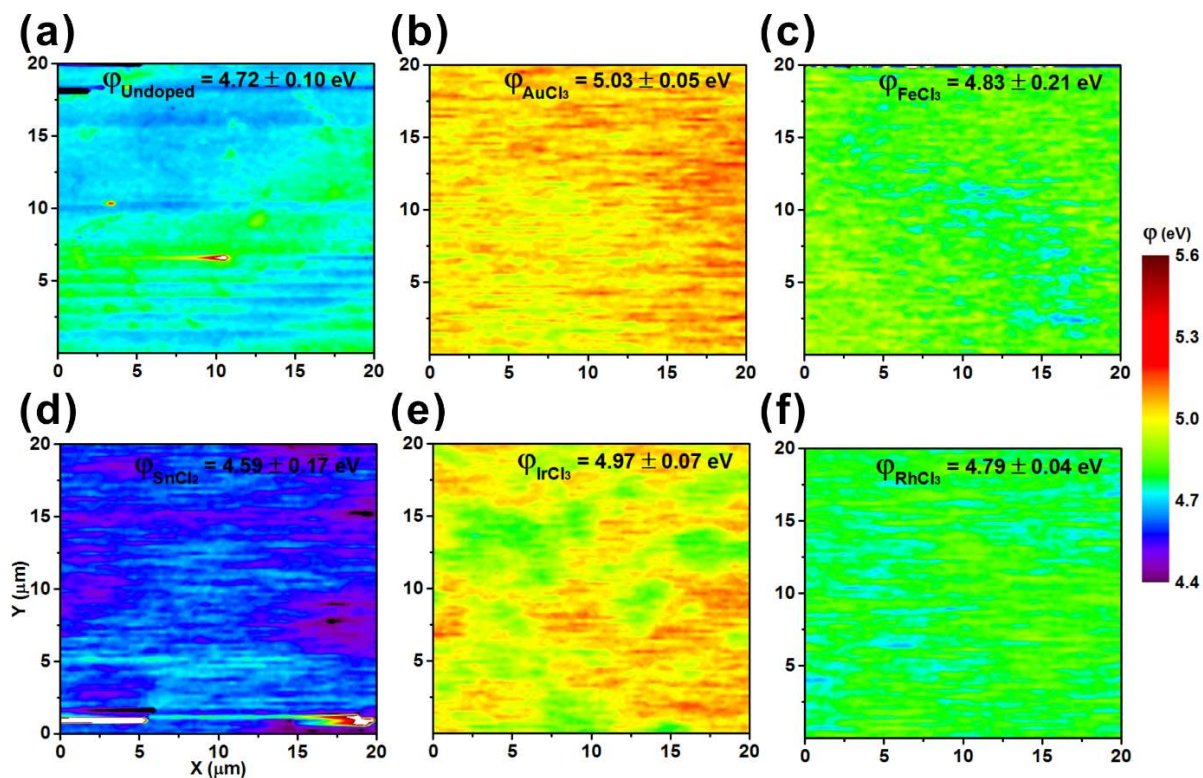
Figure 6.9 Kelvin Probe Force Microscopy (KPFM) maps: (a) undoped, (b) AuCl₃-, (c) FeCl₃-, (d) SnCl₂-, (e) IrCl₃-, and (f) RhCl₃-doped graphene

6.3.2 Gibb's Free Energy and Reduction Potential of Dopants

Figure 6.10 (c) shows a comparison of the work function shift for all doped samples obtained by KPFM, UPS, Hall measurement and Density Function Theory (DFT). DFT calculations were performed using Material Studio 7.0 and DMol^3 with calculations based on a 3 nm x 3 nm graphene basal plane. The generalized gradient approximation with a Perdew–Burke–Ernzerhof functional (GGA-PBE) was applied for the exchange-correlation function. The trend in the work function shift from the DFT models was similar to the KPFM results, but FeCl₃, SnCl₂ and RhCl₃ doping showed a ~0.3 eV higher work function in all cases compared to KPFM, UPS or Hall measurement. The difference between DFT calculation and measured work function values is likely attributed to the fact that the graphene we used for the measurements was unintentionally doped in ambient condition, alongside effects associated

with the proximal substrate or UV adhesive used for transfer. However, the trend of work function shift from DFT is consistent with our other empirical methods.
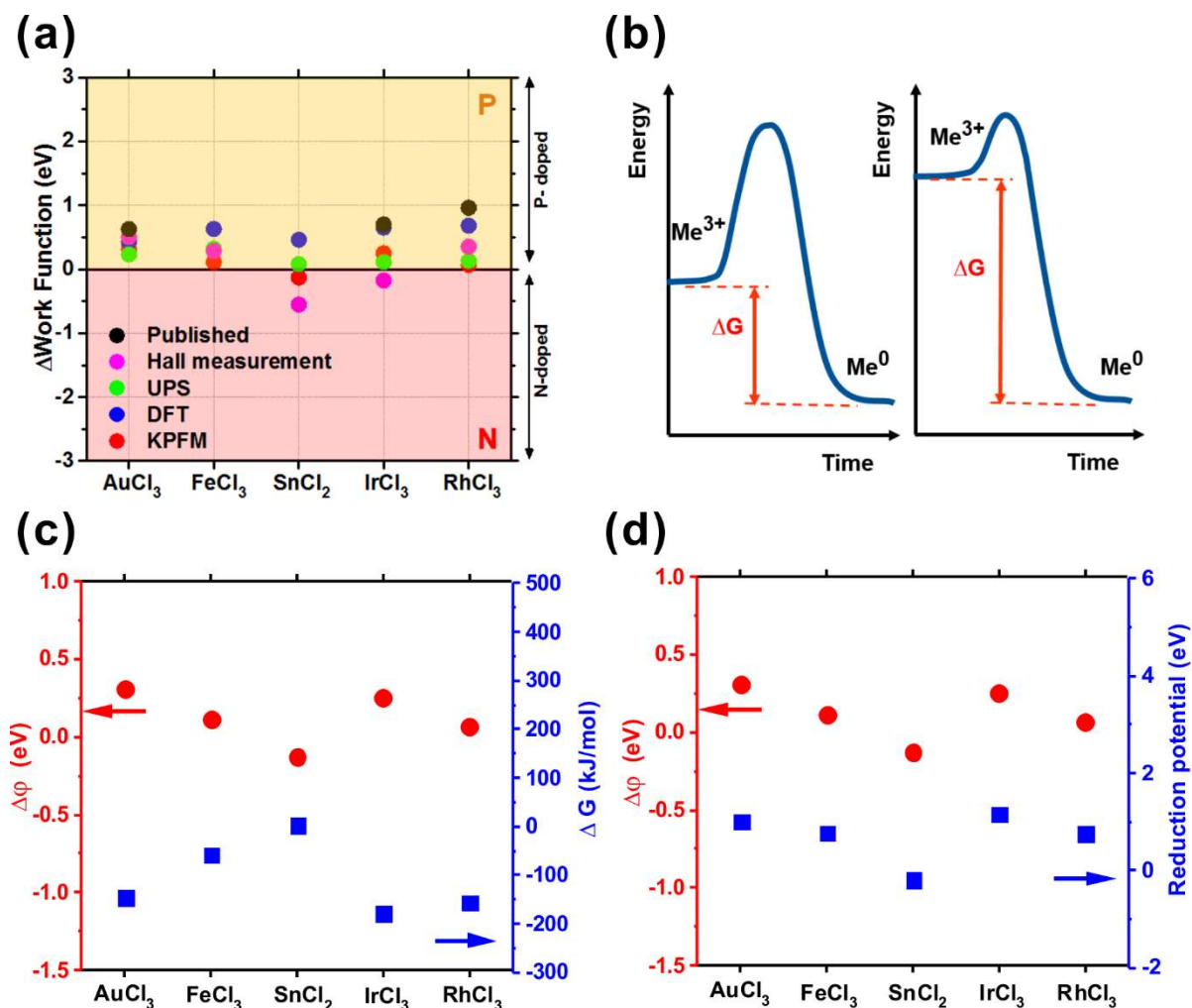
Figure 6.10 (a) Comparison of measured work function and published data, (b) an example plot of charge transfer reaction of graphene by Me_xCl_y, and comparison of work function shift values measured by KPFM with (c) Gibb's free energy and (d) reduction potential.

Achieving a high degree of charge transfer is key to increasing the doping level, which depends on the Gibb's free energy and the reduction potential of the dopants. The Gibb's free energy (ΔG) is defined as the thermodynamic potential used to calculate the maximum or

reversible work that may be performed by a thermodynamic system at a constant temperature.[57] Charge transfer is endothermic ($\Delta G < 0$); it readily accelerates the reaction when ΔG is highly negative, as described in **Figure 6.10** (b). The metallic ions (Me^{3+}) are increasingly likely to achieve neutrality (Me^0) with larger $|\Delta G|$ by transferring positive charge to the graphene. There is an increasing likelihood of charge transfer with larger $|\Delta G|$, resulting in a large work function shift. The Gibb's free energy of the metallic constituents is compared with the empirically assessed work function values (KPFM) in **Figure 6.10** (c).[58] The mirrored trend in the work function in relation to ΔG is clear. A high work function shift was observed in $AuCl_3$ (0.31 eV) and $IrCl_3$-doped graphene (0.25 eV) with negatively large ΔG ($AuCl_3$: -145.7 kJ/mol and $IrCl_3$: -179.9 kJ/mol).[58]

Another influential parameter in driving the rate and direction of charge transfer in the present 2D system is the reduction potential.[59] As seen in **Figure 6.10** (d), the work function of the doped graphene has a similar trend with the reduction potential of the metallic ions. The positive reduction in the metal chloride dopants ($AuCl_3$, $FeCl_3$, $IrCl_3$, and $RhCl_3$) results in the removal of a given proportion of the local electron population. The reduction reaction mediates *p*-type doping, leaving Me^0 products. If the reduction potential is high, the rate of charge transfer increases, resulting in a large increase in work function. For *n*-type doping from $SnCl_2$, the reduction potential is negative for oxidation of Sn^{2+} (-0.19 V)[58]. There is a tendency to donate electrons to graphene, whilst the other dopants tend to accept electrons with positive potentials ($AuCl_3$: 1.002 V, $FeCl_3$: 0.77 V, $IrCl_3$: 1.156 V, and $RhCl_3$: 0.76 V)[58]. We thus anticipate that the graphene doped with $AuCl_3$, $FeCl_3$, $IrCl_3$ and $RhCl_3$ show nominally *p*-type behaviour, whereas graphene doped with $SnCl_2$ would exhibit nominally *n*-type behaviour. The work functions assessed by KPFM, UPS and Hall measurement are consistent with the results as shown in **Figure 6.10** (a).

6.4 Charge Transport in Doped Graphene

Charge transport in graphene does not adhere to standard models previously reported for either semiconductors or metals. Graphene has a conical band structure. The conduction band touches the valence band at a Dirac point.[60] In pristine graphene, there is no bandgap. The density of states is nearly zero near E_F indicating neither semiconducting nor metallic behaviour. Due to this peculiarity in electronic structure, electrical conduction in graphene is often likened to a disordered conducting material and described by variable range hopping (VRH).[61-63] To investigate the charge carrier behaviour further, the effects of temperature on the electrical resistance in pristine graphene has been studied widely.[64-67] However, the carrier transport model of doped graphene has rarely been reported. This section will present a model of charge transport in doped graphene based on experimental results.

6.4.1 Hopping Transport

Variable Range Hopping (VRH) has been often implicated as a common charge transport mechanism in such ensembled nanomaterials.[65, 68] VRH is defined as the conduction by phonon-assisted quantum tunnelling between disordered localised states near E_F, where the resistance (R) can be expressed as a function of temperature, T as: [65, 69]

$$R(T)^{-1} = R_0^{-1} \exp\left[-\left(\frac{T_0}{T}\right)^{\frac{1}{P}}\right]$$

(6.7)

where T_0 is tunnelling parameter and p = (d+1), where d is the dimensionality of hopping. The tunnelling transport is characterised by Mott's 3D VRH, Mott's 2D VRH or the Efros/Shklovskii (ES) VRH with $\exp(-T^{1/4})$, $\exp(-T^{1/3})$ and $\exp(-T^{1/2})$ dependence, respectively.[70] At low temperatures, the density of states in partially ordered systems is not constant. Electrons leave holes when they hop from one atom to the next. [71-73] Thus, the system acquires sufficient energy to overcome the Coulombic interaction for hoping transport. This is termed ES VRH which can be observed at very low temperatures (<10 K)[71] due to electron-hole puddles brought about from extrinsic substrate effects.[73]
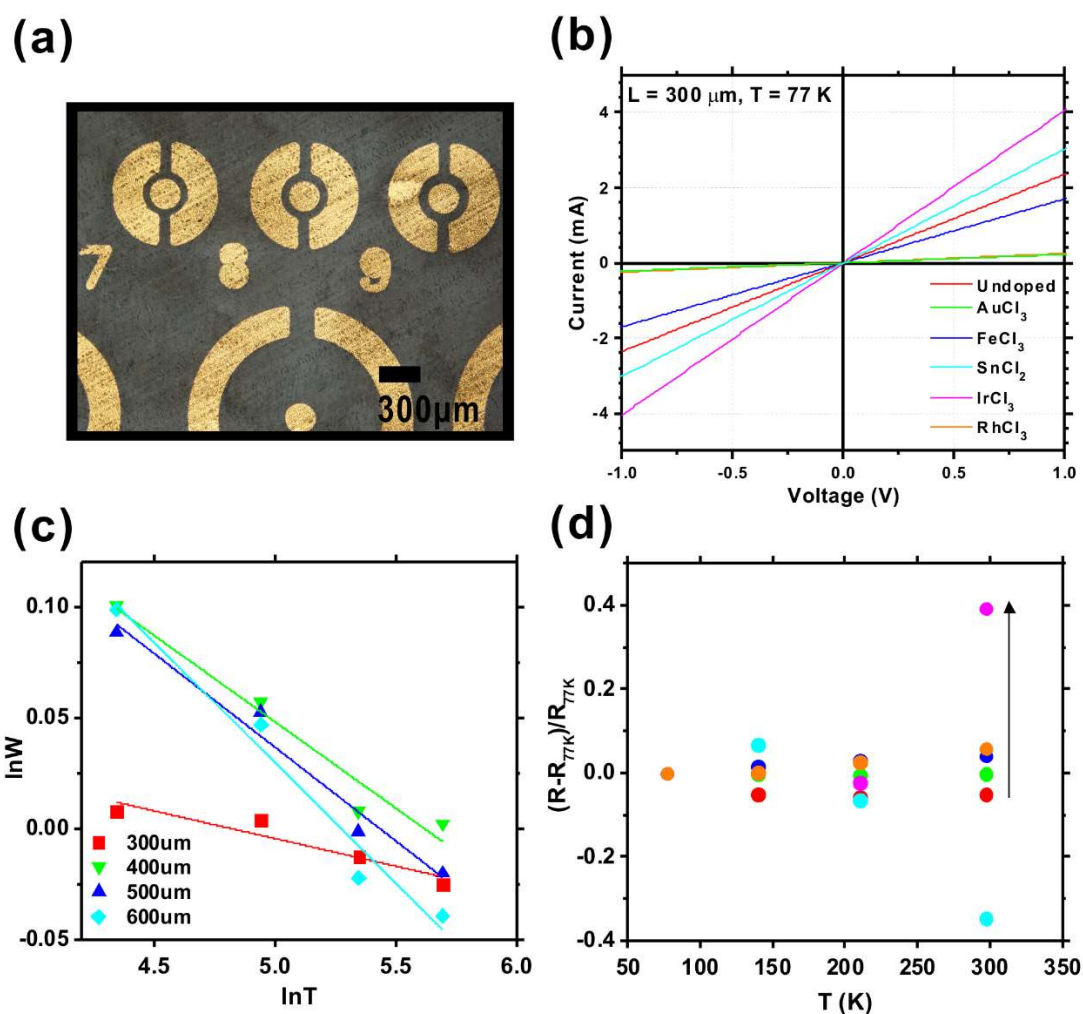
Figure 6.11 (a) A microscopic image of Cr/Au contact electrodes thermally deposited using a shadow mask on PET substrate for current-voltage (IV) measurement, (b) the IV curves of undoped and Me_xCl_y-doped graphene measured at 77 K (L = 300 μm), (c) a logarithmic derivative of electrical resistance calculated from the IV measured at various temperature, and (d) the normalised resistance change with increasing temperature.

VRH has been considered for pristine graphene with E_F at the Dirac point.[65] However, E_F can clearly be adjusted by chemical doping and lead to new transport regimes. To investigate conduction in our doped graphene, the current-voltage (IV) characteristics were measured as a function of temperature, from 77 K to room temperature (297 K). Cr/Au (10/80 nm) contacts were thermally evaporated and defined via shadow masking of circular transmission lines (**Figure 6.11** (a)), for a range of channel lengths (L = 200 - 500 μm), allowing the use of

130

empirical access to the contact resistance. As seen in **Figure 6.11** (b), the I-V characteristics of doped graphene's (L=300 μm) measured at 77 K are linear with the current level of $AuCl_3$, $RhCl_3$, and $FeCl_3$ doped graphene being lower than that of the undoped graphene. For a detailed analysis, the differential resistance at zero bias voltage, R = (dV_0/dI) was calculated for all temperatures. The calculated differential resistance, in $IrCl_3$- and $SnCl_2$-doped cases were 10^2 to 10^{10} times larger than other doped samples and the undoped graphene. The reasons for this large resistance will be discussed in the next section. By fitting the resistance (R) vs T curve with equation (6.7), we can gain insight into the dominant transport mechanism for our pristine and doped graphene. Undoped graphene shows an exponentially decreasing resistivity with temperature, over the measured temperature range, but other doped graphene samples show increasing resistivity as temperature rises at higher than a certain temperature (~ 120 K). Such trends are not captured using standard VRH-like models.

The Zabrodskii's Reduced Activation Method (RAM)[74] was used in order to determine the functional form of the T-dependent resistivity of VRH conduction. In this method, the reduced activation energy ($W = T^{-1}\partial \ln R/\partial T^{-1}$) can be expressed as $W(T) = A + x(T_0/T)^P$ by substituting the VRH model, $R(T)^{-1} = R_0^{-1} \exp[-(T/T_0)]^{\frac{1}{P}}$, we have

$$\ln W(T) \approx \ln(x(T_0)^P) - p \ln(T) \tag{6.8}$$

where $\ln(x(T_0)^P)$ is the y-intercept and p is the gradient for lnW(T) plotted as a function of ln(T). Using equation (6.8) we plotted the R of $AuCl_3$-doped graphene (**Figure 6.11** (c)). From the fitting, the extracted exponent, p, was 0.08 – 0.11 which is not within the range predicted by either the Mott VRH or ES VRH models. The exponent values outside of the VRH range (0.25 – 0.33) suggests that doping forces the transport to deviate from conventional VRH transport. To examine the T-dependent R trend modified by chemical doping, the change in resistance from the resistance at 77K (R-R_{77K}) was calculated at L = 500 μm (**Figure 6.11** (d)). The undoped graphene has decreasing R (R- R_{77K} < 0), but the R of the doped graphene increases (R- R_{77K} > 0) with increasing T. It can be assumed that chemical doping reduces the resistance but the resistance increases slightly by increasing T. The doped graphenes show a larger R increase than undoped graphene at room temperature, as highlighted in **Figure 6.11** (d). Therefore, another model is required.

131

6.4.2 A Carrier Transport Model for Chemically Doped Graphene

Park *et. al.* suggested a three-termed transport model for the temperature–dependent conduction in polycrystalline graphene and proved the model by fitting the measured resistance from 8 K to room temperature.[74] By adding Thermal Activation (TA) and Nearest Neighbour Hopping (NNH) to the existing VRH model, this composite modelled was expressed as; [74]

$$R(T)^{-1} = R_{TA}{}^{-1} \exp\left(-\frac{E_\alpha}{k_B T}\right) + R_{NNH}{}^{-1} \exp\left(-\frac{E_n}{k_B T}\right) + R_{VRH}{}^{-1} \exp\left[-\left(\frac{T_0}{T}\right)^{\frac{1}{P}}\right] \qquad (6.9)$$

where E_a is the thermal activation energy, k_B is the Boltzman constant, E_n is the NNH activation energy, and R_{TA}, R_{NNH}, and R_{VRH} are the TA, NNH, and VRH constants, respectively. They suggested that the grain boundaries function as metallic sub-nanoscale wires mediating tunnelling between neighbouring metallic wires which themselves are dominated by NNH. In this thesis, such conductive line defects were observed in SSRM, suggesting that edge-mediated conduction in doped graphene can be enhanced by preferential aggregation of dopant molecules. The Park model matched our findings well for T < 140 K (R^2 =0.94), but the increasing R vs. T curves of doped graphene did not match the model as the NNH component is an exponentially decaying term. In such a model there is no term to explain the increasing trend observed in our experimental data.

The conduction models outlined above focus on pristine graphene with E_F at the Dirac point, or semiconducting graphene. There is no discussion for degenerately doped graphene, which has a high carrier density. Chemical doping increases the carrier density and modifies E_F resulting in metallic behaviour. Metallic behaviour and an abundance of charge carriers may result in the electrical resistance from electron-phonon or electron-defect scattering at high temperatures. In this thesis a new, augmented model is proposed that explains the observed electrical conduction in doped graphene for the entirety of the temperature range considered.

Central to this is the introduction of an increasing resistance term at high temperatures due to effective phonon coupling effects, as;

$$R(T)^{-1} = R_{TA}^{-1} \exp\left(-\frac{E_\alpha}{k_B T}\right) + R_{NNH}^{-1} \exp\left(-\frac{E_n}{k_B T}\right) + R_{VRH}^{-1} \exp\left[-\left(\frac{T_v}{T}\right)^{\frac{1}{3}}\right] + R_M^{-1}\left[1 + \alpha(T - T_0)\right] \qquad (6.10)$$

where E_n is the NNH activation parameter, T_v is the tunnelling parameter, α is the temperature coefficient, T_0 is the reference temperature at which the resistance linearly increases with increasing T (usually room temperature), and, R_M is the resistance at T_0.[75]
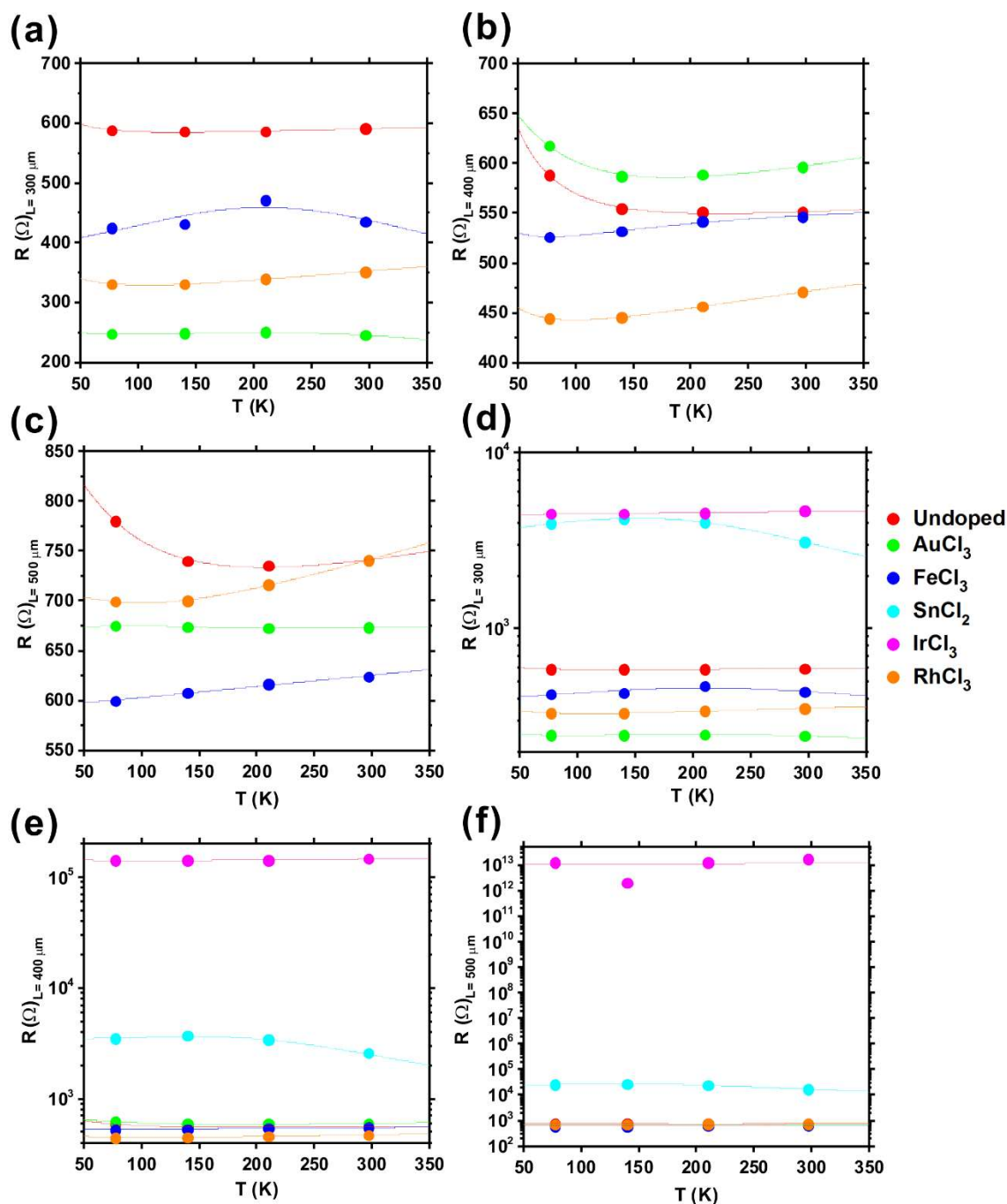
Figure 6.12 Differential resistance calculated from the IV measured with various channel lengths in linear scale: (a) 300 μm, (b) 400 μm and (c) 500 μm, and log scale: (d) 300 μm, (e) 400 μm and (f) 500 μm.

The R vs. T curves of undoped and doped graphenes were successfully fitted with the suggested model over the whole temperature range (77 - 297 K), as illustrated (solid lines) in **Figure 6.12**. For T > 140 K, the doped graphene samples are well matched ($R^2 = 0.97$

134

(AuCl$_3$) - 0.99(RhCl$_3$)), as shown in **Figure 6.12** (a), (b), and (c). The proposed model corresponds well with the resistance variation of doped graphene with higher α (1.1x10$^-$^{3}(AuCl3) – 9.44x10^{-3}(RhCl$_3$)) than the undoped (7.1x10^{-4}) indicating that doped graphene has a large number of charge carriers experiencing scattering and can be regarded as following diffusive transport in an otherwise principally metallic system. Diffusive transport is known to be readily affected by local scattering.[76-77] The scattering of carriers by substrate and interface phonons might contribute to an R increase at high temperatures. The external phonon contribution is strongly dependent on charge carrier density[78] so that the electronic transport in chemically doped graphene at high temperatures appears to be diffusive. To determine which transport is dominant in each doping case, the following discriminant was employed;[74]

$$\varepsilon_{max} = k(T_v T_c^{\,2})^{\frac{1}{3}} \leq \frac{5}{6} E_n \tag{6.11}$$

$$\varepsilon_{max} = k(T_v T_c^{\,2})^{\frac{1}{3}} > \frac{5}{6} E_n \tag{6.12}$$

$$\varepsilon_{max} = k(T_v T_c^{\,2})^{\frac{1}{3}} >> \frac{5}{6} E_n \tag{6.13}$$

where ε$_{max}$ is the maximum energy of VRH, T$_v$ is the VRH hopping parameter, and E$_n$ is the NNH activation energy. In Mott VRH, ε$_{max}$ is the energy between two localised states as defined by $\varepsilon_{max} = k(T_v T_c^{\,2})^{\frac{1}{3}}$ which is dependent on T and should have a value less than the impurity band width (Δε). For NNH conduction, activation is not overly affected by T and the average hopping distance is the mean separation between impurities, grain boundaries, or defects. The activation energy of NNH, E$_n$ ~ 5/6Δε. Thus, if the determinant, Δε = 6/5E$_n$ > ε$_{max}$ is satisfied, purely VRH is valid [74] and NNH or diffusive transport are prohibited. In the opposing case (equation (6.12)), NNH is dominant. If ε$_{max}$ >> 5/6 E$_n$ (equation (6.13)), diffusive transport is dominant. The undoped graphene exhibits VRH to NNH transport, whilst NNH to diffusive transport is dominant in all the doped cases. **Table 2** summarises the dominant electron transport of undoped and doped graphene.

Table 2 Dominant electron transport anticipated by the determinant formula

	Undoped	AuCl$_3$	FeCl$_3$	SnCl$_2$	IrCl$_3$	RhCl$_3$
L=300 µm	VRH~NNH	Diffusive	Diffusive	VRH	VRH	Diffusive
L=400 µm	VRH~NNH	NNH~Diffusive	NNH~Diffusive	VRH	VRH	Diffusive
L=500 µm	VRH~NNH	Diffusive	Diffusive	VRH	VRH	Diffusive
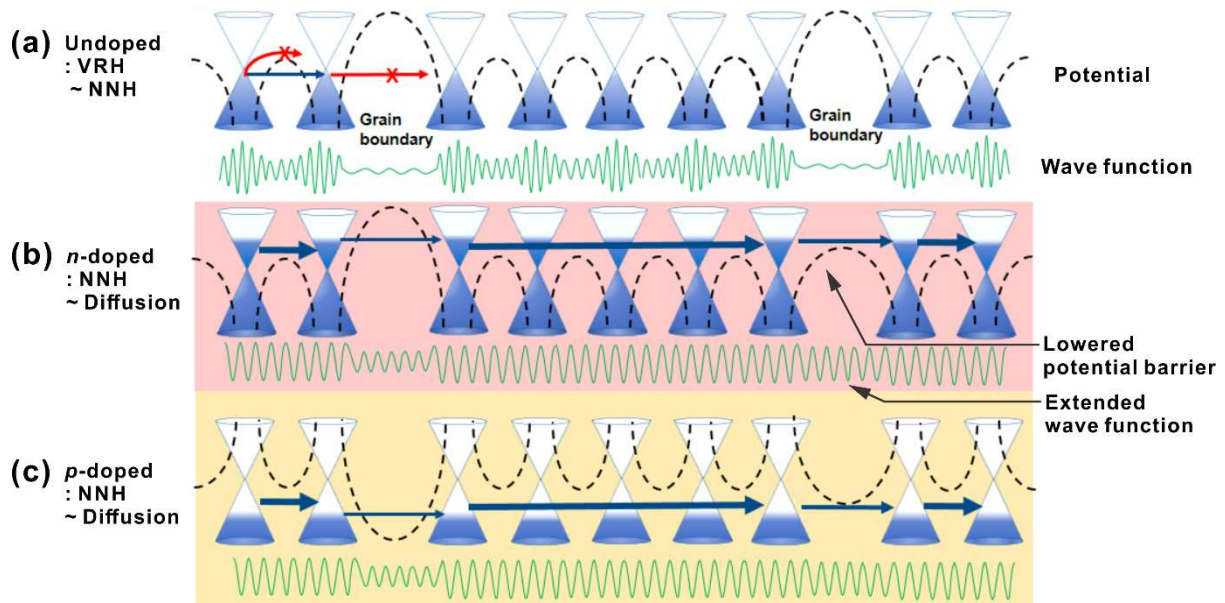
Figure 6.13 Diagrams illustrating the electronic transport of (a) undoped, (b) *n*-doped, (c) *p*-doped graphene through potential barriers such as grain boundaries.

As described in **Figure 6.13**, there are various potential barriers within the transport system. Barriers between carbon atoms are low and easily overcome. Grain boundary or defect states in the carbon lattice are higher and wider than the barriers between carbon atoms such that hopping becomes increasingly difficult. If E_F is at the Dirac point in pristine graphene, the electron wave function becomes localised. The electrons cannot overcome the barrier height at the grain boundaries and defects, even though they may have a finite probability of tunnelling between the C-C barriers. Conversely, *n*-doping moves the E_F higher than potential barrier between adjacent carbon atoms so that the wave function is extended and electrons may move freely. Although electrons can be localised between grain boundaries or defects

even in *n*-doped graphene, tunnelling can happen through the potential barriers of grain boundaries or defects with some probability due to higher E_F (NNH). The potential barriers for holes are in the opposite direction and the same transport mechanism can be applied in *p*-doped graphene as illustrated in **Figure 6.13** (c).

In a polycrystalline material, the grain boundary barrier height (ϕ_b) is inversely proportional to the doping level (N), as given by [79]

$$\phi_b = \frac{q^2 N_t^{\,2}}{8 \varepsilon N}$$

(6.14)

where ϕ_b is the grain boundary barrier height, N_t is the trap density, ε is the grain boundary electric permittivity, q is the elementary electron charge (1.60×10^{-19} C) and N is the increased density of states upon doping. ϕ_b can be lowered by increasing N so that the charge carrier wave function can extend allowing more carriers to overcome the lowered barrier at some grain boundaries, as described in **Figure 6.13** (b) and (c). Thus, charge carriers in doped graphene can move as if there are few to no potential barriers with extended wave functions rather than localised. This leads to a low electrical resistance compared to the barrier-dependent hopping in undoped graphene, but at high temperatures (>140 K), the abundant free carriers experience increased scattering resulting in increased macroscale resistance. Upon doping, the possibility of carrier scattering is increased because of the increased number of carriers. Therefore, VRH is dominant in undoped graphene, whilst transport in doped graphene lies on the border of NNH and diffusive transport. Practically measuring the temperature-dependent R of undoped graphene, it was found that such system experience a combination of VRH and NNH transport.

6.4.3 Contact Resistance of Graphene and Metal Thin Film

Using the various channel lengths available in the circular transmission line model (CTLM), the contact resistance (R_C) was calculated. As shown in **Figure 6.14**, the calculated R_C is < 0.08 Ωcm^2 for undoped and all doped graphene samples, except $SnCl_2$ (0.069 Ωcm^2 at 297 K - 0.177 Ωcm^2 at 77 K) and $IrCl_3$ (20.7 Ωcm^2 at 297 K - 210.5 Ωcm^2 at 77 K). SnO_2

agglomerates (radius: ~ 2μm) may have an effect on the high R_C between Cr/Au electrodes and doped graphene. The R_C can be affected if large amounts of such insulating agglomerates lie at the electrode interface (contact radius: 100 μm). Conversely, the sheet resistance of $SnCl_2$-doped graphene measured by four-point probe (**Figure 6.5** (b)) was lower than that of the undoped graphene.
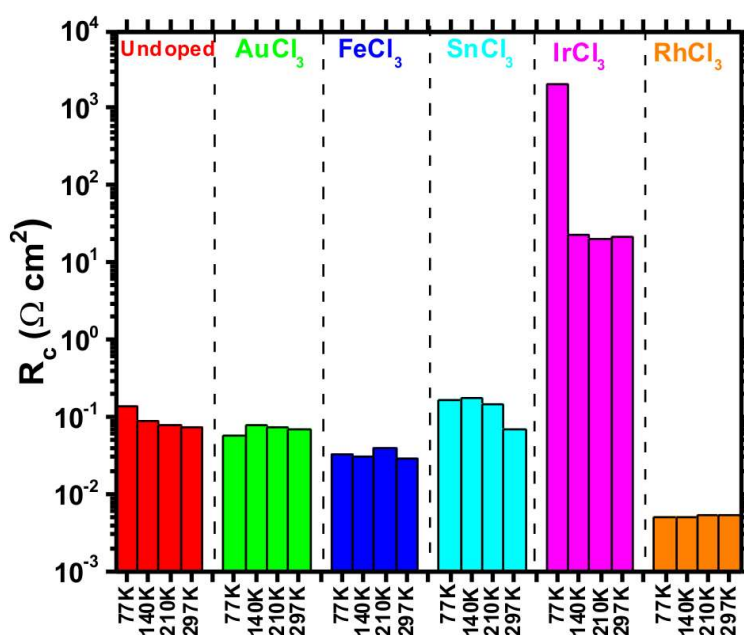
Figure 6.14 Contact resistance (R_C) between graphene and Cr/Au contact electrodes.

$IrCl_3$-doped graphene showed considerably higher resistance in our temperature dependent transport studies, and our contact resistance measurements. These independently measured values differ greatly from published works[80]. The $IrCl_3$ doping anomaly may be associated with the topological insulating behaviour of Ir on graphene.[81-82] Indeed, DFT simulations have shown that Ir atoms adsorbed on graphene can open a small bandgap (0.3 eV).[83] The bandgap opening indicates that graphene with Ir atoms may well have very localised semiconducting characteristics and Schottky barriers at the interface between the metal and graphene thereby increasing R_C.

138

6.5 Summary

Efficient charge transfer mediated by chemical doping with $AuCl_3$, $FeCl_3$, $SnCl_2$, $IrCl_3$ and $RhCl_3$ allows for accurate concurrent control over the resistance (3.5 kΩ to 0.93 Ω) and work function (-0.13 eV($SnCl_2$) to 0.31 eV($AuCl_3$)) of PET-supported CVD graphene. Analyses by XPS, UPS, KPFM, DFT modelling and Hall measurement validated the work function shift findings. Charge carrier transport in graphene was studied at various temperatures with Mott 2D VRH and NNH dominant in undoped graphene whilst NNH and diffusive transport play a major role in the doped graphenes. The successful control of the work function by chemical doping demonstrated in this study suggests graphene is an ideal material for applications where work function optimisation is needed, such as in electron field emission applications, carrier injection layers in OLED and solar cells, as well as highlighting one possible means of advanced contact interface engineering.

Reference

1.   Abdou, M. S. A.; Holdcroft, S., Gold-Decorated Poly(3-Alkylthiophenes). *Chemistry of Materials*, **1996,** *8* (1), 26-31.

2.   Li, S.; Wang, Y.; Lai, C.; Qiu, J.; Ling, M.; Martens, W.; Zhao, H.; Zhang, S., Directional Synthesis of Tin Oxide@Graphene Nanocomposites Via a One-Step up-Scalable Wet-Mechanochemical Route for Lithium Ion Batteries. *Journal of Materials Chemistry A*, **2014,** *2* (26), 10211-10217.

3.   Qi, W. H.; Wang, M. P.; Xu, G. Y., The Particle Size Dependence of Cohesive Energy of Metallic Nanoparticles. *Chemical Physics Letters*, **2003,** *372* (5–6), 632-634.

4.   Seitz, F., *The Modern Theory of Solids*. McGraw-Hill: 1940.

5.   Qi, W. H.; Wang, M. P., Size Effect on the Cohesive Energy of Nanoparticle. *Journal of Materials Science Letters*, **2002,** *21* (22), 1743-1745.

6.   Qi, W.; Wang, M.; Xu, G., The Particle Size Dependence of Cohesive Energy of Metallic Nanoparticles. *Chemical Physics Letters*, **2003,** *372* (5), 632-634.

7.   Linder, D.; Linder, D., Knowledgedoor, Element Handbook. http://www.knowledgedoor.com/2/elements_handbook/cohesive_energy.html.

8.   Eyben, P.; Alvarez, D.; Clarysse, T.; Denis, S.; Vandervorst, W. In *Recent Progress and Insights in Two-Dimensional Carrier Profiling Using Scanning Spreading Resistance Microscopy*, American Institute of Physics: 2003; pp 685-692.

9.   Ou, X.; Das Kanungo, P.; Koegler, R.; Werner, P.; Goesele, U., Carrier Profiling of Individual Si Nanowires by Scanning Spreading Resistance Microscopy. *Nano Letters*, **2010,** *10* (1), 171-175.

10.   Chang, H.; Saito, M.; Nagai, T.; Liang, Y.; Kawazoe, Y.; Wang, Z.; Wu, H.; Kimoto, K.; Ikuhara, Y., Single Adatom Dynamics at Monatomic Steps of Free-Standing Few-Layer Reduced Graphene. *Sci Rep*, **2014,** *4*, 6037.

11.   Lee, D. H.; Lee, J. A.; Lee, W. J.; Choi, D. S.; Lee, W. J.; Kim, S. O., Facile Fabrication and Field Emission of Metal-Particle-Decorated Vertical N-Doped Carbon Nanotube/Graphene Hybrid Films. *The Journal of Physical Chemistry C*, **2010,** *114* (49), 21184-21189.

12.   Palnitkar, U.; Kashid, R. V.; More, M. A.; Joag, D. S.; Panchakarla, L.; Rao, C., Remarkably Low Turn-on Field Emission in Undoped, Nitrogen-Doped, and Boron-Doped Graphene. *Applied Physics Letters*, **2010,** *97* (6), 063102.

13. Lee, D. H.; Lee, J. A.; Lee, W. J.; Kim, S. O., Flexible Field Emission of Nitrogen-Doped Carbon Nanotubes/Reduced Graphene Hybrid Films. *small*, **2011,** *7* (1), 95-100.

14. Shi, S.; Sadhu, V.; Moubah, R.; Schmerber, G.; Bao, Q.; Silva, S. R. P., Solution-Processable Graphene Oxide as an Efficient Hole Injection Layer for High Luminance Organic Light-Emitting Diodes. *Journal of Materials Chemistry C*, **2013,** *1* (9), 1708-1712.

15. Zhong, Z.; Dai, Y.; Ma, D.; Wang, Z. Y., Facile Synthesis of Organo-Soluble Surface-Grafted All-Single-Layer Graphene Oxide as Hole-Injecting Buffer Material in Organic Light-Emitting Diodes. *Journal of Materials Chemistry*, **2011,** *21* (16), 6040-6045.

16. Stratakis, E.; Savva, K.; Konios, D.; Petridis, C.; Kymakis, E., Improving the Efficiency of Organic Photovoltaics by Tuning the Work Function of Graphene Oxide Hole Transporting Layers. *Nanoscale*, **2014,** *6* (12), 6925-6931.

17. Jo, G.; Na, S.-I.; Oh, S.-H.; Lee, S.; Kim, T.-S.; Wang, G.; Choe, M.; Park, W.; Yoon, J.; Kim, D.-Y., Tuning of a Graphene-Electrode Work Function to Enhance the Efficiency of Organic Bulk Heterojunction Photovoltaic Cells with an Inverted Structure. *Applied Physics Letters*, **2010,** *97* (21), 213301.

18. Li, S.-S.; Tu, K.-H.; Lin, C.-C.; Chen, C.-W.; Chhowalla, M., Solution-Processable Graphene Oxide as an Efficient Hole Transport Layer in Polymer Solar Cells. *ACS Nano*, **2010,** *4* (6), 3169-3174.

19. Choudhury, D.; Das, B.; Sarma, D. D.; Rao, C. N. R., Xps Evidence for Molecular Charge-Transfer Doping of Graphene. *Chemical Physics Letters*, **2010,** *497* (1–3), 66-69.

20. Meyer, J.; Kidambi, P. R.; Bayer, B. C.; Weijtens, C.; Kuhn, A.; Centeno, A.; Pesquera, A.; Zurutuza, A.; Robertson, J.; Hofmann, S., Metal Oxide Induced Charge Transfer Doping and Band Alignment of Graphene Electrodes for Efficient Organic Light Emitting Diodes. *Scientific Reports*, **2014,** *4*, 5380.

21. Kramers, H. A.; Heisenberg, W., Über Die Streuung Von Strahlung Durch Atome. *Zeitschrift für Physik*, **1925,** *31* (1), 681-708.

22. Lee, S. Y., Placzek-Type Polarizability Tensors for Raman and Resonance Raman Scattering. *The Journal of Chemical Physics*, **1983,** *78* (2), 723-734.

23. Ferrari, A. C., Raman Spectroscopy of Graphene and Graphite: Disorder, Electron–Phonon Coupling, Doping and Nonadiabatic Effects. *Solid State Communications*, **2007,** *143* (1), 47-57.

24. Malard, L.; Pimenta, M.; Dresselhaus, G.; Dresselhaus, M., Raman Spectroscopy in Graphene. *Physics Reports*, **2009,** *473* (5), 51-87.

25. Heller, E. J.; Yang, Y.; Kocia, L.; Chen, W.; Fang, S.; Borunda, M.; Kaxiras, E., Theory of Graphene Raman Scattering. *ACS Nano*, **2016,** *10* (2), 2803-2818.

26. Ferrari, A. C.; Meyer, J. C.; Scardaci, V.; Casiraghi, C.; Lazzeri, M.; Mauri, F.; Piscanec, S.; Jiang, D.; Novoselov, K. S.; Roth, S.; Geim, A. K., Raman Spectrum of Graphene and Graphene Layers. *Physical Review Letters*, **2006,** *97* (18), 187401.

27.   Li, X.; Cai, W.; An, J.; Kim, S.; Nah, J., Large-Area Synthesis of High-Quality and Uniform Graphene Films on Copper Foils. *Science (New York, N.Y.)*, **2009,** *324* (5932), 1312-1314.

28.   Gao, L.; Ren, W.; Zhao, J.; Ma, L.-P.; Chen, Z., Efficient Growth of High-Quality Graphene Films on Cu Foils by Ambient Pressure Chemical Vapor Deposition. *Applied Physics Letters*, **2010,** *97* (18), 183109.

29.   Kwon, K. C.; Kim, B. J.; Lee, J.-L.; Kim, S. Y., Effect of Anions in Au Complexes on Doping and Degradation of Graphene. *Journal of Materials Chemistry C*, **2013,** *1* (13), 2463-2469.

30.   Kwon, K. C.; Kim, B. J.; Lee, J.-L.; Kim, S. Y., Role of Ionic Chlorine in the Thermal Degradation of Metal Chloride-Doped Graphene Sheets. *Journal of Materials Chemistry C*, **2013,** *1* (2), 253.

31.   Zafar, Z.; Ni, Z. H.; Wu, X.; Shi, Z. X.; Nan, H. Y., Evolution of Raman Spectra in Nitrogen Doped Graphene. *Carbon (New York)*, **2013,** *61*, 57-62.

32.   Iqbal, M. W.; Arun Kumar, S.; Iqbal, M. Z.; Jonghwa, E., Raman Fingerprint of Doping Due to Metal Adsorbates on Graphene. *Journal of Physics: Condensed Matter*, **2012,** *24* (33), 335301.

33.   Kim, K.; Reina, A.; Shi, Y.; Park, H.; Li, L.-J., Enhancing the Conductivity of Transparent Graphene Films Via Doping. *Nanotechnology*, **2010,** *21* (28), 285205.

34.   Wehling, T. O.; Novoselov, K. S.; Morozov, S. V.; Vdovin, E. E.; Katsnelson, M. I.; Geim, A. K.; Lichtenstein, A. I., Molecular Doping of Graphene. *Nano Letters*, **2008,** *8* (1), 173-177.

35.   Murat, A.; Rungger, I.; Jin, C.; Sanvito, S.; Schwingenschlögl, U., Origin of the P-Type Character of Aucl3functionalized Carbon Nanotubes. *The Journal of Physical Chemistry C*, **2014,** *118* (6), 3319-3323.

36.   Charles, K., *Introduction to Solid State Physics*. Wiley: 2004.

37.   Schlaf, R.; Merritt, C. D.; Picciolo, L. C.; Kafafi, Z. H., Determination of the Orbital Lineup at Reactive Organic Semiconductor Interfaces Using Photoemission Spectroscopy. *Journal of Applied Physics*, **2001,** *90* (4), 1903-1910.

38.   Bagus, P. S.; Ilton, E. S.; Nelin, C. J., The Interpretation of Xps Spectra: Insights into Materials Properties. *Surface Science Reports*, **2013,** *68* (2), 273-304.

39.   Tsetseris, L.; Wang, B.; Pantelides, S. T., Substitutional Doping of Graphene: The Role of Carbon Divacancies. *Physical Review B*, **2014,** *89* (3), 035411.

40.   Arsié, L.; Esconjauregui, S.; Weatherup, R.; Guo, Y.; Bhardwaj, S.; Centeno, A.; Zurutuza, A.; Cepek, C.; Robertson, J., Stability of Graphene Doping with Moo3 and I2. *Applied Physics Letters*, **2014,** *105* (10), 103103.

41.   Berger, C.; Song, Z.; Li, X.; Wu, X.; Brown, N.; Naud, C.; Mayou, D.; Li, T.; Hass, J.; Marchenkov, A. N.; Conrad, E. H.; First, P. N.; de Heer, W. A., Electronic Confinement and Coherence in Patterned Epitaxial Graphene. *Science*, **2006,** *312* (5777), 1191-1196.

42.   Akturk, A.; Goldsman, N., Electron Transport and Full-Band Electron-Phonon Interactions in Graphene. *Journal of Applied Physics*, **2008,** *103* (5), 053702.

43.   Chen, J.-H.; Jang, C.; Xiao, S.; Ishigami, M.; Fuhrer, M. S., Intrinsic and Extrinsic Performance Limits of Graphene Devices on Sio2. *Nat Nano*, **2008,** *3* (4), 206-209.

44.   Dorgan, V. E.; Bae, M.-H.; Pop, E., Mobility and Saturation Velocity in Graphene on Sio2. *Applied Physics Letters*, **2010,** *97* (8), 082112.

45.   DasA; PisanaS; ChakrabortyB; PiscanecS; Saha, S. K.; Waghmare, U. V.; Novoselov, K. S.; Krishnamurthy, H. R.; Geim, A. K.; Ferrari, A. C.; Sood, A. K., Monitoring Dopants by Raman Scattering in an Electrochemically Top-Gated Graphene Transistor. *Nat Nano*, **2008,** *3* (4), 210-215.

46.   Ryu, S.; Liu, L.; Berciaud, S.; Yu, Y.-J.; Liu, H.; Kim, P.; Flynn, G. W.; Brus, L. E., Atmospheric Oxygen Binding and Hole Doping in Deformed Graphene on a Sio2 Substrate. *Nano Letters*, **2010,** *10* (12), 4944-4951.

47.   Wehling, T. O.; Lichtenstein, A. I.; Katsnelson, M. I., First-Principles Studies of Water Adsorption on Graphene: The Role of the Substrate. *Applied Physics Letters*, **2008,** *93* (20), 202110.

48.   Lafkioti, M.; Krauss, B.; Lohmann, T.; Zschieschang, U.; Klauk, H., Graphene on a Hydrophobic Substrate: Doping Reduction and Hysteresis Suppression under Ambient Conditions. *Nano Letters*, **2010,** *10* (4), 1149-1153.

49.   Moran-Lopez, J. L.; Bosch, A. T., Changes in Work Function Due to Charge Transfer in Chemisorbed Layers. *Surface Science*, **1977,** *68*, 377-384.

50.   O'Boyle, M.; Hwang, T.; Wickramasinghe, H., Atomic Force Microscopy of Work Functions on the Nanometer Scale. *Applied Physics Letters*, **1999,** *74* (18), 2641-2642.

51.   Rosenwaks, Y.; Shikler, R.; Glatzel, T.; Sadewasser, S., Kelvin Probe Force Microscopy of Semiconductor Surface Defects. *Physical Review B*, **2004,** *70* (8), 085320.

52.   Yu, Y.-J.; Zhao, Y.; Ryu, S.; Brus, L. E.; Kim, K. S.; Kim, P., Tuning the Graphene Work Function by Electric Field Effect. *Nano Letters*, **2009,** *9* (10), 3430-3434.

53.   Wang, X.; Xu, J.-B.; Xie, W.; Du, J., Quantitative Analysis of Graphene Doping by Organic Molecular Charge Transfer. *The Journal of Physical Chemistry C*, **2011,** *115* (15), 7596-7602.

54.   Liscio, A.; Veronese, G. P.; Treossi, E.; Suriano, F.; Rossella, F.; Bellani, V.; Rizzoli, R.; Samorì, P.; Palermo, V., Charge Transport in Graphene–Polythiophene Blends as Studied by Kelvin Probe Force Microscopy and Transistor Characterization. *Journal of Materials Chemistry*, **2011,** *21* (9), 2924-2931.

55.   Filleter, T.; Emtsev, K. V.; Seyller, T.; Bennewitz, R., Local Work Function Measurements of Epitaxial Graphene. *Applied Physics Letters*, **2008,** *93* (13), 133117.

56.   Shi, Y.; Kim, K. K.; Reina, A.; Hofmann, M.; Li, L.-J., Work Function Engineering of Graphene Electrode Via Chemical Doping. *ACS Nano*, **2010,** *4* (5), 2689-2694.

57.   Greiner, W.; Neise, L.; Stöcker, H., *Thermodynamics and Statistical Mechanics*. Springer-Verlag: 1995.

58.   Dean, J. A., *Lange's Handbook of Chemistry*. 15th ed.; McGraw-Hill Book Company, 1979.

59.   Li, X.; Cai, W.; An, J.; Kim, S.; Nah, J.; Yang, D.; Piner, R.; Velamakanni, A.; Jung, I.; Tutuc, E.; Banerjee, S. K.; Colombo, L.; Ruoff, R. S., Large-Area Synthesis of High-Quality and Uniform Graphene Films on Copper Foils. *Science,* **2009,** *324* (5932), 1312-1314.

60.   Neto, A. C.; Guinea, F.; Peres, N. M.; Novoselov, K. S.; Geim, A. K., The Electronic Properties of Graphene. *Reviews of Modern Physics,* **2009,** *81* (1), 109.

61.   Khveshchenko, D., Electron Localization Properties in Graphene. *Physical Review Letters,* **2006,** *97* (3), 036802.

62.   Aleiner, I.; Efetov, K., Effect of Disorder on Transport in Graphene. *Physical Review Letters,* **2006,** *97* (23), 236801.

63.   Han, M. Y.; Brant, J. C.; Kim, P., Electron Transport in Disordered Graphene Nanoribbons. *Physical Review Letters,* **2010,** *104* (5), 056801.

64.   Sarma, S. D.; Adam, S.; Hwang, E.; Rossi, E., Electronic Transport in Two-Dimensional Graphene. *Reviews of Modern Physics,* **2011,** *83* (2), 407.

65.   Kaiser, A. B.; Skakalova, V., Electronic Conduction in Polymers, Carbon Nanotubes and Graphene. *Chemical Society Reviews,* **2011,** *40* (7), 3786-3801.

66.   Joung, D.; Khondaker, S. I., Efros-Shklovskii Variable-Range Hopping in Reduced Graphene Oxide Sheets of Varying Carbon S P 2 Fraction. *Physical Review B,* **2012,** *86* (23), 235423.

67.   Morozov, S. V.; Novoselov, K. S.; Geim, A. K., Electron Transport in Graphene. *Physics-Uspekhi,* **2008,** *51* (7), 744.

68.   Joung, D.; Khondaker, S. I., Efros-Shklovskii Variable-Range Hopping in Reduced Graphene Oxide Sheets of Varying Carbon Sp2 Fraction. *Physical Review B,* **2012,** *86* (23), 235423.

69.   Mott, N. F.; Davis, E. A., *Electronic Processes Innon-Crystalline Materials*. Clarendon Press Oxford: 1971; Vol. 1.

70.   Efros, A. L.; Shklovskii, B. I., Coulomb Gap and Low Temperature Conductivity of Disordered Systems. *Journal of Physics C: Solid State Physics,* **1975,** *8* (4), L49.

71.   Vishwakarma, P.; Subramanyam, S., Hopping Conduction in Boron Doped Amorphous Carbon Films. *Journal of Applied Physics,* **2006,** *100* (11), 113702.

72.   Yu, D.; Wang, C.; Wehrenberg, B. L.; Guyot-Sionnest, P., Variable Range Hopping Conduction in Semiconductor Nanocrystal Solids. *Physical Review Letters,* **2004,** *92* (21), 216802.

73.   Martin, J.; Akerman, N.; Ulbricht, G.; Lohmann, T.; Smet, J. H.; von Klitzing, K.; Yacoby, A., Observation of Electron-Hole Puddles in Graphene Using a Scanning Single-Electron Transistor. *Nat Phys,* **2008,** *4* (2), 144-148.

74.   Park, J.; Mitchel, W. C.; Elhamri, S.; Grazulis, L.; Altfeder, I., Abnormal Hopping Conduction in Semiconducting Polycrystalline Graphene. *Physical Review B,* **2013,** *88* (3), 035419.

75.   Rossiter, P. L., *The Electrical Resistivity of Metals and Alloys*. Cambridge University Press: 1987.

76. Colinge, J. P.; Colinge, C. A., *Physics of Semiconductor Devices*. Springer: 2005.

77. Ehrenreich, H.; Turnbull, D., *Advances in Research and Applications: Semiconductor Heterostructures and Nanostructures*. Elsevier Science: 1991.

78. Das Sarma, S.; Adam, S.; Hwang, E. H.; Rossi, E., Electronic Transport in Two-Dimensional Graphene. *Reviews of Modern Physics***, 2011,** *83* (2), 407-470.

79. Orton, J. W.; Powell, M. J., The Hall Effect in Polycrystalline and Powdered Semiconductors. *Reports on Progress in Physics***, 1980,** *43* (11), 1263.

80. Kwon, K. C.; Kim, B. J.; Lee, J.-L.; Kim, S. Y., Role of Ionic Chlorine in the Thermal Degradation of Metal Chloride-Doped Graphene Sheets. *Journal of Materials Chemistry***, 2013,** *1* (2), 253-259.

81. Hu, J.; Alicea, J.; Wu, R.; Franz, M., Giant Topological Insulator Gap in Graphene with 5d Adatoms. *Physical Review Letters***, 2012,** *109* (26), 266801.

82. Chang, P.-H.; Bahramy, M. S.; Nagaosa, N.; Nikolić, B. K., Giant Thermoelectric Effect in Graphene-Based Topological Insulators with Heavy Adatoms and Nanopores. *Nano Letters***, 2014,** *14* (7), 3779-3784.

83. Lazar, P.; Granatier, J.; Klimes, J.; Hobza, P.; Otyepka, M., The Nature of Bonding and Electronic Properties of Graphene and Benzene with Iridium Adatoms. *Physical Chemistry Chemical Physics***, 2014,** *16* (38), 20818-20827.

Chapter 7   Conclusion and Outlook

7.1   Conclusion

This thesis has presented two novel approaches to the transfer of CVD graphene from the growth metallic catalyst to polymer destination substrates. The developed approached, termed hot press lamination (HPL) and UV-Adhesive (UVA) have shown dramatically improved graphene adhesion whilst the author's work on chemical doping using metal chloride compounds has evidenced an interesting route to enhance electrical the conduction of the transferred graphene.

CVD is widely considered to be the most viable and commercially attractive technique to realise the use of graphene as a transparent flexible conductor in large-area electronics, in applications such as OLEDs. However, the use of CVD graphene necessitates the concurrent development of transfer processes to move the as-synthesised graphene from its opaque metallic catalyst to a wide range of arbitrary substrates. Though established, conventional PMMA-transfer causes varied functional issues for the mass production of large graphene sheets, such as deleterious polymer residues, handling challenges associated with samples larger than a few cm-square, as well as, and perhaps most critically, rather weak interfacial adhesion. On the contrary, the outlined HPL and UVA transfer approaches, detailed in this thesis, not only offer simple, fast, and low-cost processing, but also display strong, long-lasting adhesion between the graphene and the PET substrates (UVA: 4.40±1.09 N/m, HPL: 0.60 ±0.26 N/m) compared to equivalent CVD-graphene transferred by PMMA (0.44±0.06 N/m). By means of bend angle and repeated bending fatigue experiments, it has been shown that graphene on PET is more mechanically stable than ITO on PET, independent of the transfer method employed. After 10^4 bend-relax cycles, graphene showed a much higher

maintained conductivity and robustness towards straining fatigue, without the formation of notable cracks and with little variation in the normalised resistance (PMMA: 0.80, UVA: 0.53, and HPL: 0.65), whilst severe micro-crack nucleation and growth were noted in ITO samples, resulting in large resistance increase (x34.5). The superiority of the developed UVA and HPL approaches, in terms of maintained conductivity, was validated by dramatically smaller resistance changes compared to PMMA-transferred-graphene.

For the use as a transparent flexible electrode in applications requiring sheet resistances that could not be achieved by using the CVD graphene alone, such as in OLEDs, a hybrid structure of AgNW/graphene on PET was considered due to its low R_S (57 ± 14 Ω/sq.). However, voids and sharped, perturbances associated with the AgNWs in test cells resulted in non-uniform light emission and issues with electrode short-circuits. As an alternative to the studied AgNW/graphene hybrid, chemical doping was considered by studying the transport effects of various Me_xCl_y compounds as a means of decreasing R_S without deteriorating the optical transparency. The most dramatic reduction in R_s was observed upon $AuCl_3$ doping, decreasing R_S from 2.6 kΩ/sq. to 0.4 kΩ/sq. with only a 1.5 % decrease in %T. The largest dopant molecular time-dependent desorption occurred for $RhCl_3$-doped graphene ($\Delta\Gamma/\Gamma_0 = -1.06$) resulting in the largest increase in R_S (0.8kΩ/sq.) after 200h in air at STP, suggesting that dopant desorption is the most influential factor in degrading the temporal stability of such doped graphene systems.

Experimental efforts revealed chemical doping as an accurate means of work function tuning in graphene. The increased carrier density upon charge transfer associated with the metallic constituents in the dopant Me_xCl_y compounds contributed to both an R_S decrease and also notable work function shifts ($\Delta\varphi = 0.31$ eV ($AuCl_3$) to -0.13 eV ($SnCl_2$)) of the transferred CVD graphene on PET. High work function shifts were observed in $AuCl_3$ (0.31 eV) and $IrCl_3$ (0.25 eV) with the negatively largest Gibb's free energy ($AuCl_3$: -145.7 kJ/mol, and $IrCl_3$: -179.9 kJ/mol).

Temperature-dependent electron transport, following doping, was explored in terms of the engineered work function and carrier concentration. Existing conduction models, such as thermal activation, VRH and NNH were found wanting in the present doped systems to explain the observed carrier transport given the assumption of semiconducting graphene

oxide or pristine graphene with E_F pined at the Dirac point. This thesis proposes a new, modified temperature-dependent conduction model for doped graphene which shows excellent agreement with the empirical differential resistance variation measured from 77K – 297 K (R^2 = 0.97 (AuCl$_3$) - 0.99 (RhCl$_3$)). The present studies suggested that the charge carrier wave functions in the doped samples shifted the E_F and were extended allowing them to overcome the potential barriers associated with grain boundaries. Conversely, undoped samples had notably localised transport. Barrier dependent hopping transport in pristine graphene was, upon chemical doping, changed to an extended, metallic-like conduction behaviour. The increased number of charge carriers in the doped graphenes where found to experience increased scattering at high, near room temperatures, resulting in an increased resistance. Carrier transport in Me_xCl_y doped graphene has been described, for the first time, with diffusive transport, whilst VRH and NNH were found to dominate in undoped graphene.

7.2 Outlook

The studies in previous chapters focused on achieving mechanical stability and conductivity enhancement of PET-supported CVD graphene. Elucidating the micro-scale physics and chemistry of such systems empirically revealed a variety of otherwise unique physical properties that require further study to fully provide a full understanding.

The further research associated with this thesis can be classified in three principle directions, namely;(1) focussing on the practical use of the proposed approaches in commercial scale mechanically flexible OLED devices, (2) the development of *p-n* and *p-i-n* diodes using pristine and partially *n-* and *p-* dopants, and (3) an extended study on the transport including the exploration of the topological insulating characteristics of CVD-graphene upon doping with IrCl$_3$.

(1) More specifically, these three future themes can be extended, as the decreased R_S and improved adhesion of graphene attained in this study are applicable to the actual fabrication of large area flexible displays. This work would focus on the production of

OLED cells fabricated using both graphene processed with the developed techniques as well as conventional ITO. The luminance efficiency, light intensity, and uniformity would subsequently be analysed and compared to the ITO control OLED.

(2) A graphene *p-n* junction would be fabricated by local chemical doping of graphene sheets, possibly through the use of micro-inkjet printing, or emerging nanofabrication techniques, such as Dip Pen Nanolithography, or through the use of photolithograpahically-defined wells. Such *p-n* junction diodes would be considered for use in photosensor applications. The photocurrent of such graphene diodes would likely be dominated by the junction potential [1] so that the sensor sensitivity can be controlled as a function of dopant concentration, all towards realising one of the thinnest, mechanically flexible photo-sensors yet reported.

(3) As discussed in Chapter 5 and Chapter 6, IrCl$_3$-doped graphene displayed a somewhat anomalous higher resistance (12 kΩ/sq.) than the undoped graphene (3.5 kΩ/sq.). This unexpected, semi-insulating behaviour has been theoretically studied elsewhere.[2-3] Graphene coated with atomic Ir been shown to offer physical properties not dissimilar to topological insulators, with DFT simulations demonstrating the opening of a bandgap (0.3 eV).[4] The experimental findings on IrCl$_3$-doped graphene in this thesis go some way to support these reports and highlight the possibility for the use of such Ir-doped graphene as a unique FET channel which overcomes many issues associated with the near-zero bandgap of graphene. Attempts have been made elsewhere to open a band gap using gate-field induction in bi-layer graphene,[5-7] and oxygen plasma treatment as a means of symmetry breaking of the carbon lattice.[8] Both strategies are non-trivial to exploit. However, imparting a band gap through simple, low cost doping processes based on IrCl$_3$may make for a viable means of realising alternative channels in switching devices to complement silicon-based FETs.

For the upcoming transparent flexible electronics era, such future work would make graphene a truly competitive and readily applicable solution to some of the most pressing, yet equally promising, transparent electronics applications, devices and systems.

References

1.   Peters, E. C.; Lee, E. J.; Burghard, M.; Kern, K., Gate Dependent Photocurrents at a Graphene Pn Junction. *Applied Physics Letters*, **2010,** *97* (19), 193102.

2.   Hu, J.; Alicea, J.; Wu, R.; Franz, M., Giant Topological Insulator Gap in Graphene with 5d Adatoms. *Physical Review Letters*, **2012,** *109* (26), 266801.

3.   Chang, P.-H.; Bahramy, M. S.; Nagaosa, N.; Nikolić, B. K., Giant Thermoelectric Effect in Graphene-Based Topological Insulators with Heavy Adatoms and Nanopores. *Nano Letters*, **2014,** *14* (7), 3779-3784.

4.   Lazar, P.; Granatier, J.; Klimes, J.; Hobza, P.; Otyepka, M., The Nature of Bonding and Electronic Properties of Graphene and Benzene with Iridium Adatoms. *Physical Chemistry Chemical Physics*, **2014,** *16* (38), 20818-20827.

5.   Oostinga, J. B.; Heersche, H. B.; Liu, X.; Morpurgo, A. F.; Vandersypen, L. M., Gate-Induced Insulating State in Bilayer Graphene Devices. *Nat Mater*, **2008,** *7* (2), 151-7.

6.   Zhang, Y.; Tang, T.-T.; Girit, C.; Hao, Z.; Martin, M. C.; Zettl, A.; Crommie, M. F.; Shen, Y. R.; Wang, F., Direct Observation of a Widely Tunable Bandgap in Bilayer Graphene. *Nature*, **2009,** *459* (7248), 820-823.

7.   Mak, K. F.; Lui, C. H.; Shan, J.; Heinz, T. F., Observation of an Electric-Field-Induced Band Gap in Bilayer Graphene by Infrared Spectroscopy. *Physical Review Letters*, **2009,** *102* (25), 256405.

8.   Nourbakhsh, A.; Cantoro, M.; Vosch, T.; Pourtois, G.; Clemente, F.; van der Veen, M. H.; Hofkens, J.; Heyns, M. M.; De Gendt, S.; Sels, B. F., Bandgap Opening in Oxygen Plasma-Treated Graphene. *Nanotechnology*, **2010,** *21* (43), 435203.